UNIVERSITY OF CALIFORNIA,
IRVINE

Designing Fuel Cell Oxygen Reduction Electrocatalysts: from Carbon Supports to Membrane Electrode Assembly Evaluation

DISSERTATION

submitted in partial satisfaction of the requirements
for the degree of

DOCTOR OF PHILOSOPHY

in Chemical and Biochemical Engineering

by

Morteza Rezaei Talarposhti

Dissertation Committee:
Professor Plamen Atanassov, Chair
Associate Professor Iryna Zenyuk
Professor Yun Wang

2020

TABLE OF CONTENTS

LIST OF FIGURES

LIST OF TABLES

VITA

Morteza Rezaei Talarposhti

Work Experience

Jan 2019 – Present, University of California Irvine, **Irvine, CA, USA**
Research Assistant, Department of Chemical and Biochemical Engineering, National Fuel Cell Research Center

Nov 2016 – Dec 2018, The University of New Mexico, **Albuquerque, NM, USA**
Research Assistant, Department of Chemical and Biological Engineering, Center for Micro Engineered Materials, Advanced Material Laboratory

Mar 2014 – May 2016, Pars Lian Chemical Company **Tehran, Iran**
Technical Service Engineer in Petroleum Treatment
Petroleum Process
Bottle testing
Oil Field Control

May 2013 – Mar 2014, Pasaddak Co. **Tehran, Iran**
Research and Development Supervisor
Customer Service
Technical Support
Line Start Up

Jan 2010 – Nov 2015, Iran Language Institute **Tehran, Iran**
English Tutor (part time)
Tutoring English to young-adult Learners

EDUCATION

Nov 2017- Present **University of California, Irvine** **Irvine, CA, USA**
Chemical Engineering, Ph.D. (Degree Expected by 09/20)
Thesis: Elaboration of the Effect of Carbon Support, Particle Proximity and Ionomers on the Mechanism of the Oxygen Reduction Reaction Using Kinetic Isotope Effect Studies and Membrane Electrode Assembly Testing
Advisor: *Dr. Plamen Atanassov*

Sep 2016 – Nov 2017 **The University of New Mexico** **Albuquerque, NM, USA**
Chemical Engineering, Master (MSc)
Thesis: Microbial Desalination Cells with Efficient Platinum-Group-Metal-Free Cathode Catalysts
Advisor: *Dr. Plamen Atanassov*

Sep 2008 – Sep 2011 **Science and Research Branch of Azad University** **Tehran, Iran**
Chemical Engineering, Master (MSc)
Thesis: The Effect of Nitrogen Sources on Optimization of the Culture Media of *Saccharopolyspora erythraea*

Sep 2003 – Sep 2008 **Iran University of Science and Technology** **Tehran, Iran**
Chemical Engineering, Bachelor (BSc)
Thesis: A Survey on the Expansion Properties of High Aluminate Cement with Different Contents of Gypsum

PUBLICATIONS

1- **Morteza Rezaei Talarposhti**, Carlo Santoro, Mounika Kodali, Rohan Gokhale, Alexey Serov, Irene Merino-Jimenez, Ioannis Ieropoulos and Plamen Atanassov; Microbial Desalination Cells with Efficient Platinum-Group-Metal-Free Cathode Catalysts, *ChemElectroChem* 2017,4, 3322–3330

2- Aaron Roy, **Morteza R. Talarposhti**, Stanley J. Normile, Iryna V. Zenyuk, Vincent De Andrade, Kateryna Artyushkova, Alexey Serov and Plamen Atanassov; Nickel–copper supported on a carbon black hydrogen oxidation catalyst integrated into an anion-exchange membrane fuel cell, *Sustainable Energy Fuels*, 2018, 2, 2268

3- Jiangjin Liu, **Morteza Rezaei Talarposhti**, Tristan Asset, Dinesh C. Sabarirajan, Dilworth Y. Parkinson, Plamen Atanassov and Iryna V. Zenyuk; Understanding the Role of Interfaces for Water Management in Platinum Group Metal-Free Electrodes in Polymer Electrolyte Fuel Cells, *ACS Appl. Energy Mater.* 2019, 2, 3542−3553

4- **Morteza Rezaei Talarposhti**, Tristan Asset, Samuel T. Garcia, Yechuan Chen, Sergio Herrera, Sheng Dai, Eric J. Peterson, Kateryna Artyushkova, Iryna V. Zenyuk and Plamen Atanassov; . Part II: Effect of the Platinum Dispersion. *ChemPhysChem* 10.1002/cphc.201901092

5- L. Cheng, K.K. Khedekar, **M. Rezaei Talarposhti**, A. Perego, M. Metzger, S. Kuppan, S. Stewart, P. Atanassov, N, Tamura, N. Craig, I. Zenyuk, C. Johnston, Mapping of Heterogeneous Catalyst Degradation in Polymer Electrolyte Fuel Cells, (2020), *Advanced Energy Materials*, 10.1002/aenm.202000623

6- **M.R. Talarposhti**, T. Asset, A. Roy, K. Artyushkova, L.-K. Tsui, F.H. Garzon, A. Serov, and P. Atanassov, Nickel-Copper Catalysts: Effect of Carbon Supports in Hydrogen Oxidation Activity in Alkaline Electrolyte, *ChemElectroChem*, (2020) ***submitted***

7- **Morteza Rezaei Talarposhti**, Kaustubh Khedekar, Lei Cheng, Saravanan Kuppan, Andrea Perego, Yechuan Chen, Michael Metzger, Sarah Stewart, Plamen Atanassov, Nobumichi Tamura, Nathan Craig, Christina Johnston, Iryna V. Zenyuk, Probing Heterogeneous Degradation of Catalyst in PEM Fuel Cells Under Realistic Automotive Conditions with Multi-modal Techniques, Joule (2020) ***submitted***

CONFERENCES

Oct01 – Oct05, 2017 232nd Electrochemical Society Meeting, **National Harbor, MA, USA**
Title: Nickel–copper supported on a carbon black hydrogen oxidation catalyst integrated into an anion-exchange membrane fuel cell
Authors: Aaron Roy, **Morteza R. Talarposhti**, Stanley J. Normile, Iryna V. Zenyuk, Vincent De Andrade, Kateryna Artyushkova, Alexey Serov and Plamen Atanassov

Oct13 – Oct17, 2019 236th Electrochemical Society Meeting, **Atlanta, GA, USA**
Title: Kinetic Isotope Effect as a Tool to Investigate the Oxygen Reduction Reaction on Pt based Electrocatalysts
Authors: **Morteza Rezaei Talarposhti**, Tristan Asset, Samuel T. Garcia, Yechuan Chen, Sergio Herrera, Sheng Dai, Eric J. Peterson, Kateryna Artyushkova, Iryna V. Zenyuk and Plamen Atanassov

ABSTRACT

Designing Fuel Cell Oxygen Reduction Electrocatalysts: from Carbon Supports to Membrane Electrode Assembly Evaluation

by

Morteza Rezaei Talarposhti

Doctor of Philosophy in Chemical and Biochemical Engineering

University of California, Irvine, 2020

Professor Plamen Atanassov, Chair

This work investigates the oxygen reduction reaction (ORR) mechanism on Pt nanoparticles (NPs) dispersed on several carbon blacks with various physicochemical properties (*i.e.* specific surface area ranging from 80 to 900 $m^2 g^{-1}$, different graphitization degree, *etc*.). Using the kinetic isotope effect (KIE) along with various electrochemical characterizations, it was determined that the rate determining step (RDS) of the ORR is a proton-independent step when the density of Pt NPs on the surface of the carbon support is high. Upon decrease of the density of Pt NPs on the surface, the RDS of the ORR starts involving a proton, as denoted by an increase of the KIE > 1. This underlined the critical role played by the carbon support in the oxygen reduction reaction electrocatalysis by Pt supported on high surface area carbon. Furthermore, two of these carbon supports were selected and using the same synthesis methods, different loadings of Pt NPs were deposited on them. This allowed us to investigate the effect of catalyst loading, thus, take another approach to assess the particle proximity effect on the ORR.

The durability and performance of the selected electrocatalysts were also explored in a membrane electrode assembly (MEA) in real-world operational conditions of automotive fuel cells. The effect

of the loading of the platinum nanoparticles (Pt NPs) supported on two of the carbon supports with different morphologies (93 vs. 890 m^2 g^{-1}) on the oxygen reduction reaction (ORR) was also investigated. The correlation between their electrochemical performances with their physico-chemical properties was suggested. The experiments were extended from bench-scale lab tests to pilot-size membrane electrode assembly (MEA) fuel cell testing where the performance and durability of the in-house synthesized electrocatalyst was investigated. On the result basis, it was confirmed that low platinum loading on a high surface area carbon support resulted in a contribution of the latter to the ORR (see Chapter II for additional details). Moreover, it was observed that in the MEA systems, when using electrocatalyst with a large loading of Pt on the electrode – and thus a thin catalytic layer on the cathode side – at high current densities, flooding would partially block the Pt active site and thus limits the fuel cell performances. Finally, the heterogeneity of polymer electrolyte fuel cells (PEFCs) catalyst degradation was studied under varied relative humidity and type of feed gas. Accelerated stress tests (AST) were performed on four membrane electrode assemblies (MEAs) under wet and dry conditions in air or nitrogen environment for 30,000 square cycles from 0.60 V to 0.95 V (or open circuit voltage (OCV) for air since during cycling in air the OCV drops to values below 0.9 V). It was observed that the largest electrochemical active area (ECSA) loss during the ASTs was for MEA in wet conditions under nitrogen gas. This was mainly attributed to higher upper potential limit (UPL) of 0.95 V that was maintained during experiment and to higher water content in the MEA enabling higher Pt^{2+} mobility. In air the OCV was lower than 0.95 V during cycling reducing the overall upper potential limit (UPL) to below 0.95 V and thus reducing the rate of platinum oxide (PtO) formation and dissolution. Micro XRD was performed on end of life (EOL) MEAs to show Pt particle size distribution under lands and channels and in various MEA locations. Largest Pt sizes were

observed for wet conditions and under the lands. Both represent locations in MEAs with higher water content. AST in air and wet environment showed the highest Pt particle size growth from inlet to outlet, which is due to larger water content at the outlet compared to the inlet. Micro XRF shows that Pt redistribution is a local phenomenon and Pt loading remains relatively uniform within the MEA. Additional diagnostics were used to understand morphology of the MEA at the EOL and confirmed that catalyst layer support structure does not change during AST. Conclusively, the ORR mechanism is subject to different environmental factors, including the morphological and surface characterization of the carbon support, density of the Pt NPs deposited on the support and operation conditions. A wide range of characterization methods and investigations protocols and procedures, ranging from bench-size lab scale tests to pilot-size automotive operation condition fuel cells was implemented. We hypothesized the ORR mechanism, investigated the effect of surface density and particle proximity of Pt NPs and showed the heterogeneity in the MEAs degradation p

Chapter 1

Introduction

1.1 Proton Exchange Membrane Fuel Cells

Fossil fuel depletion and our ever-increasing need to energy make the development of sustainable source of small and large-scale energy, critically essential, such as wind turbines, solar and photovoltaic cells and fuel cells.[1–3] Among them, fuel cells show the most promising balance between power production and anthropogenic impact on nature.[4] There are different types of fuel cells, *i.e.* proton exchange membrane fuel cells (PEMFC),[5] alkaline fuel cells,[6,7] Direct methanol,[8] solid oxide,[9] phosphoric acid[10] and molten carbonate fuel cells.[11] PEMFCs deliver higher power densities at a lower weight and volume compared to other fuel cells. PEMFCs are able to operate at moderate temperatures (*i.e.* ca. 80 °C), thus allowing short startup times. These advantages make them attractive power sources for mobile applications (*e.g.* cars, buses, etc.).[12–18]

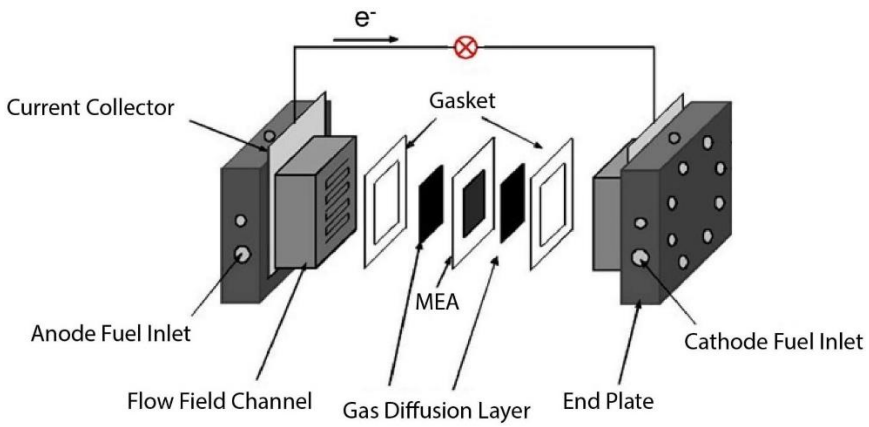

Figure 1.1. Schematic of a single cell polymer electrolyte membrane fuel cell[19]

PEMFCs consist of a solid polymer, proton conducting membrane, separating two gas diffusion electrodes, which can be divided in two parts, *i.e.* (i) the gas diffusion layer and the microporous

layer, which provide gases and electrons to the second part, (ii) the catalytic layer (CL). The latter is often made of an active material, under the form of nanoparticles, supported on a porous carbon and partly covered in ionomer. On the cathode side of the fuel cell, oxygen reduces to water (ORR) and on the anode side hydrogen oxidizes to protons (HOR). Platinum is considered to be the best single metal electrocatalyst on both cathode[20] and anode[21] sides of a fuel cell due to high activity and durability in acidic conditions.[22] (see **Figure 1.1** for a single fuel cell assembly) Pt-Based electrocatalysts can be divided in three classes that are *(i)* pure Pt, *(ii)* Pt alloys and *(iii)* core-shell structures. In this thesis we only concentrate on pure platinum as we are studying the fundamentals of the oxygen reduction reaction and the phenomena that take place at the electrocatalyst surface. Pt is a scarce and expensive element, hence requiring its maximal loading to be limited in a fuel cell electrode.[23] The composition and structure of the support, as well as the operating conditions play a key role in carbon supported Pt NPs degradation. Some of the properties of the Pt NPs and supports influencing the degradation processes are listed as: *(i)* Pt loading and particle size, *(ii)* effective particle coverage on the support surface, *(iii)* Temperature and pH of the system, *(iv)* contamination and impurities and *etc*.[24]

Pt nanoparticles degradation and loss of active surface area of the electrocatalysts (ECSA loss) in the fuel cell system is dominated by three mechanisms that cause loss of Pt NPs that are *(i)* physical detachment of Pt, induced by the carbon corrosion, dissolution of Pt that can be followed by *(ii)* redeposition on larger Pt NPs causing Ostwald ripening or *(iii)* by reduction of Pt^{2+} ions on the membrane due to reduction with crossover H_2.[25] In cathodic and anodic sweeps at high potentials, Pt dissolution is the dominant degradation mechanism [26,27] and is controlled by Pt NPs particle size and oxide coverage.[28] (See **Figure 1.2** for detailed schematic of Pt degradation)

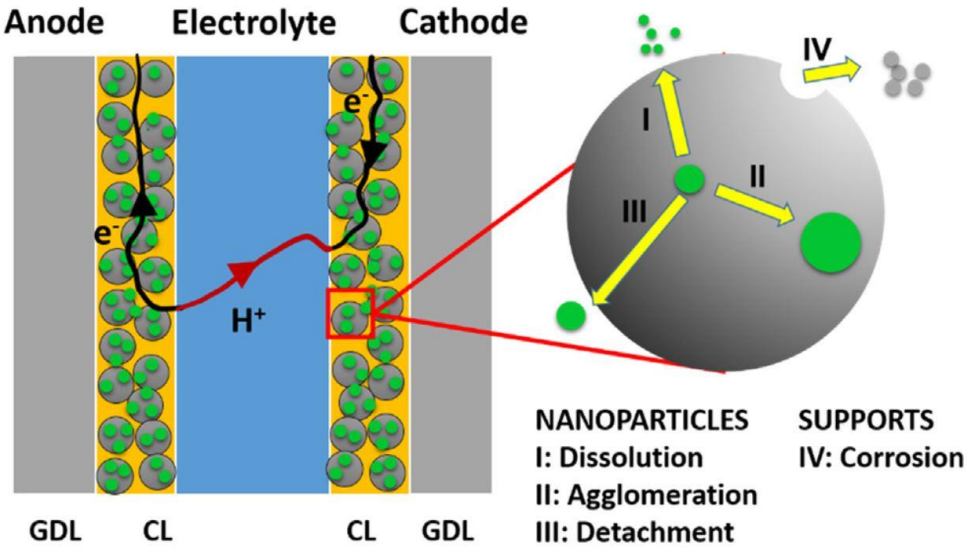

Figure 1.2 Schematic representation of platinum corrosion, including (i) Dissolution, (ii) Agglomeration (iii) Detachment and (iv) carbon support corrosion. (v) Ostwald ripening is a common phenomenon that is consisted of dissolution of Pt NPs and re-deposition on other Pt NPs, *(vi)*Pt deposition on the polymer electrolyte membrane is another corrosion that occurs for Pt NPs deposited on carbon supports. (*image reprinted from Ref.*[29])

According to the Gibbs-Thomson equation, smaller nanoparticles exhibit a higher surface energy and are thus more likely to dissolve – and eventually re-deposit on larger nanoparticles through Ostwald ripening. Alternatively, dissolved Pt ions can migrate and precipitate in the membrane through their reaction with the H_2 crossing over. Accelerated stress testing is generally a method to test electrocatalysts for their durability in fuel cell systems and consists of potential cycling between two operative potentials to simulate the load change (in automotive operation conditions *i.e.* potentials ranging from 0.2 to 1 V, in startup/shutdown conditions *i.e.* where the potential momentarily shoots up to 1.5 V, *etc.*) to accelerate the degradation of catalyst layer for research purposes on fuel cells.[30–32]

As stated in the previous paragraph, carbon suffers from corrosion under fuel cell conditions like start-up/shutdown and fuel starvation with the following reaction:[33]

$$C + 2H_2O \rightarrow CO + 4H^+ + 4e^- \; E^0 = 0.207 \; vs. NHE \; at \; 25 \; ^\circ C \qquad (1.1)$$

Carbon support corrosion causes detachment, agglomeration and sintering of Pt NPs, leading to notable losses in ECSA. Carbons with higher graphitic content lead to a better resistance against corrosion.[34] The supports (and their impact on the Pt reactivity and electrocatalyst overall stability) can be tuned by doping the support.[35–41]

1.2 Oxygen Reduction Reaction

The ORR, the limiting reaction of the PEMFCs, has been widely studied in the literature.[42] It can take place through two different pathways:[43,44] the 4-electron transfer pathway or a series of 2-electron transfer reactions, both of which are shown below:

4-electron Pathway:

$$O_2 + 4H^+ + 4e^- \leftrightarrow 2H_2O \qquad (1.2)$$

2-electron Pathway:

$$O_2 + 2H^+ + 2e^- \leftrightarrow 2H_2O_2 \qquad (1.3)$$

Peroxide can undergo further reduction or decomposition in acidic solutions[45] with the following reactions:

$$H_2O_2 + 2H^+ + 2e^- \leftrightarrow H_2O \qquad (1.4)$$

$$H_2O_2 \leftrightarrow H_2O + {}^1/_2\, O_2 \qquad (1.5)$$

On platinum, the rate-determining step (RDS) of the ORR, is often admitted as the first protonation of the oxygen,[46] *i.e.*

$$O_2 + H^+ + e^- \leftrightarrow OOH_{ads} \quad (1.6)$$

1.3 Active Material

Using platinum as active material increases the final cost of the fuel cell due to its scarcity and thus confines the feasibility and commercialization of PEMFCs.[37,47,48] Widespread vehicle market acceptance has not yet been obtained for PEMFCs despite of decades of research.[49] Thus, it becomes essential to maximize the performance of the fuel cell per unit mass of platinum by increasing the exposure of its active sites for the ORR and achieve the department of energy goals.[50,51] Based on the expected advancements, the projected cost of the energy, for PEMFCs in vehicles applications, by 2020 and 2025, are *ca.* \$47/kW_{net} and *ca.* \$40/kW_{net} respectively.[52]

The ECSA is an important factor in determining the performance of a fuel cell.[53–55] It is a good indicator of the quality of the electrocatalyst along with mass activity (MA).[56] Gasteiger *et. al.*[57] have concluded that ECSA and MA are independent of catalyst loading. The surface area per unit volume has been regarded independent of the loading with the assumption of spherical shape for the nanoparticles. Researchers have introduced a non-linear scaling factor for the volumetric agglomerate density. Researchers found that high loadings of Pt NPs results in smaller ECSAs.[58] Pozio *et al.*[59] reported that at high Pt loadings, some of the Pt NPs were sunk in the carbon substrate, hence being blocked and not accessible to the ionic species (e.g. H^+) needed for the reaction. Before going into details of the different methods currently investigated to achieve such goals, we will introduce two fundamental notions to assess the efficient use of Pt in PEMFCs, *i.e.* the electrochemical surface area (ECSA) and the Pt utilization. To calculate the ECSA, two major methods are used in the literature,[60] *i.e.* H-Adsorption and CO-Stripping.

The H-Adsorption method is based on the charge needed to remove a monolayer of adsorbed hydrogen.[61] (see **Figure 1.3**)

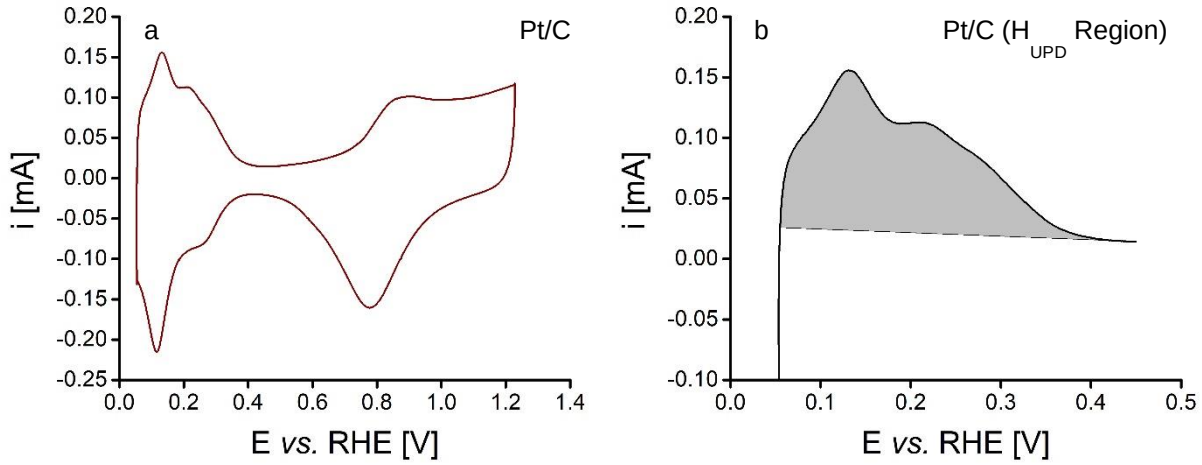

Figure 1.3 Pt/C cyclic voltammetry in N_2-Saturated electrolyte (a) and a zoom on the H_{upd} region of the voltammogram where we integrate to finally calculate ECSA. (b)

ECSA determination usually requires some assumptions. For instance, hydrogen adsorption/desorption charge density on Pt is 210 μC/cm$^2_{pt}$, assuming the adsorption of one hydrogen atom per platinum atom. However, the hydrogen monolayer does not provide a 100% coverage on Pt active sites, thus, anions can also adsorb and block the active site which is responsible for to an additional +20 μC/cm$^2_{pt}$ and -10 μC/cm$^2_{pt}$ in sulfuric acid and perchloric acid, respectively. This effect is assumed to be negligible.[62–64] Integrating the area underneath the hydrogen desorption region (**Figure 1.3.b**) and considering the first assumption (*i.e.* 210 μC/cm$^2_{pt}$ needed for hydrogen desorption) provides the ECSA. CO stripping method is based on the required charge density to electrooxidize a monolayer of adsorbed CO (CO_{ads}) on one cm^2 of Pt which is Q_{OX} in the equation and is 420 μCcm$^{-2}_{Pt}$.[59,65,66] (see **equation 1.8**)

$$ECSA_{CO} = \frac{Q_{CO}}{Q_{Ox}} \qquad (1.8)$$

where Q_{CO} is the active surface of the catalyst which is obtained with the area underneath the peak seen in **Figure 1.4**, seen at the potential of *ca.* 0.7 V vs. RHE. Chattot *et. al.*[67] widely discussed

the potentials at which the CO-stripping peak appears for various Pt-based nanostructures. The shape and the position of the CO_{ads} stripping peak is strongly dependent on the alloying and surface defectivity of Pt-alloys.

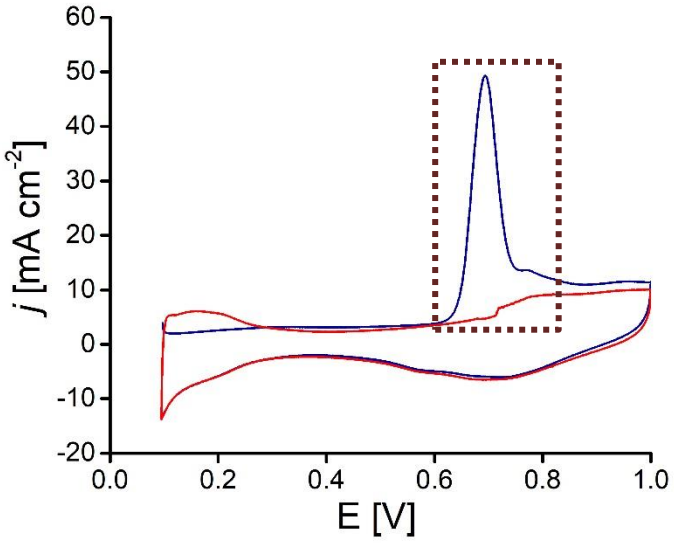

Figure 1.4 *Generic voltammogram of pre-adsorbed CO (CO_{ad}) on Pt/C*

1.3.1 Decreasing the Pt Loading – Pt Utilization

Decreasing the loading of Pt (in milligrams per geometrical surface area or mg/cm^2_{geo}) in the electrocatalysts can be achieve either by *(i)* optimizing the Pt utilization (*i.e.* thus increasing the activity by gram of platinum) or by *(ii)* alloying it with other metals (*i.e.* thus increasing the activity per atom of platinum and, therefore, the overall activity of the electrocatalyst),[14,68] *(iii)* shaping structural defects, *etc*. Optimizing the platinum utilization go through an optimization of the electrode preparation methods. There are different methods to fabricate Pt electrodes including low-loading platinum electrodes, of which, is to apply the ion carrier (generally Nafion®) into the catalyst layer.[69,70] This can be done by spraying, brushing or floating/dipping the electrode in the

ionomer solution.[71] However these methods suffer from inhomogeneity of distribution of the ionomer.[72] Sputter deposition is the method that has been commercially used and provides the highest Pt utilization.[73] Other methods include mixing of the supported catalyst with the ionomer in the presence of glycerol which keep the particles in the suspension and avoids agglomeration.[14,74] To achieve a uniform distribution of the ionomer on the catalyst particles, the ionomer can be converted into a colloid solution by adding a proper organic solvent followed by the addition of the ionomer to the supported catalyst.[75] In addition, the distribution of the nanoparticles on the carbon support should be as homogenous as possible, with little agglomeration. To achieve so, Fang *et al.*[76] used polyol synthesis process with ethylene glycol (EG) as the reducing agent. They reached ECSA of 78 $m^2g_{pt}^{-1}$, with 78% of Pt utilization. Polyol synthesis method proved highly effective in synthesizing catalysts with high loadings of platinum. (up to *ca.* 60 wt. %). Coating the surface of the carbon support with poly-benzimidazole[77] or PTFE[78] was also investigated to *(i)* improve the homogeneity of the ionomer and *(ii)* prevent Pt NPs formation in the inaccessible pores, thus increasing the Pt utilization. The latter is claimed to improve the ECSA by a factor of 33%.[79]

Low Pt loading and, thus, decreased available Pt area and accessibility often induces severe performance losses, partly due to the local oxygen transport resistance.[80] Two driving forces for oxygen transport through different components of the CCL are the total pressure (that causes Fiskian resistance (R_F) through larger pores) and the concentration difference (that causes non-Fiskian resistance (R_{NF}) due to diffusion through smaller pores or liquid films). *Knudsen diffusion* is a pore size-dependent transport phenomenon where in pores smaller than 100 Å, collisions of the diffusing molecules with the pore walls are more than the collisions of the molecules with each

other (otherwise known as the mean free path). At this condition, the molecules temporarily adsorb on the walls of the pores and then "re-emit" in different directions.[81,82] Specifically, R_{NF} consists of resistance in small pores in *(i)* microporous layer (MPL), *(ii)* in cathode catalyst layer (CCL) and *(iii)* resistance in the region close to (or at) the Pt surface (R^{Pt}_{O2}).[53] R^{Pt}_{O2} dominates the oxygen transport resistance for low-platinum loading electrocatalysts and decreases with an increased Pt ECSA.[83–85] For catalysts with a certain mass activity, the one with higher ECSA will have a better voltage performance due to less flux of oxygen necessary to fully perform the reaction.[86] Nonetheless, by placing all Pt atoms on the surface (*i.e.* maximizing the ECSA by producing a Pt-monolayer catalyst), using half of the Pt used in a Pt-alloy/C catalyst, performances can be matched.[54] On the other hand, maximizing the ECSA requires much smaller Pt NPs which come at the cost of performance depreciation considering low coordination of oxygen atoms that causes excessively strong binding of ORR intermediate species to the surface of Pt.

Alloying Pt with other transition metals is also regarded an immediate solution to decreasing Pt usage in electrocatalysts. Reportedly, Pt-alloys like Pt_3Sc that have been synthesized using colloidal polyol method, have shown promising ORR activities and high ECSA of 102.1 $m^2g_{Pt}^{-1}$.[47] Improved PtCo alloys have also been used to further reduce the Pt usage in fuel cells.[87] Gröger *et al.*[88] published an extensive review over different types of platinum electrocatalyst reduction strategies, *i.e.* alloying of Pt with other transition metals and dealloyed catalysts,[89,90] platinum monolayers over core-shell substrates[91,92] and nanostructured thin films[93], *etc.* However, those complex structures (*i.e.* platinum monolayers, nanostructured thin films, *etc*.) presents specific challenges related to their implementation in fuel cells, that will not be discussed throughout this report.

1.3.2 Kinetic Isotope Effect

However, little is known on how the changes in loading are impacting the ORR mechanism. To investigate such mechanistic changes, the kinetic isotope effect (KIE) can be used. The KIE studies assess the changes in kinetics between deuterated and water-based electrolytes (*e.g.* 0.5 M D_2SO_4 + D_2O *vs.* 0.5 M H_2SO_4 + H_2O) through the calculation of the rate constant ratio, *i.e.* KIE = k_H/k_D, indicating whether or not a proton is involved in the studied mechanism (here, ORR) rate determining step. The constant rate ratio can be calculated either by extracting the constant rate from the Koutechy-Levich equation (in the diffusion-limited region of the ORR, using a rotating electrode setup) or from the Tafel slopes. A KIE of 1 indicates that there is no difference in the reaction rates when H^+ or D^+ are involved in the ORR. Hence, the RDS is not proton dependent. A KIE under 1 (e.g. an inverse KIE effect) is rarely observed and often induced by the longer O-H bonds compared to that of O-D, resulting in a more occluded site for the reactive species.[94] A KIE over 1, results from a proton involvement in the RDS. This is observed for Fe-N-C electrocatalysts (KIE = ca. 2 –3; see Malko *et al.*[95] and Tse *et al.*[96]), unlike Pt electrocatalysts. Yeager et al.[97] were the first to show no kinetic isotope effect on Pt electrocatalysts in deuterated phosphoric acid (KIE = 1). (See also, Tse *et al.*[98]) This absence of KIE on Pt indicates that protons are not involved in the RDS of the ORR on platinum. Specifically, the first protonation of the oxygen can be further described by **Equations (8-10)**, with the RDS being the electron transfer:

$$O_2 \leftrightarrow O_{2,ads} \quad (1.9)$$

$$O_2 + e^- \leftrightarrow O^-_{2,ads} \quad (1.10)$$

$$O^-_{2,ads} + H^+ \leftrightarrow OOH_{ads} \quad (1.11)$$

1.4 Effect of the Carbon Support

Carbon supports play a fundamental role in the electrocatalyst stability and activity and different types of carbons have been used as support since the 1970s.[99] One of the common ways to categorize the carbon supports are based on their morphologies (*i.e.* in plane or out of the plane graphitization [L_a and L_c respectively] and interplanar distance [d_{002}])[100,101] which shows the crystallinity of the carbon.[102–106] The carbon supports graphitization is important from the point of its inverse relation to surface area, thus the pore size available. Carbon support must function as the provider of proper pore structure and hydrophobicity in order to minimize the catalytic layer resistance and assist in the gas transport.[107] There are different types of pores, *i.e.* primary pores or mesopores (<0.1 μm) in which the ORR takes place and larger inactive secondary pores that are otherwise known as micropores[108] (see **Figure i.4.**). For the optimal ORR reaction, we need active Pt surface, located in a primary pore where there is an adequate presence of oxygen through an optimized thickness of Nafion® film, thus, sufficient proton availability as well as electron conductivity. This optimal point is referred to as a three-phase point (see **Figure 1.5.**). Finally, the importance of high surface area while having the least possible micropores is essential characteristics of the carbon support.[109]

Effective distribution of Pt NPs allows us to increase the loading of Pt on the carbon surface without any significant loss of Pt utilization. However, increasing Pt loading, also enhances the oxidation reaction of the carbon support at potentials below 1 V vs. RHE, i.e. when the Pt is not under its oxidized form and thus can contribute to the $CO_{ads} \rightarrow CO_2$ intermediate step.[110–112] As a result, the optimum carbon support should have a high degree of graphitization to resist oxidation throughout its operating range.[113,114]

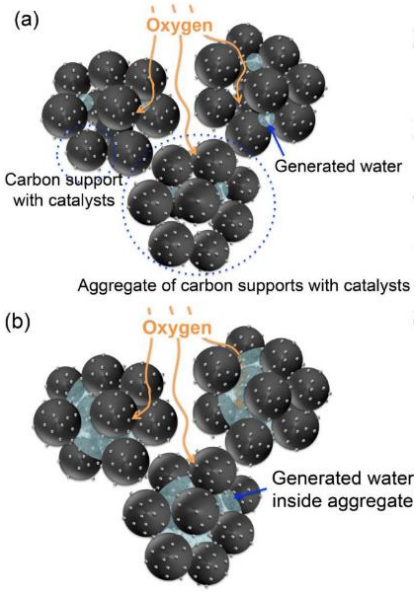

Figure 1.5 *Pore distribution of carbon black, shown with water generation in mesopores (primary pores) (a) and in micropores (Secondary pores) (b)* [242]

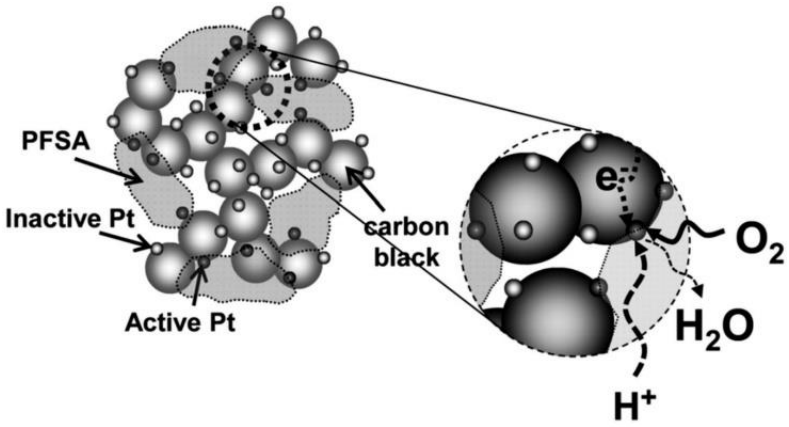

Figure 1.6 *A schematic depiction of the three-phase point in the catalyst layer, including carbon supported Pt NPs, ionomer and the path for the gas diffusion*[243]

The carbon support oxidation reactions are kinetically dependent on the physical and chemical properties of the carbon support and external conditions like temperature and electrode potential.[115–117]

The reactivity of the Pt electrocatalysts for the ORR is also impacted by the nature of their support. Lim *et al.*[118] have shown that a defective graphene support reduces the activation energy of the rate determining step of the ORR from 0.37 to 0.16 eV on the Pt nanoparticles supported on said support. A wide library of carbon supports, including carbon blacks of different specific surfaces,[119] carbon nanotubes and graphene nanosheets,[120] metal oxides,[121] *etc.* have been used as support for Pt nanoparticles for the ORR, with a special attention to their stability in fuel cell conditions.

1.5 Ionomer

Another CL component that impacts the PEMFC performances is the ionomer. Ionomer limitations have recently become a subject of research alongside low-Pt-loaded cathodes.[53] The ionomer (bulk or thin films) and water (produced during the ORR), introduce an additional source of oxygen transport resistance. Shortly, the resistance observed at the cathode is equivalent to a *ca.* 35 nm-thick-layer of the ionomer film, *i.e.* much larger than the 2 – 10 nm films that are used in current cells designs, hence underlining that the ionomers properties are modified when implemented in the membrane electrode assembly. As an example, the O_2 transport resistance through the ionomer is 3–10 times higher in the catalytic layer than in *ex-situ* ionomers thin-films. Hence, the increase of resistance is likely arising from the *in-situ/operando* ionomer thin-film having a different structure than the *ex-situ* thin-film ionomer.[84] This motivates numerous attempts to characterize

the ionomer thin-film inside the MEA.[122–124] Increasing the ionomer content will increase both bulk and local oxygen transport resistance due to diverse morphologies of the ionomer. This means excessive ionomer can form invalid pores which add up to bulk resistance and aggregated ionomer on Pt surface can prolong diffusion of oxygen to the surface of the active site, which increases the local resistance (**Figure 1.7**).[125]

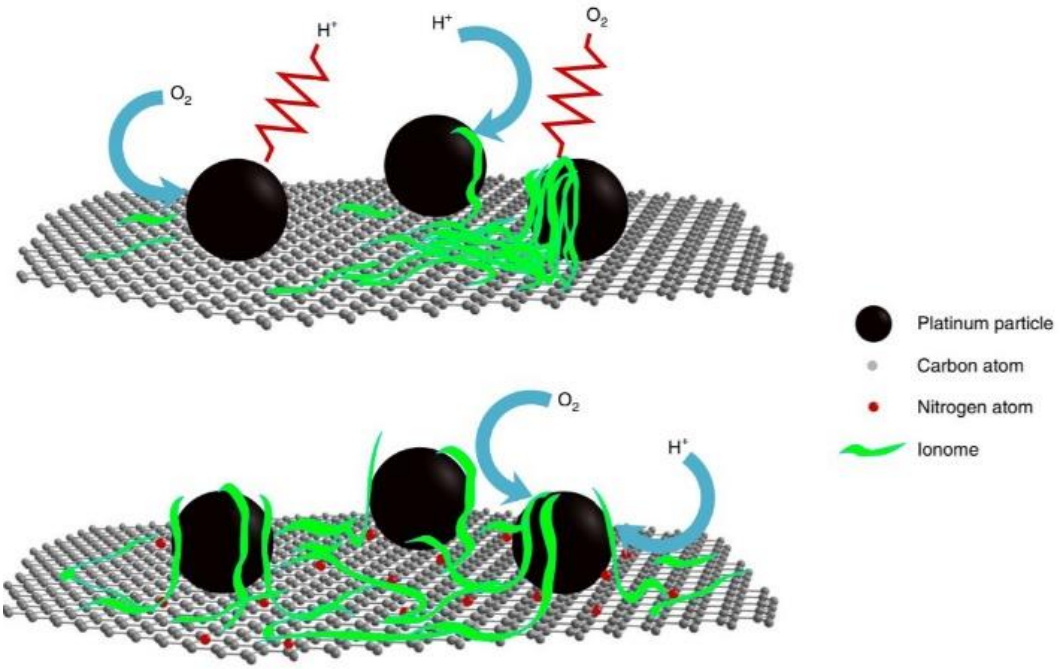

Figure 1.7. Schematic illustration of the ionomer distribution and thickness over the Pt/carbon surface (top) and a modified Pt/N-carbon surface (bottom) with respect to the effect of proton conductivity and O2 mass transport. (from reference[126])

Achieving a decreased local oxygen transport, thus requires a better understanding of *(i)* the ionomer dispersion onto the electrocatalyst surface (*i.e.* homogeneous *vs.* clusters), of *(ii)* the exact surrounding of an active site in MEA (*i.e.* does the ORR occurs through a triple-phase boundary or O_2 diffusion through the ionomer) and of *(iii)* Pt-ionomer interactions. Sulfonate groups on the ionomer (Nafion®) have been found to adsorb on Pt-surface and reduce the ORR activity while at the same time, this adsorption leads to immobilization of the ionomer chain and further confines

the ionomer. This confinement makes the ionomer lose its ability to phase segregate (phase segregation gives the ionomer the ability to form separated polymer and water domains, thus provide a path for oxygen diffusion) that impedes the oxygen transport.[53] Additionally, the electrostatic interactions (*i.e.* the effect of the platinum zero charge potential and its variation throughout the potential range) between the ionomer and the platinum nanoparticles should not be overlooked, as they can results in displacement of the ionomer film.

1.6 The interfaces of catalyst/ionomer and ionomer/carbon support

The limiting current densities of different loadings of Pt/C electrocatalysts has shown an inverse relation between the Pt loading and ORR kinetics. This phenomenon is typically attributed to the increase in oxygen transport resistance and reduction in Pt specific surface area.[55,80,82,85,127–130] To have a complete three-phase point the reactive sites need to be at least partially covered with ionomer. The ionomer thin film shows properties different than that of bulk ionomer (*i.e.* polymer electrolyte membrane [PEM]) due to the thickness of the ionomer layer approaching the characteristic length of the material. It is shown that water uptake inside the catalyst layer (CL) increases with the increasing Pt loading of the electrocatalyst and the ionomer content of the CL which, in turn, causes an increase in wettability and hydrophilicity. However, it is also shown that the general water uptake is depressed in the CL.[122,131] **Figure 1.8** demonstrates water uptake isotherms for Nafion in various PEMFC catalyst layers as a function of relative humidity compared with that of bulk Nafion [132,133]

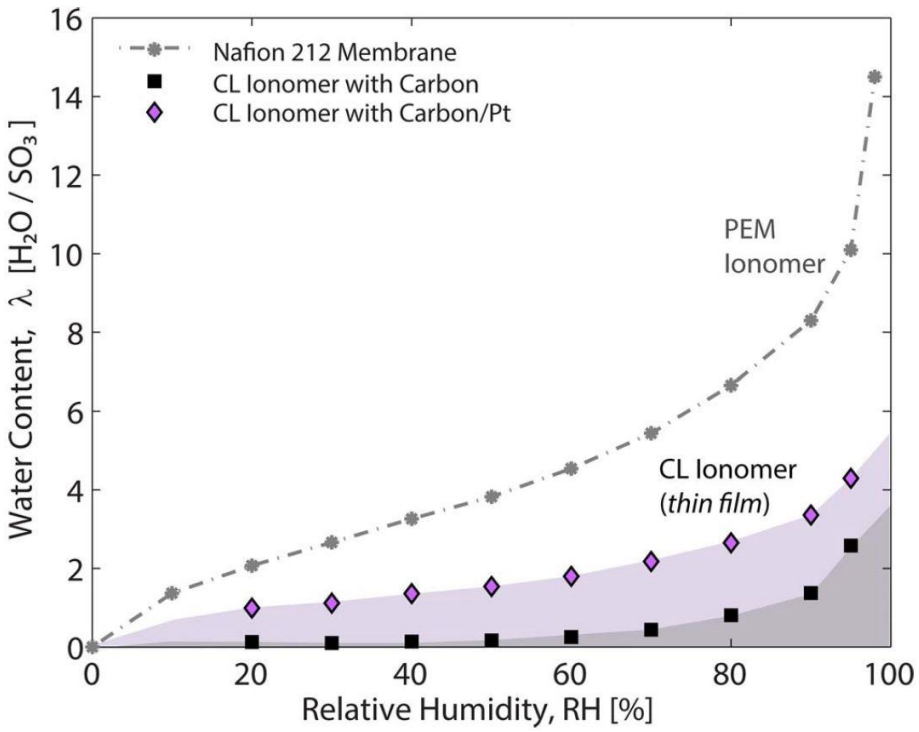

Figure 1.8. Water-uptake isotherms for Nafion in various PEMFC catalyst layers as a function of relative humidity compared with that of bulk Nafion membrane[132]

1.7 Gas Permeation

Another notable challenge on the fuel cell systems is the challenge of gas permeation. The most important part is H_2 crossover specially at low current densities that can cause faradaic losses[134] along with safety issues[135] and degradation.[136] In addition to PEM side chain degradation, CF_2 backbone can also chemically attack the membrane and cause extreme fluorine losses and increase H_2 crossover.[137] Hydrogen permeability at high current densities and intrinsic membrane permeability are negligible but at low current densities specially at the open circuit voltage (OCV) the unfavorable impact of H_2 crossover is detrimental.[138] H_2 crossover is a diffusion dominated process[139] that is facilitated by using thinner polymer membranes[140] (*i.e.* ca. 20 μm for current membranes), operating at higher temperatures and pressures[141] and the water content[101] in the membrane. The H_2 flux across the fuel cell is given in the literature[103] with the following **equation**:

$$J_{H_2}^{ccross} = \left(\frac{K_{H_2} D_{PEM}}{l_{PEM}}\right) \times P_{H_2}^{a} \quad (1.12)$$

where J_{H2} is the flux of hydrogen across the cell, K_{H2} is the partial pressure-related solubility coefficient of H_2 and P^a_{H2} is the hydrogen partial pressure. From this permeability coefficient is defined as follows:

$$\varphi_{H_2} = K_{H_2} \times D_{PEM} \quad (1.13)$$

which is a function of pressure, temperature, relative humidity, water content and the nature of the membrane. It is more strongly dependent on temperature than other aforementioned factors.[143]

1.8 Objectives

Here, we aim to understand how our 'optimized' electrocatalyst will interact with the solid electrolyte (i.e. poisoning of the active sites, backbone/nanoparticles interaction, etc.) and if it can be successfully implemented in a PEMFC. The aim is to create a matrix of carbon supports of differing specific surface areas as a support material on which we deposit different loadings of Pt NPs (*i.e.* 3.5/14/30/maximum wt.%). Characteristics such as durability, catalyst distribution, and electrochemical performance will be investigated on these sets of electrocatalysts. TEM images can provide the particle size distribution in the catalysts which is a useful input for the physical state of the electrocatalysts.[144] Electrochemical characterizations of the catalysts will be the set of data, providing evidence on how the interactions of the ionomer with the electrocatalyst (*i.e.* the surface density of the Pt NPs, ECSA, *etc.*) and with the carbon support will project on the performance of the electrocatalyst. Considering that, the carbon supports which have shown a KIE are expected to have different interactions than supports which have not shown a KIE effect, which

is why one of each carbon support (with and without KIE effect) was selected for further investigation on the effect of Pt loading and proximity effect on ORR.

1.8.1 Thesis Objectives

In this project, we started with the effect of carbon supports on the rate-determining step of the oxygen reduction reaction. In this objective we used kinetic isotope effect as a tool to investigate proton involvement in the RDS of the ORR. The resulting publication from this investigation is brought in *chapter 2* of this document. Furthermore, we moved on to eliminate this effect using different loadings of Pt on two selected carbon supports one of which showed KIE effects and the other showed no effect of proton in the RDS of the ORR, thus, no KIE. Moreover, we integrated the in-house made electrocatalysts with the maximum loading, into a membrane electrode assembly (MEA) system to test their durability and electrochemical performance in an automotive condition operated fuel cell test station. This is the topic of *chapter 3* in this document. We followed the research by probing the heterogenous degradation of electrocatalysts in a polymer electrolyte fuel cell (PEFC) system under realistic automotive conditions using multi-modal techniques. The resulting publication from this investigation is shown in *chapter 4* of this document.

Chapter 2

Kinetic Isotope Effect as a Tool to Investigate the Oxygen Reduction Reaction on Pt-based Electrocatalysts

Part II: Effect of the Platinum Dispersion

2.1 Introduction

The recent energy crisis induce a need for sustainable energy sources both in large and small scales, [1,2] such as wind turbines, solar and photovoltaic cells, and fuel cells. [3] Among them, the proton exchange membrane fuel cell (PEMFC) can satisfy the energy need with the least anthropogenic impact on nature. [4] However, it suffers from great costs, partly induced by its expensive catalytic material, platinum, necessary to catalyze the oxygen reduction reaction (ORR) occurring at the cathode. Hence, it becomes essential to either synthesize electrocatalysts without platinum (but achieving similar performances), or to maximize the performance of the fuel cell per unit mass of platinum (ultra-low loadings) [145] by increasing the exposure of its active sites for the ORR. [50,51] The ORR has been widely studied in the literature. It can take place through two different pathways: [43,44] the 4-electron transfer pathway or a series of 2-electron transfer reactions, both of which are shown below:

4-electron pathway:

$$O_2 + 4H^+ + 4e^- \leftrightarrow 2\,H_2O \qquad (2.1)$$

2-electron pathway:

$$O_2 + 2H^+ + 2e^- \leftrightarrow H_2O_2 \qquad (2.2)$$

Peroxide can undergo further reduction or decomposition in acidic solutions[146] with the following reactions:

$$H_2O_2 + 2H^+ + 2e^- \leftrightarrow H_2O \quad (2.3)$$

$$H_2O_2 \leftrightarrow H_2O + {}^1/_2\, O_2 \quad (2.4)$$

On platinum, the rate-determining step (RDS) of the ORR, is often admitted as the oxygen first protonation, [46] *i.e.*

$$O_2 + H^+ + e^- \leftrightarrow OOH_{ads} \quad (2.5)$$

Throughout the years, platinum nanostructures, along with their supports, have been optimized to achieve better performance. [147] The mechanisms at stake beneath those activity enhancements have been studied by several methods, including the following calculations: *(i)* correlating the binding strength of oxygen intermediates and the reactivity; [148,22] and *(ii)* classic electrochemical methods such as Tafel slopes analysis. [149] Another technique of interest is based on the kinetic isotope effect (KIE). [150] It consists of studying the ratio of the reaction rates caused by the substitution of hydrogen with deuterium, [151,152] given by

$$KIE = \frac{k_{ORR,H_2O}}{k_{ORR,D_2O}} \quad (2.6)$$

A KIE of 1 indicates that there is no difference in the reaction rates when H^+ or D^+ are involved in the ORR. Hence, the RDS is not proton dependent. A KIE under 1 (*e.g.* an inverse KIE effect) is rarely observed and often induced by the longer O-H bonds compared to that of O-D, resulting in a more occluded site for the reactive species. [94] A KIE over 1, results from a proton involvement in the RDS. The KIE usually ranges from 1 – 7, although KIE up to 16 have been observed, and

can be subdivided in two categories, *i.e. (i)* KIE = 1 – 2, often referred as a 'secondary KIE', implies a modification of the rate determining step when shifting from H_2O-based electrolyte to D_2O-based electrolyte, but this rate determining step does not involve the breaking of a O-D/O-H bond. The exact maximal value of the secondary KIE (here, 2) is highly debatable. Christensen and Fristrup[153], based on Westheimer works, considered as the secondary KIE maximal value 1.2 and that the 1.2 < KIE < 2.0 induce a full breaking of the X-H/X-D bond (X being the other element connected to the H/D) but that the observed KIE is heavily decreased due to the linear symmetry of intermediate complex involved in the RDS. However, 1 < KIE < 2 has been observed for reaction involving nonlinear molecules (*e.g.* a KIE of 1.4, has been observed during the formation of fluorenone by the diazotization of *o*-phenylbenzylamine), and thus, another hypothesis is that the X-H/X-D bond is only partially broken at KIE < 2. [154] This underlines the complexity of assessing a KIE < 2 for the oxygen reduction reaction, as it could be indicative of a RDS involving the breaking of the O-H/O-D bond, but with a peculiar symmetry, or of the involvement of the proton in the rate determining step, but without implying the breaking of an O-D/O-H bond; *(ii)* KIE = 2 – 7, the 'primary KIE', for which the O-D/O-H bond is broken, or formed, during the rate determining step. [153] A KIE is observed for Fe-N-C electrocatalysts (KIE = *ca.* 2 –3; see Malko *et al.* [95] and Tse *et al.* [96]), unlike Pt electrocatalyst. Yeager *et al.* [97] were the first to show the absence of a kinetic isotope effect on Pt electrocatalyst in deuterated phosphoric acid (KIE = 1). This absence of KIE on Pt indicates that protons are not involved[44] in the RDS of the ORR on platinum. This result has been confirmed by George *et al.*[155], in the first part of this paper, who investigated the kinetic isotope effect on commercial, 40 wt. % Pt/C (HiSPEC 4000) and platinum extended surfaces (poly-Pt). They observed, both in sulfuric-based and perchloric-based electrolytes, the absence of a KIE, hence implying that, on highly Pt loaded and Pt extended surfaces, the rate

determining step is not proton dependent. Additionally, it also indicates that the proton involvement in the rate determining step is also independent of the electrolyte nature, and more specifically, of the presence of Pt poisoning species such as SO_4^{2-}.

The first protonation of the oxygen can be further described by **Equations 7 – 9**.

$$O_2 \leftrightarrow O_{2,ads} \quad (2.7)$$

$$O_{2,ads} + e^- \leftrightarrow O_{2,ads}^- \quad (2.8)$$

$$O_{2,ads}^- + H^+ \leftrightarrow OOH_{ads} \quad (2.9)$$

According to George *et al.*[155] findings, this implies that the rate determining step on highly Pt loaded and Pt extended surface is either the O_2 adsorption (**Equation 7**) or the electron transfer (**Equation 8**). As previously stated, the reactivity of the platinum electrocatalysts for the ORR is also impacted by the nature of their support. A wide library of carbon supports, including carbon blacks of different specific surfaces,[119] carbon nanotubes and graphene nanosheets,[120] metal oxides,[121] *etc.* has been used as supports of Pt nanoparticles for the ORR, with a special attention to their stability in fuel cell conditions. Indeed, carbon suffers from corrosion under fuel cell conditions like start-up and fuel starvation.[33] Higher graphitic content of the carbon support leads to a better resistance of the support to corrosion.[34] Lim *et al.*[118] explained that defective graphene support reduces the activation energy of the rate determining step of the ORR from 0.37 to 0.16 eV on the platinum nanoparticles, which lowers the energy barrier of the RDS by decreasing the stability of the hydroxyl groups. Hence, the carbon nature seems to play a key role on Pt reactivity toward ORR. In this paper, we are investigating the modification of the ORR mechanism (using the KIE) on Pt nanoparticles supported on various carbon blacks. In addition, the electrocatalysts were fully characterized using various techniques, including, but not limited to, Raman

Spectroscopy, X-ray diffraction (XRD), transmission electron microscopy (TEM), X-ray photoelectron spectroscopy (XPS) and near ambient pressure XPS (NAP-XPS).

2.2 Materials and Methods

2.2.1 Preparation of Pt/C catalysts

The Pt nanoparticles were synthesized using the polyol method, which has been thoroughly elaborated in previously published works by multiple researchers.[156,157] Briefly, the process is as follows. Pt salt (H_2PtCl_6-xH_2O 99.995% trace metals basis, Sigma Aldrich) was dissolved in a solution of 2:1 deionized water (18.2 MΩ) and ethylene glycol. The solution was then brought up to pH=12.5 and stirred under inert atmosphere (Argon) for 1 hour. Then, the temperature was risen to 120 °C for 3 hours while stirring, thus leading to the formation of a platinum nanoparticles colloid. In the meantime, the carbon support (FCX080, FCX100, FCX200, FCX400 and FCX800, provided by Cabot®) was dispersed in a solution of 1:1 deionized water and ethylene glycol, aiming for a loading of 20 wt. % of platinum on the carbon support (or 30 wt. % for Pt/FCX080). The two solutions were mixed and considering the zeta potentials of the support and the Pt NPs,[158,159] the final solution's pH was brought down to 2.5, and then stirred for 22 hours. The solution was then filtered, washed and dried in the oven for 45 minutes at 110 °C, resulting in the Pt/C electrocatalysts discussed in this work. In addition, a commercial Pt/C (40 wt. % Pt on Vulcan XC72R Carbon, Sigma Aldrich) was purchased and used for comparison.

2.2.2 Physicochemical characterizations

X-ray diffractions were obtained using a Rigaku Smartlab diffractometer, equipped with a D-Tex Ultra silicon strip detector in a Bragg-Brentano focusing geometry. The X-ray source was Cu k_α and the k_β beams were filtered using a nickel filter slit. The sample holder was a zero-background quartz holder and scanned from 10° to 150° at a scan rate of 7° min^{-1}. MDI JADE 2010 software was used to perform whole-pattern refinement using Pt phase data from the ICSD database as a reference. Raman spectroscopy was performed using a confocal Raman microscope WITec Alpha 300R equipped with a 532 Nd-Yag laser, WITec UHTS 300 spectrometer, Andor, DV 401 BV CCD camera and objective (x20, NA = 0.40). Aberration-corrected scanning transmission electron microscopy (AC-STEM) characterization was performed using a JEOL Grand ARM300F with two spherical aberration correctors at 300 kV for both probe-forming and TEM imaging. Analysis of particle size and particle size distribution was done using ImageJ software. Near Ambient Pressure X-ray Photoelectron Spectroscopy (NAP-XPS) were performed at soft XPS Beamline 9.3.2 in Advanced Light Source at Lawrence Berkeley National Laboratory. First, C1s and Pt4f spectra were acquired using 550 eV X-ray source in ultra-high vacuum (UHV)for calibration. For adsorption studies, 280 eV X-ray source was used for all spectral acquisition. To remove pre-adsorbed species from the surface of catalysts, a cleaning step was performed at 150 °C in UHV. Pt4f spectra were then acquired at 80 °C in UHV, followed by sequential data collection in an oxygen atmosphere of 0.1 Torr pressure at 80 °C, and back at UHV at the same temperature. All spectra were obtained at 100 eV pass energy. The protocol for data acquisition, processing and data interpretation is based on previously published thorough study of detecting changes in NAP-XPS spectra due to gas adsorption.[160]

2.2.3 Electrochemical characterizations

Electrochemical studies were performed using a Pine Instrument Company electrochemical analysis system in a three-electrode cell containing either 0.5M H_2SO_4 electrolyte (VWR, Omnitrace®, in H_2O, 18.2 MΩ) or 0.5M D_2SO_4 electrolyte (96 - 98 wt.%, Sigma-Aldrich, in D_2O, Sigma-Aldrich 99.9 at.%, without further purification, as the purity of the D_2O has little impact on the kinetic isotope value in acidic environment, according to the recent findings from Sakaushi[161]) saturated at room temperature with either O_2 or N_2 depending on the test goals. A carbon-rod counter electrode and Ag/AgCl reference electrode (0.198 V *vs.* Reversible Hydrogen Electrode – RHE) were used as the two components of the 3-electrode cell, whereas the third component was a working electrode, on which an ink containing the electrocatalyst was deposited. The ink was prepared by mixing 5mg of the Pt/FCX electrocatalyst with 1012 μL of deionized water, 477 μL of Isopropyl alcohol and 28.5 μL of Nafion^{TM} ionomer (5 wt.% solution, DuPont). The ink was briefly sonicated. Then, 20 μL were deposited onto a glassy carbon disk. After activation at 500 mV s^{-1} and characterization at 20 mV s^{-1} in N_2-saturated electrolyte, cyclic voltammetry was acquired between 400 to 2500 rpm with a scan rate of 5 mVs^{-1} using a rotating ring-disk electrode (RRDE). The ring potential was set to 1.1 V *vs.* RHE. (A representative sample of ring and disk currents versus potential is shown in **Figure 2.1**.) A current collection efficiency of 0.42 was used to calculate the H_2O_2 yield. The N_2-saturated electrolytes experiments in 0.5 H_2SO_4 were used to calculate the electrocatalyst surface area, using a desorption charge of H_{ads} per Pt of 210 μC cm_{Pt}^{-2}. The KIE was calculated using the O_2-saturated electrolyte measurements by determining the constant rate at the onset potential.

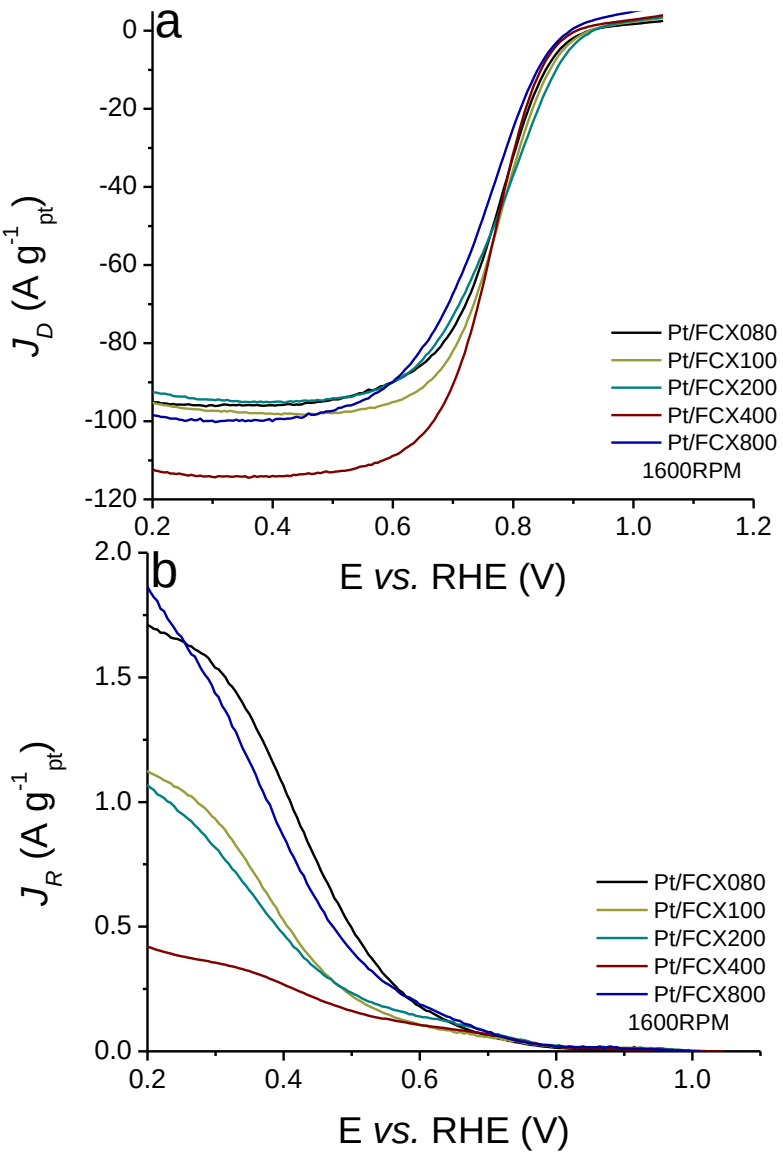

Figure 2.1 Rotating ring-disk electrode (RRDE) characterization of the electrocatalysts discussed in this chapter, in O_2-saturated 0.5 M H_2SO_4, with a scan rate of 5 mV s^{-1} and a rotation speed of 1600 rpm; disk current (a); ring current (b). It can be seen in the voltammogram that the PtFCX400 shows higher kinetic current plateau compared to the other samples. This experiment appeared to be reproducible, through several different syntheses onto Pt/FCX400 and while varying the experimental conditions. Hence, it was assumed to be induced by the intrinsic characteristics of the carbon support and not by the experimental procedure nor the Pt nanoparticles.

2.2.3.1 Kinetic isotope effect calculations

There are several methods to calculate the kinetic isotope effect (KIE), based on how the kinetic constant (k) was calculated. *Koutecky-Levich* equations are performed at the diffusion-limited region of the ORR and the method is based on the following equations:

$$\frac{1}{j} = \frac{1}{j_k} + \frac{1}{j_l} \tag{2.10}$$

$$j_{l,c} = 0.62nFD_{o_2}^{\frac{2}{3}}\omega^{\frac{1}{2}}\upsilon^{\frac{-1}{6}}C_{o_2}^{*} \tag{2.11}$$

$$j_k = nfk_fC_{o_2}^{*} \tag{2.12}$$

$$\frac{j_0^H}{j_0^D} \times \frac{1}{0.908} = \frac{k_0^H}{k_0^D} \tag{2.13}$$

Where j_l is the limiting current density (obtained experimentally), $C^*_{O_2}$ is the bulk concentration of oxygen, F is the Faraday constant, D_{O_2} is the diffusion coefficient of oxygen, ω is the rotation speed, v is the kinematic viscosity and n is the number of transferred electrons. Plotting j_l^{-1} vs. $\omega^{0.5}$ the inverse kinetic current (j_k^{-1}) can be calculated as it is the intercept and the slope of the plot gives 'n'. From there, Eq. 4 can be used to calculate the kinetics constant ratio and, therefore, the KIE.[98] The errors induced by this method arise from the fact that the calculations are performed far from the onset potential, which is when the current is transport limited and $j_k >> j_l$, therefore leading to extremely small values of j_l^{-1}, susceptible to inaccuracy. Another method for performing the KIE calculations is using the Tafel slopes.[149] The following equations, along with Eq. 4, are relevant when using this method:

$$\eta = T_s\, ln(j_0) - T_s\, ln(j) \tag{2.14}$$

$$j_0 = nfk_0C^* \tag{2.15}$$

Where j is the current density, j_0 is the exchange current density at either the onset potential of the reaction or at the equilibrium potential and T_s stands for the Tafel slopes, which were experimentally determined. Here, we established $\eta = 0$ at the onset potential, hence assuming that all limitations between the onset potential and thermodynamic equilibrium potential (*i.e.* 1.229 V

vs. RHE in H_2O, 1.249 V *vs.* RHE in D_2O) were not kinetically induced. This decision was made to avoid extrapolating the Tafel slopes over 4 current decades, which could induce dramatic imprecision on the calculations of the rate constant and, as such, that of the KIE. From **Equation 2.14** and **Equation 2.15**, the KIE effect can be calculated, using **Equation 2.13**. The assessment of j_0 was performed as presented in **Figure 2.2**. The experimental data, corrected for ohmic losses and the diffusion in solution (*i.e.*, j_k) were plotted as a function of the potential (see **Figure 2.2.A**). The onset potential was established as the potential at which the current dropped below the detection limit of the potentiostat. The Tafel slopes were measured over one decade of kinetic current from the potential corresponding to the inflexion point (see **Figure 2.2.B**) of the measured current data, as it is established that, over said inflexion point, the influence of the transport limitations on the measured currents leads to imprecision in the calculation of the kinetic current and, hence, in the resulting Tafel slopes.

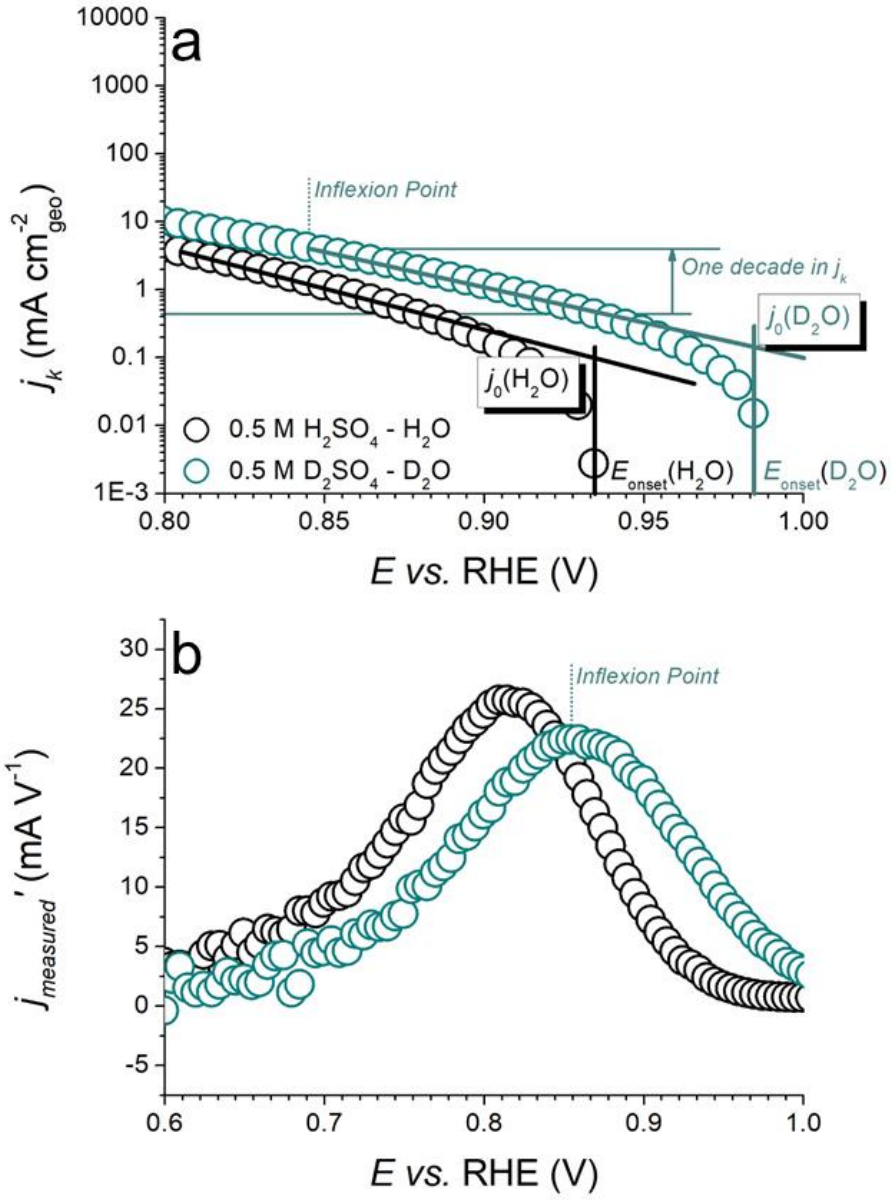

Figure 2.2 Illustration of the method used to calculate the current exchange density at the onset potential; (a) Tafel representation of the kinetic current vs. the potential in D_2O and H_2O-based solutions and (b) inflexion point observed for the measured current in D_2O and H_2O-based solutions.

2.3 Results and Discussion

Here, we focused on five different types of carbon black provided by Cabot®, described as FCX080, FCX100, FCX200, FCX400 and FCX800. The numbers correspond to an approximation of their specific surface, *i.e.* 77, 93, 134, 388 and 890 m^2 g^{-1}, respectively (see **Table 2.1**). As evidenced in **Table 2.1**, the changes in specific surface reflect in changes in micropores (d_{pores} < 2 nm), mesopores (2 nm < d_{pores} < 50 nm) and macropores (50 nm < d_{pores} < 300 nm). More specifically, the micropores and mesopores volume increase with the increasing specific surface, whereas the macropores volumes is roughly constant between FCX080, FCX100 and FCX200, before greatly increasing (from *ca.* 0.20 cm^3 g^{-1} to *ca.* 0.90 cm^3 g^{-1}) for FCX400 and FCX800. This implies that the electrocatalyst surface accessible for nanoparticles, with d = 2 – 3 nm, increases with the increase of the carbon overall specific surface.

Table 2.1. In-plane and out-of-the-plane graphitization, specific surface and pores volume (micropores correspond to pore size below 2 nm, mesopores to pore size between 2 – 50 nm and macropores to pore size between 50 and 300 nm) of the various carbon supports discussed in this work.

	S_{carbon} (m^2 g^{-1})	Micropores volume (cm^3 g^{-1})	Mesopores volume (cm^3 g^{-1})	Macropores volume (cm^3 g^{-1})	L_a (nm)	L_c (nm)
FCX080	77	0.01	0.14	0.19	5.3	6.6
FCX100	93	0.01	0.17	0.24	2.4	5.0
FCX200	134	0.02	0.18	0.22	2.7	2.9
FCX400	388	0.04	0.83	0.85	2.6	1.5
FCX800	890	0.20	1.03	0.95	3.6	0

Over a first phase, the physical properties of the carbon supports were investigated, using X-ray diffraction (XRD), Raman spectroscopy, scanning electron microscopy (SEM), scanning transmission electron microscopy (STEM) and N_2 adsorption. The XRD patterns of the supports are shown in **Figure 2.3a**. The typical features of carbon, *i.e.* the (002) and (100) planes, are observed at 2θ ~ 26° and 2θ ~ 43° for FCX080, respectively. This indicates a high 'out-of-the-

plane' graphitization[162] (L_c = 6.6 nm, see **Table 2.1**) which decreases with the increase of the carbon specific surface area (*i.e.* L_c = 1.5 nm for FCX400 and L_c = 0.0 nm for FCX800, see **Table 2.1**). Interestingly, the low out-of-the-plane graphitization arises from different carbon morphologies, as evidenced by the STEM micrographs (see **Figure 2.4**): L_c clearly decreases from FCX080 to FCX400, but the carbon stacking remains high for FCX800 (see **Figure 2.4e**). Hence, if the graphitic planes appear to have the same orientation by STEM, XRD indicates that, for FCX800, they are not stacked.

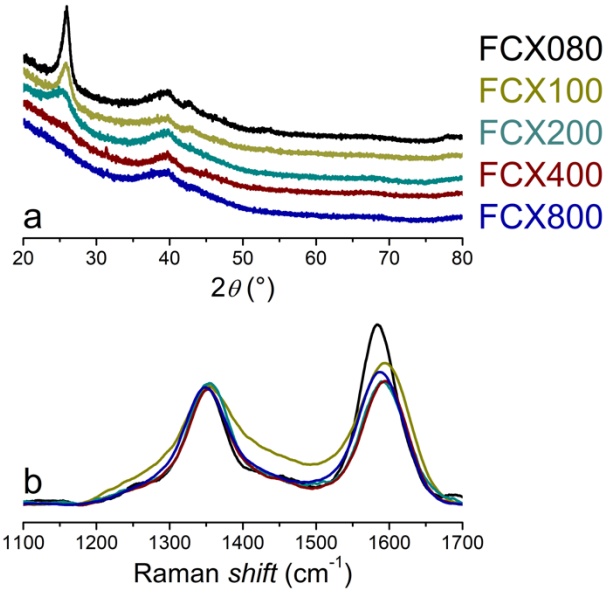

Figure 2.3. X-ray diffraction (a) and Raman (b) patterns of the various carbon supports discussed in this work.

Raman spectroscopy is very commonly used to characterize ordered and disordered crystal structures of carbonaceous materials in the crystallite plane.[163,164] For carbon, the characteristic bonds are observed at 1350 cm^{-1} (D_1-band)[165] and in the 1580 – 1610 cm^{-1} region (containing the D_2 – 1610 cm^{-1} – and the G-band – 1585 cm^{-1}). The D-bands correspond to the disordered graphene lattice in the plane or at the edge of the graphene sheet, whereas the G-band corresponds to the ideal graphene sheet. The patterns presented in **Figure 2.3b** are normalized with respect to the D_1-

band intensity. The 'in-plane' crystallite size (L_a) was calculated using the Knight & White equation[166] (see Eq. 2.16).

$$L_a = 4.4 \times {A_g}/{A_{D_1}} \qquad (2.16)$$

Where A_g is the area under the G-band, after fitting (using four Lorentzian peaks for D_1, D_2, D_3, *i.e.* amorphous carbon[165] and G) and A_{D1} the area under D_1-band, after fitting. The highest L_a are achieved for FCX080 and FCX800, *i.e.* the lowest and highest specific surface carbon (see **Table 2.1**). Such results confirm the STEM observations (see **Figure 2.5**), where a significantly higher in-plane graphitization appears to be achieved for those samples.

As shown in **Figure 2.5**, Pt nanoparticles (NPs) were deposited onto the various carbon supports. They were prepared following the polyol method[156], hence achieving identical NPs size for all electrocatalysts. The particle size, extracted from the STEM pictures, along with their crystallite size and the electrocatalysts loading are presented in **Table 2.2**. To thoroughly investigate the effect of the surface density of the nanoparticles onto the ORR, we increased the loading of Pt on the FCX080 (*i.e.* 30.9 wt. % *vs. ca.* 15 – 20 wt. %). As stated above, the NPs size is constant. This is confirmed by the carbon support independent crystallite size, that remains comprised between 1.4 nm and 2.1 nm (see **Table 2.2**). Hence, for Pt/FCX080 and Pt/FCX100, the higher particle size extracted from the TEM micrographs was ascribed to NPs agglomeration, due to low specific surface area of these two supports. Additionally, we performed XPS analysis on the electrocatalysts, prior and after platinum deposition. We observed that the NPs preferentially anchor onto the carbon support defects (*i.e.* on the edges of the carbon planes rather than on the planes), as evidenced by an increase of the carbon graphitic content observed in XPS data after

deposition of Pt NPs and the resulting decrease in the oxygen content. Indeed, because of the Pt NPs anchoring over the structural defects, the latter contribution to the XPS signal decreases, as the distance between the electrocatalyst surface and the structural defects is increased. Such phenomenon is detrimental to the long-term stability, as the defective edges of the carbon are more prone to corrosion than the carbon planes. In addition, preferential anchoring onto the oxygenated functional groups results in low-populated carbon planes and, thus, depreciated dispersion. Interestingly, the NPs anchoring seems to be independent of the carbon defectivity & functionalization on the FCX100 (see **Table 2.2**).

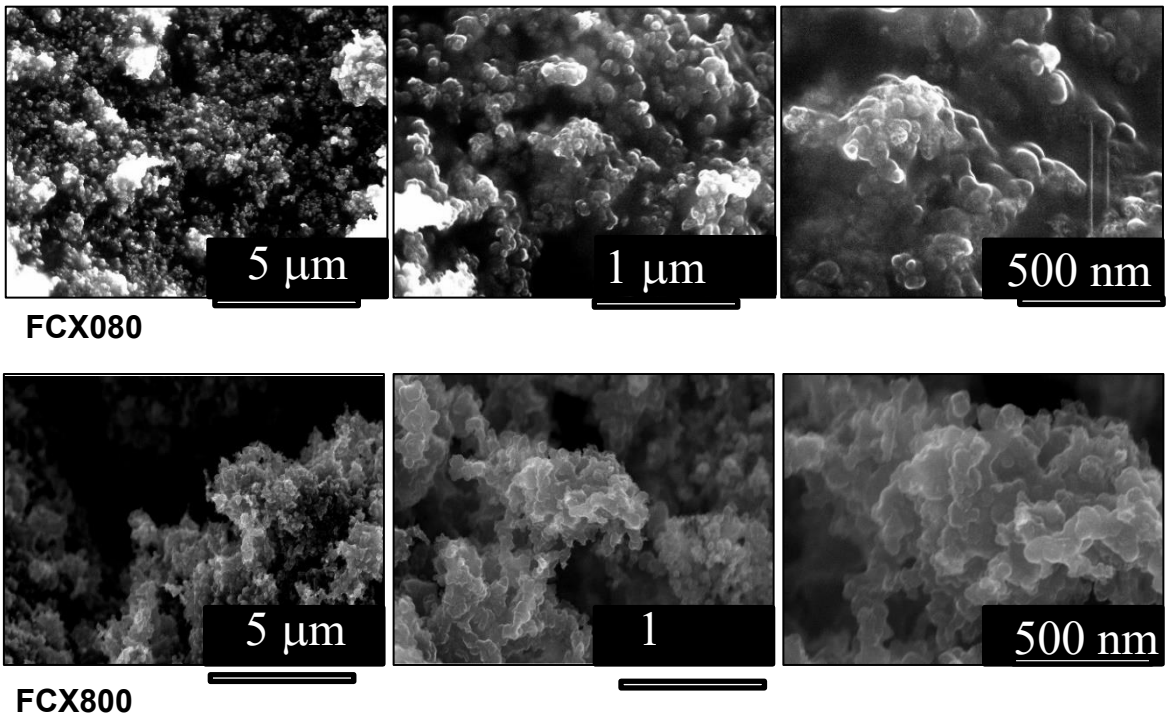

Figure 2.4 *SEM images of FCX100 and FCX400*

From SEM microscopy (See **Figure 2.4** for sample SEM imaging), all the five carbon supports investigated in this work, have an observable particle size distribution between 50 to 80 nm, with low surface area carbon supports on the higher end of this range and high surface area carbon supports on the lower value of the range. As stated earlier, oxygen rich amorphous domains are

more abundant in high surface area carbon supports where they provide more anchoring sites for Pt NPs to deposit, thus, better dispersion of active sites. The scarcity of anchoring sites in more graphitic carbon supports (*i.e.* low specific surface area) leads to a more agglomerated deposition of active particles. Since higher surface area carbon supports exhibit more accessibility of the Pt NPs, ionomer poisoning will be bigger of an issue in electrocatalysts fabricated using such supports.

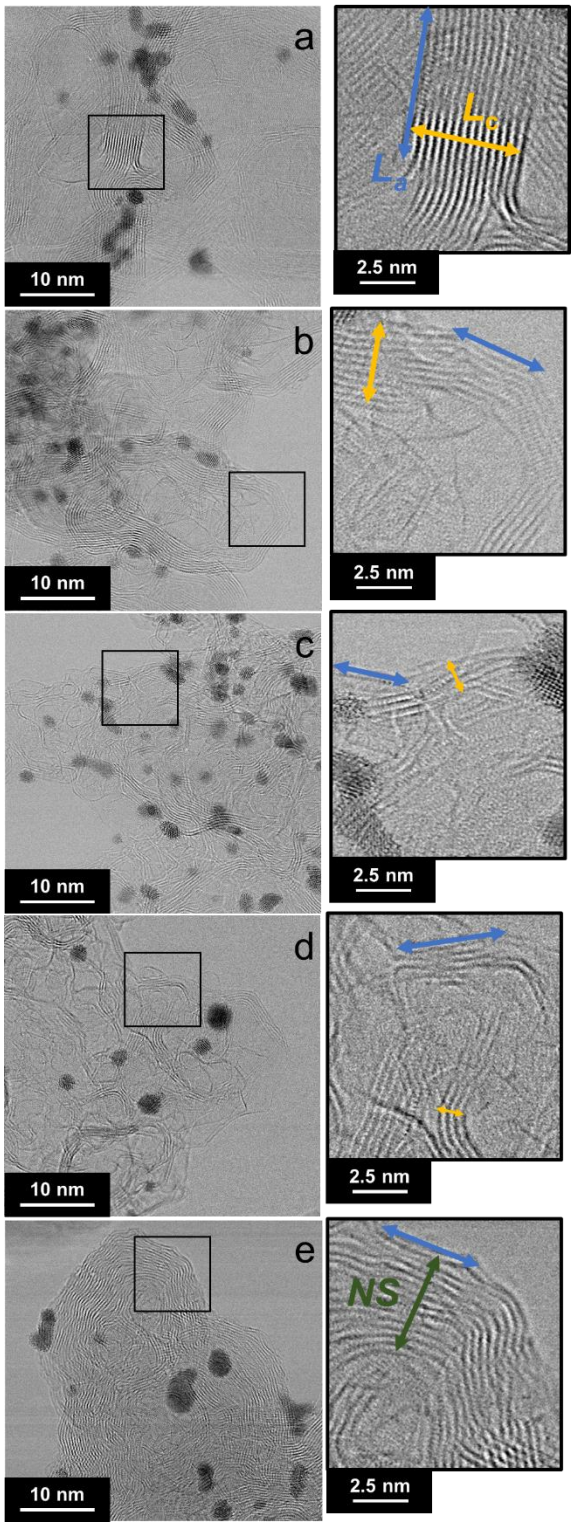

Figure 2.5 HR-TEM micrographs of Pt/FCX080 (a), Pt/FCX100 (b), Pt/FCX200 (c), Pt/FCX400 (d) and Pt/FCX800 (e). L_c and L_a corresponds to the crystallite size out and in-the-plane, respectively. 'NS' corresponds to a 'pseudo', but ultimately non-stacked (as evidenced in **Figure 2.3**) distance.

Table 2.2 Loading, particle & crystallite size of the Pt NPs and XPS data prior to and after the deposition.

	ICP (wt. %)	**d_{XRD} (nm)**	**d_{TEM} (nm)**	**XPS**			
				C_{gr} (%) (C)	C_{gr} (%) (Pt/C)	O% (C)	O% (Pt/C)
FCX080	30.90	1.5	2.5 ± 0.8	31.1	61.1	12.7	8.1
FCX100	20.20	2.1	2.5 ± 0.8	42.1	40.9	10.3	11.3
FCX200	16.10	1.6	2.1 ± 0.8	18.5	36.2	16.6	12.1
FCX400	21.30	1.8	1.9 ± 0.7	25.4	42.9	12.4	9.6
FCX800	18.20	1.4	1.9 ± 0.6	15.6	47.7	15.4	10.3

The electrocatalysts were then characterized in N_2 and O_2 saturated 0.5 M H_2SO_4, as summarized in **Figure 2.6**. The difference in the features in the hydrogen adsorption region (see **Figure 2.6a**), which refers to a range of potential from 0.05 to 0.40 V *vs.* RHE, is induced by changes in the agglomeration of the NPs and/or support-induced changes in the adsorption strength of protons on Pt (as mentioned above, the NPs originate from the same synthesis and, as such, are identical except for their agglomeration). The electrochemically active surface area (ECSA) of the different electrocatalysts was calculated using the H_{upd} region (see **Figure 2.6b**, where the current has been corrected for the double layer contribution) and are summarized in **Table 2.3**. It is important to note that: (i) despite an increased loading, the Pt/FCX080 presents a similar ESCA to Pt/FCX100 (42 $m^2\ g_{Pt}^{-1}$ vs. 47 $m^2\ g_{Pt}^{-1}$), and (ii) that the Pt/FCX400 presents an unexpectedly low specific surface area (46 $m^2\ g_{Pt}^{-1}$ as opposed to 70 – 74 $m^2\ g_{Pt}^{-1}$ for Pt/FCX200 & Pt/FCX800, respectively). These results are the average of 3 – 5 different experiments. From the ECSA of the electrocatalysts and the specific surface area of the carbon supports, a new parameter was introduced, $S_{carbon}/S_{Pt,H}$. This parameter is representative of the carbon coverage with Pt (a high $S_{carbon}/S_{Pt,H}$ ratio indicates that most of the carbon is free of Pt NPs, whereas a low $S_{carbon}/S_{Pt,H}$ ratio indicates that the carbon is mostly covered by Pt NPs). Two categories arise from these new parameters: *(i)* Pt/FCX080, FCX100, FCX200, with $S_{carbon}/S_{Pt,H}$ = 1.8 – 2, and *(ii)* Pt/FCX400, FCX800, with $S_{carbon}/S_{Pt,H}$ =

8.4 – 12.7. This ratio was also calculated for a commercial catalyst (Pt/C, Sigma Aldrich) with a similar loading than observed by George *et al.*[155], *i.e.* 40 wt. % and was $S_{carbon}/S_{Pt,H}$ = 3.1.

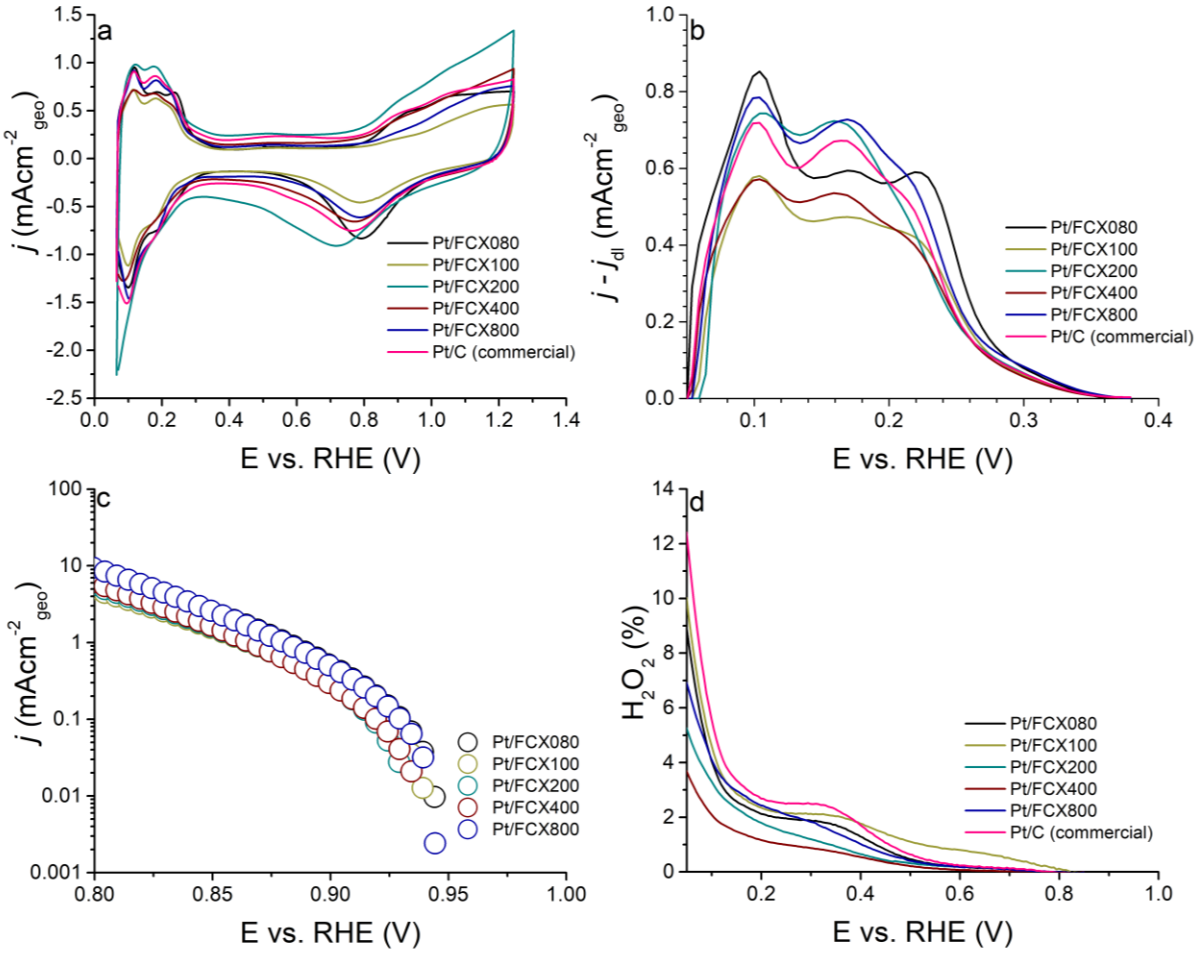

Figure 2.6. Electrochemical characterization of Pt/FCX080, FCX100, FCX200, FCX400 and FCX800, along with a commercial Pt/C electrocatalyst in N_2 (a, b) or O_2 (c, d) saturated 0.5 M H_2SO_4. Cyclic voltammetry in N_2 saturated 0.5 H_2SO_4 (a) and a zoom onto the H_{upd} region (b); Tafel slopes, corrected from the transport in solution, in O_2 saturated 0.5 M H_2SO_4 (see **Figure 2.1** for the non-corrected data) (c); peroxide production calculated from the ring current (d).

Figures 2.6c and **2.6d** present the reactivity of the electrocatalysts in O_2 saturated electrolyte. The specific activity at 0.90 V *vs*. RHE presented in **Table 2.3** was calculated from **Figure 2.6c**. From its values, it appears that: *(i)* the home-made electrocatalysts are presenting enhanced activities compared to the commercial one and *(ii)* that a slight increase in the specific activity at 0.90 V *vs.*

RHE is observed for high $S_{carbon}/S_{Pt,H}$ ratios, hence, inducing that the carbon support might be contributing to the ORR, either as a catalyst (thus, introducing a ORR mechanism occurring simultaneously on various active sites) or by modifying the Pt reactivity. The H_2O_2 production is significantly lower on Pt/FCX200 and Pt/FCX400, potentially inducing a contribution of the carbon with high in-plane crystallite size to the $2e^-$ mechanism resulting in the peroxide production (see **Table 2.1** for the carbon crystallite size).

Table 2.3. Specific surface of the carbon supports and electrochemical descriptor (S_{carbon}, $S_{Pt,H}$, $S_{carbon}/S_{Pt,H}$ and the specific activity at 0.90 V vs. RHE, $SA_{0.90}$) for the different electrocatalysts discussed in this work.

	S_{carbon} ($m^2\,g^{-1}$)	$S_{Pt,H}$ ($m^2\,g_{Pt}^{-1}$)	$S_{carbon}/S_{Pt,H}$	$SA_{0.90}$ ($\mu A\,cm_{Pt}^{-2}$)
Pt/FCX080	77	42	1.8	46.3 ± 16.5
Pt/FCX100	93	47	2	43.4 ± 9.6
Pt/FCX200	134	74	1.8	44.7 ± 4.1
Pt/FCX400	388	46	8.4	57.0 ± 16.4
Pt/FCX800	890	70	12.7	54.1 ± 7.6
Pt/C (40 wt. %)	254	81	3.1	26.2 ± 11.9

To further investigate the eventual impact of the carbon supports on the electrocatalysts reactivity, the kinetic isotope effect (KIE) was calculated, to assess an eventual change of the rate determining step. According to George *et al.*[155], the KIE for Pt electrocatalysts behave similarly in sulfuric and perchloric-based electrolyte. Thus, we decided to assess it in sulfuric-based electrolyte, to consider the presence of Pt-poisoning species when addressing the ORR mechanism and thus be in closer conditions to those observed in solid electrolyte, in presence of a Nafion® membrane, than when using a non-adsorbing electrolyte (such as 0.1 M $HClO_4$). The rate constants were calculated in 0.5M H_2SO_4 and 0.5M D_2SO_4 (in H_2O and D_2O, respectively) at the onset potential and the KIE was established as the ratio between the rate constant in H_2O and D_2O[167]. The values are reported in **Figure 2.7**, as a function of $S_{carbon}/S_{Pt,H}$. A low $S_{carbon}/S_{Pt,H}$ (*i.e.* a high density of NPs), that

shows KIE = 1, which corresponds to what was observed by George *et al.*[155] and others on Pt electrocatalysts for the ORR, which implies that the rate determining step is proton independent [44,98].

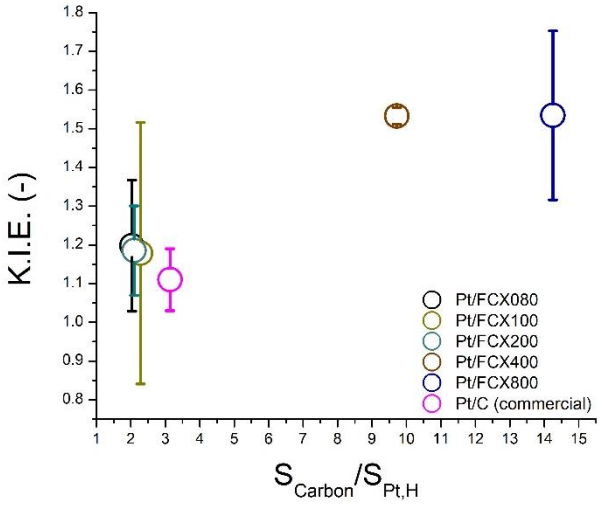

Figure 2.7. Evolution of the kinetic isotope effect as a function of $S_{carbon}/S_{Pt,H}$

This is consistent with the aforementioned statement about KIE values at high surface density of Pt NPs, considering that the specific surface area of Vulcan XC72R carbon is 254 m^2g^{-1}.[168] At high $S_{carbon}/S_{Pt,H}$ (i.e. for Pt/FCX400 and Pt/FCX800, that present a low density of NPs), that shows KIE = *ca.* 1.5, hence, providing evidence for a shift from a proton independent to a proton dependent mechanism with the increase of the $S_{carbon}/S_{Pt,H}$. As discussed in the introduction, 1.2 < KIE < 2 is indicative of a 'secondary KIE', which might not imply, by opposition to a 'primary KIE', the complete cleaving of the O-H/O-D bond, but only its partial cleaving, or the H/D atom displacement on the dioxygen molecule.[154] However, it is clear that, for Pt/FCX400 and Pt/FCX800, protons are now involved in the RDS and, thus, that decreasing the density of platinum nanoparticles (from S_{carbon}/S_{Pt} = 1 – 3 to S_{carbon}/S_{Pt} = 8 – 13) is indicative of an RDS change.

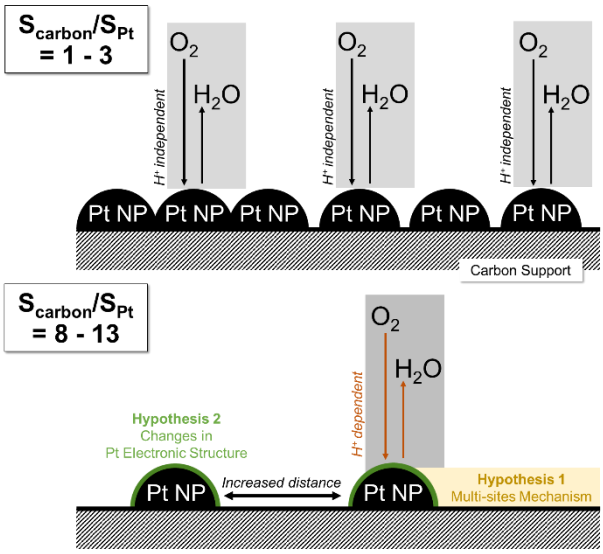

Figure 2.8. Illustration of the proton involvement in the rate determining step as a function of the platinum coverage on the carbon surface.

As illustrated in **Figure 2.8**, Two hypotheses are suggested to explain this phenomenon: (*i*) a parallel contribution to the ORR of the carbon support. Carbon blacks exhibit an extremely low reactivity for the ORR, mainly oriented toward a two-electron pathway. But, due to their vast exposed surface, they might have a minor contribution to the ORR and exhibit a proton-limited RDS with a large KIE (KIE > 2, *i.e.* full breaking of the O-D/O-H bond) leading to an overall increase of the KIE while the KIE on Pt remains identical (KIE_{Pt} = *ca.* 1); (*ii*) decrease of the Pt NPs – Pt NPs interactions, either through changes in the NPs proximity or decrease of the agglomerate content. Nesselberger *et al.* observed changes in the Pt NPs ORR reactivity, when the 'edge-to-edge' distance between the NPs is sufficiently small, and defined this phenomena as the particle proximity effect, stating that, in those conditions, the Pt NPs were behaving like bulk Pt (thus explaining the KIE = 1 observed at high Pt surface density).[169] It has also been observed that agglomerations, grain boundaries or, *lato sensu*, structural defects, strongly impact the Pt NPs

reactivity, thus implying that a decrease in said agglomeration, due to the increased interparticle distance, could result in changes in the ORR mechanism.[170]

To achieve a better understanding of the carbon support effect on the reactivity of the Pt nanoparticles for ORR, we characterized some of the electrocatalysts by near-ambient pressure X-ray photoelectron spectroscopy (NAP-XPS). NAP-XPS has been use, in the past decades, to assess the adsorption/reactivity of a wide range of molecules (CO, O_2, etc.) on various electrocatalysts (*e.g.* Ru, Au-based, *etc*.).[171–173] Here, high resolution Pt4f spectra were acquired for two of the electrocatalysts, *i.e.* Pt/FCX080 and Pt/FCX400 with similar loadings (14.8 wt. % for Pt/FCX080 and 15.2 wt. % for Pt/FCX400). The samples were investigated under ultra-high vacuum (UHV) and with exposure to oxygen (at 0.1 Torr). Variable energy X-ray source provides unique benefit of changing the signal sampling depth to be very surface sensitive. With a source energy of 280 eV, as used in **Figure 2.9**, the Pt 4f signal originates from 1.2 nm (see **Figure 2.10** for results obtained with a sampling depth of 2.5 nm), thus focusing on the phenomena occurring at the NPs/atmosphere interface. The investigation was performed in three steps (see **Figure 2.9a**, for Pt/FCX080 – the same data that is acquired from Pt/FCX400 is presented in **Figure 2.10**): *(i)* the acquisition of an XPS spectra at 80°C, under UHV, after a UHV cleaning at 150°C; *(ii)* the acquisition of an XPS spectra at 80°C, under gaseous atmosphere of 0.1 Torr O_2, after *(i)*; *(iii)* the acquisition of an XPS spectra at 80°C, under UHV, after step *(ii)*. The changes in spectra shape due to adsorption/desorption of gas on the surface of the electrocatalysts were evaluated by spectral subtraction. For spectral subtraction, a Shirley background-subtracted spectra was normalized by the total peak area to account for differences in photoelectron intensity due to attenuation in the gaseous atmosphere.

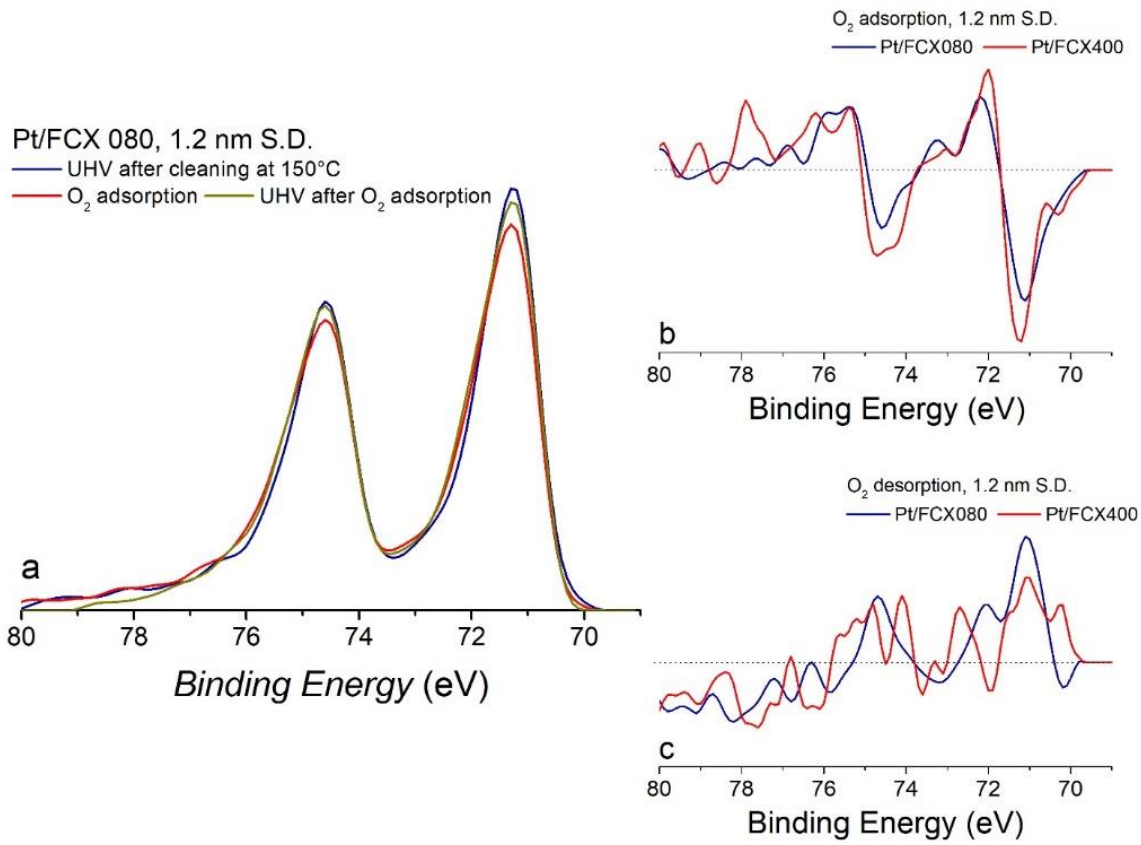

Figure 2.9 Near ambient pressure X-ray photoelectron spectroscopy spectra obtained for Pt/FCX080 under various conditions (i.e. ultra-high vacuum, UHV or 0.1 Torr O_2), with a sampling depth of 1.2 nm (a); signal difference between the 0.1 Torr O_2 environment and the UHV for Pt/FCX080 and Pt/FCX400 (b); signal difference between the UHV after O_2 adsorption and the 0.1 Torr O_2 environment for Pt/FCX080 and Pt/FCX400 (c);

The diminution of the peak intensity from UHV to gaseous atmosphere is the result of the oxygen adsorption on the Pt NPs, which induces a shift of the signal towards higher binding energies. Note that the shift in binding energy will result in an increase of the signal around the decrease in the peak intensity. The signal recovery from exposure to oxygen (step ii) to UHV condition (step iii) acts as a good indicator of how strongly oxygen was bound to the surface. Recovery of a spectral shape to the initially observed UHV pattern step (i) indicates weak reversible binding, whereas no or a small increase of the signal between step ii and step iii indicates a strong O_2 binding. **Figures 2.9b** and **2.9c** provide insights into the O_2 binding strengths on Pt/FCX080 and Pt/FCX400, by comparing the signals between UHV (steps (i)) and gas (step (ii)), and gas (steps (ii)) and UHV

(step (iii)). The O_2 adsorption observed in **Figure 2.9b** appears to have a smaller impact on the Pt/FCX080 Pt spectral shape than that of Pt/FCX400. According to **Figure 2.9c**, the surface 'recovery' from 0.1 Torr O_2 to UHV is higher on Pt/FCX080 compared to that of Pt/FCX400. These results imply that the binding of O_2 is weaker on the Pt NPs supported on FCX080. Such behavior indicates a non-negligible impact of the structure of the support on the electronic properties of the NPs, hence, on their reactivity for the ORR. This is in the frame of our obtained results using the KIE and might arise from the effect of the carbon support on the NPs distribution (*i.e.* the presence of agglomeration or the particle proximity effect[169]) which in turn impacts the reactivity of those NPs for the ORR.

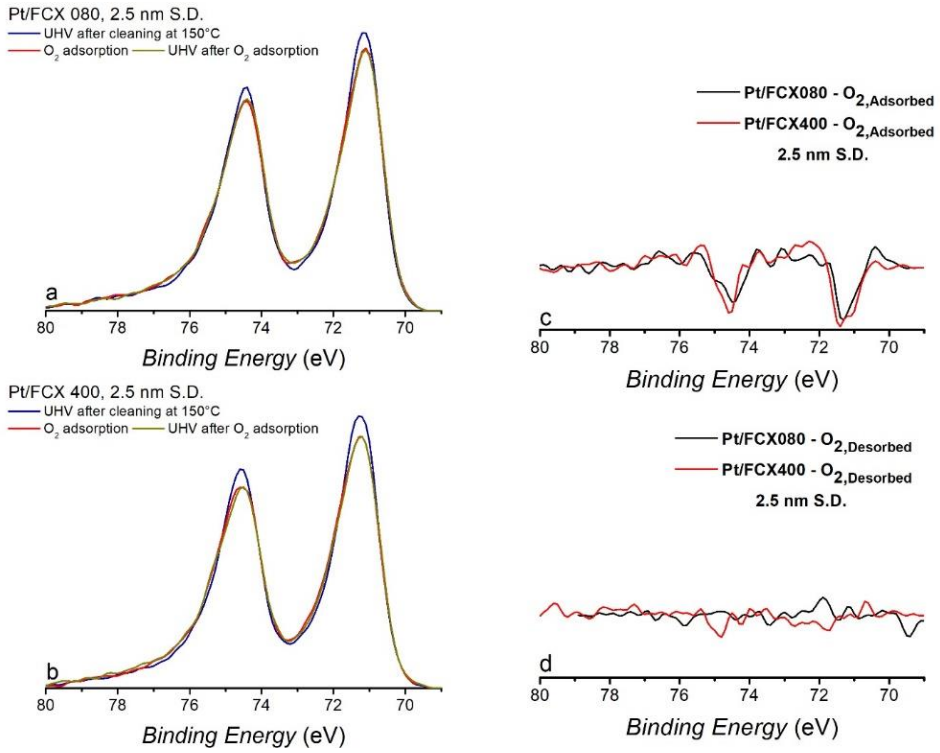

Figure 2.10 Pt 4f spectra obtained Near ambient pressure X-ray photoelectron spectroscopy for Pt/FCX080 and Pt/FCX400 under various conditions (i.e. ultra-high vacuum, UHV or 0.1 Torr O_2), originating from a sampling depth of 2.5 nm (a-b); signal difference between the 0.1 Torr O_2 environment and the UHV for Pt/FCX080 and Pt/FCX400 (c); signal difference between the UHV after O_2 adsorption and the 0.1 Torr O_2 environment for Pt/FCX080 and Pt/FCX400 (d). Evidently, part of the phenomenon that were reported in 1.2 nm sampling depth can be seen here is smaller in magnitude, *i.e.* diminution of the peak intensities as a result of oxygen adsorption on Pt NPs resulting in a shift in binding energies. However, the partial recovery of the Pt/FCX080 signal is not observed, because of the high sampling depth.

2.4 Conclusion

In this chapter, we discussed the role of Pt nanoparticles (NPs) density and of the carbon support on the reactivity of Pt/C electrocatalysts for the oxygen reduction reaction (ORR). The electrocatalysts were synthesized using the polyol method, resulting in NPs with a diameter of ~ 2 – 3 nm, independent of the carbon support. HAADF-STEM images and XPS evidenced a preferential deposition of the NPs on the edges of the carbon sheets and the carbon structural defects. Investigation of the ORR reactivity using the kinetic isotope effect (KIE) implied that there is no involvement of the proton in the rate determining step (RDS) when there is a high density of Pt NPs on the surface (*i.e.* KIE = *ca.* 1 for low surface area carbons). However, when the density of Pt NPs decreases, a KIE appears (KIE = *ca*. 1.5 for high surface area carbons), thus being indicative of a proton involvement in the RDS. This implies that the carbon supports affect the mechanism of the ORR either by: *(i)* acting as a secondary catalyst, thus, promoting a ORR occurring in parallel on the carbon and the Pt NPs or by *(ii)* modifying the dispersion of the Pt NPs, thus leading in changes in their agglomeration or in the particle proximity effect and, thus, in their reactivity. Hints toward the second hypothesis were provided by near ambient pressure XPS, as the Pt-O_2 bond seems to strengthen with the increase of the carbon support specific surface, thus illustrating modifications in the Pt electronic structure with the change in carbon support.

Acknowledgements

This work was supported in part by Toyota Research Institute of North America through National Fuel Cell Research Center. Carbonaceous materials /carbon blacks used in this work were provided

by Cabot Corp., Billerica, MA along with detailed materials analysis data set. The authors also acknowledge the DOE Office of Science User Facility under contract no. DE-AC02-05CH11231.

Chapter 3

The Effect of Pt Loading and Particle Proximity on the Oxygen Reduction Reaction on Pt-based Electrocatalysts

We investigated the effect of the loading of the platinum nanoparticles (Pt NPs) supported two carbon supports with different morphologies (93 vs. 890 $m^2 g^{-1}$) on the oxygen reduction reaction (ORR). We correlated their electrochemical performances with their physico-chemical properties. We extended our experiments from bench-scale lab tests to pilot-size membrane electrode assembly (MEA) fuel cell testing where we investigated the performance and durability of the in-house synthesized electrocatalyst. On the result basis, it was confirmed that low platinum loading on a high surface area carbon support resulted in a contribution of the latter to the ORR (see Chapter 2 for additional details). Moreover, it was observed that in the MEA systems, when using electrocatalyst with a large loading of Pt on the electrode – and thus a thin catalytic layer on the cathode side – at high current densities, flooding would partially block the Pt active site and thus limits the fuel cell performances.

3.1 Introduction

One of the most promising power sources for both stationery and mobile applications are polymer electrolyte fuel cells (PEFCs). This is due to this technology being, environmentally friendly, producing high power density with high efficiencies.[174–176] The most active electrochemical catalyst towards oxygen reduction reaction (ORR) is platinum (Pt)[177] which makes it the most commonly used electrocatalyst in such systems. Numerous researches have been conducted throughout the years on Pt due to high reaction overpotentials as a result of unfavorable kinetics

of this electrocatalyst towards ORR.[178,179] One of the ways to diminish these high overpotentials is to increase the loading of Pt NPs which leads to excessive surface density of the electrocatalyst.[180] It is known that catalyst loading (*i.e.* Pt NPs) plays a significant role in selectivity for water formation *i.e.* lower loadings show higher selectivity towards peroxide production (*i.e.* the reaction is a two-electron transfer reaction).[181] Furthermore, as evidenced in *chapter 2*, the distance between nanoparticles (which depend not only of the nature of the support, but also of its loading) impacts on the platinum reactivity & ORR mechanism.

In *chapter 3* of this document, we have selected a carbon support (*i.e.* FC100) which showed no kinetic isotope effect (KIE) towards the rate determining step (RDS) of the ORR (See *chapter 2*) and one carbon support (*i.e.* FCX800) that showed KIE effect (meaning that protons get involved in the RDS of the ORR) and synthesized electrocatalysts with 3.5 wt.%, 14 wt.% and 30 wt.% of Pt NPs on them. Moreover, for each one of the supports we made an attempt to saturate the surface of the support with the maximum possible Pt NPs. The result of this attempt was 42 wt.% and 68.8 wt.% of loading of Pt NPs for FCX100 and FCX800 respectively. By doing so, we aimed (i) to see how the performances (mass & Pt surface normalized) evolved as a function of the loading and the mechanism undertaken by the ORR on Pt and (ii) to study the implementation of the highest possible loading in MEA for fuel cell testing.

3.2 Materials and Methods

3.2.1 Preparation of Pt/C catalysts

As mentioned before, we selected two of the carbon supports from our previous work[182] and deposited different loadings of Pt NPs on them (*i.e.* 3.5 wt.%, 14 wt.%, 30 wt.% and an attempt to achieve a maximal loading of the two selected supports (*i.e.* FCX100 and FCX800) with Pt NPs) using microwave assisted polyol synthesis method. This method has been thoroughly elaborated in previous researches[157,183] and it is based on the zeta potentials of the precursors (*i.e.* carbon support and Pt NPs) as a function of their pH, being inversely signed and causing a uniform and relatively stable deposition of the nanoparticles on the support[158,159]. Succinctly, Platinum nanoparticles were synthesized using a modified polyol synthesis method based on those published by Rezaei *et al*[182]. An amount of Pt salt (H_2PtCl_6*xH_2O, 99.995% trace metals basis, Sigma Aldrich) was dissolved by ultrasonication and vigorous stirring in ethylene glycol. Then solution was brought to pH = 12 by the addition of NaOH (>97%, anhydrous pellets) dissolved in ultrapure water. The solution was then immediately transferred to the microwave heating vessels and heat to 160°C (CEM MARS 6 Microwave) under strong stirring. The resulting nanoparticle colloid solution is cooled to room temperature and brought to pH = 2. Then a calculated amount of carbon support is added to the solution and mixed for 24 hours. The catalyst is then vacuum filtered, washed, and dried in an oven at 60°C. In addition, a commercial Pt on graphitized carbon (20 wt. % Pt on Vulcan XC72R Carbon, Sigma Aldrich) was purchased and used for comparison.

3.2.2 Electrochemical characterizations

Electrochemical studies were performed using a BioLogic electrochemical analysis system in a three-electrode cell containing 0.1M $HClO_4$ electrolyte (Suprapur®, in H_2O, 18.2 MΩ) saturated at room temperature with either O_2 or N_2 depending on the test goals. A hydrogen reference electrode (RHE), a carbon-rod counter electrode and a glassy carbon rotating disk working electrode were used as the electrode components of a three-electrode electrochemical characterization setup. The electrochemical cell was stored in a equivalent volume mixture of H_2O_2 and H_2SO_4 mixture, thoroughly washed and boiled twice prior to the experiments. The ink that was deposited on the working electrode was prepared by mixing 4.94 mg of the Pt/FCX electrocatalyst with 1314.52 µL of deionized water, 657.26 µL of high purity Isopropyl alcohol and 23.71 µL of Nafion^{TM} ionomer (5 wt.% solution, DuPont). The ink was sonicated for 30 min. Then, 2×10 µL of the ink was deposited onto a glassy carbon disk with the electrode rotating at 250 – 400 rpm. First, an electrochemical impedance spectroscopy (EIS) measurement was performed to assess the ohmic losses in the cell, followed by the activation at 500 mV s^{-1} (between 0.05 and 1.23 V vs. RHE, 50 cycles) and a characterization at 20 mV s^{-1} (between 0.05 and 1.23 V vs. RHE, 3 cycles) in N_2-saturated electrolyte. Then, linear sweep voltammetries were acquired with rotation speeds between 400 to 2500 rpm with a scan rate of 5 mVs^{-1} (between 0.05 and 1.05 V vs. RHE) using a rotating ring-disk electrode (RRDE). The N_2-saturated electrolytes experiments in 0.1 M $HClO_4$ were used to calculate the electrocatalyst surface area with a desorption charge of 210 µC cm_{Pt}^{-2} H_{ads} per Pt.

3.2.3 Membrane electrode assembly (MEA) fuel cell testing

The selected electrocatalyst (*i.e.* 68.8 wt.% Pt/FCX800) was tested for performance and durability in a pilot-size Scribner 850e fuel cell test stand using DOE protocols[184] for activation and accelerated stress testing (AST). We prepared MEAs of 0.3 mg cm^{-2} loading from our electrocatalyst on the cathode and a loading of 0.1 mg cm^{-2} commercial HiSPEC Pt on the anode with an active surface area of 5 cm^2. Nafion XL was used as membrane due to its thickness of 27.5 µm and this thickness imposes the smallest possible resistance towards proton diffusion across the membrane. We used a 3X serpentine flow field on the bipolar plates and stoichiometric flow ratios of 1.2/2 for anode and cathode. The AST tests were performed in wet conditions (*i.e.* 100% relative humidity [RH]) and in two different environments that are H_2/Air and H_2/N_2, anode/cathode. The MEAs were tested for 30,000 square wave cycles with potential holds at 0.6 V and 0.95 V (OCV for H_2/Air case) for 3 seconds. The AST was stopped at cycles 1000, 5000 and 15000 for the purpose of characterization beside at the beginning and the end of life.

3.3 Results and Discussion

The effect of the Pt nanoparticles loading (and, therefore, of the particle proximity effect and the agglomeration) was investigated on two carbon black with widely different surfaces (93 $m^2 g^{-1}$ for FCX100, 890 $m^2 g^{-1}$ for FCX800, see **Table 3.1**). We deposited four different loadings of platinum nanoparticles (Pt NPs) on both FCX100 and FCX800 supports (*i.e.* 3.5 wt.%, 14 wt.% and 30 wt.% and a maximum practical loading, achieved by aiming to a theoretical loading of 80 wt.%, namely 68.8 wt.% for Pt/FCX800 and 42.2 wt.% for Pt/FCX100) using the polyol synthesis method. **Figure** shows the O_2-saturated linear sweep voltammetry and the N_2-saturated cyclic voltammetry of the different loadings of Pt NPs. The N_2-saturated plots (see **Figure a**) exhibit an Pt H_{UPD} altered

signal, induced by the high capacitance of the carbon support, for the samples with the highest carbon loading on the surface.

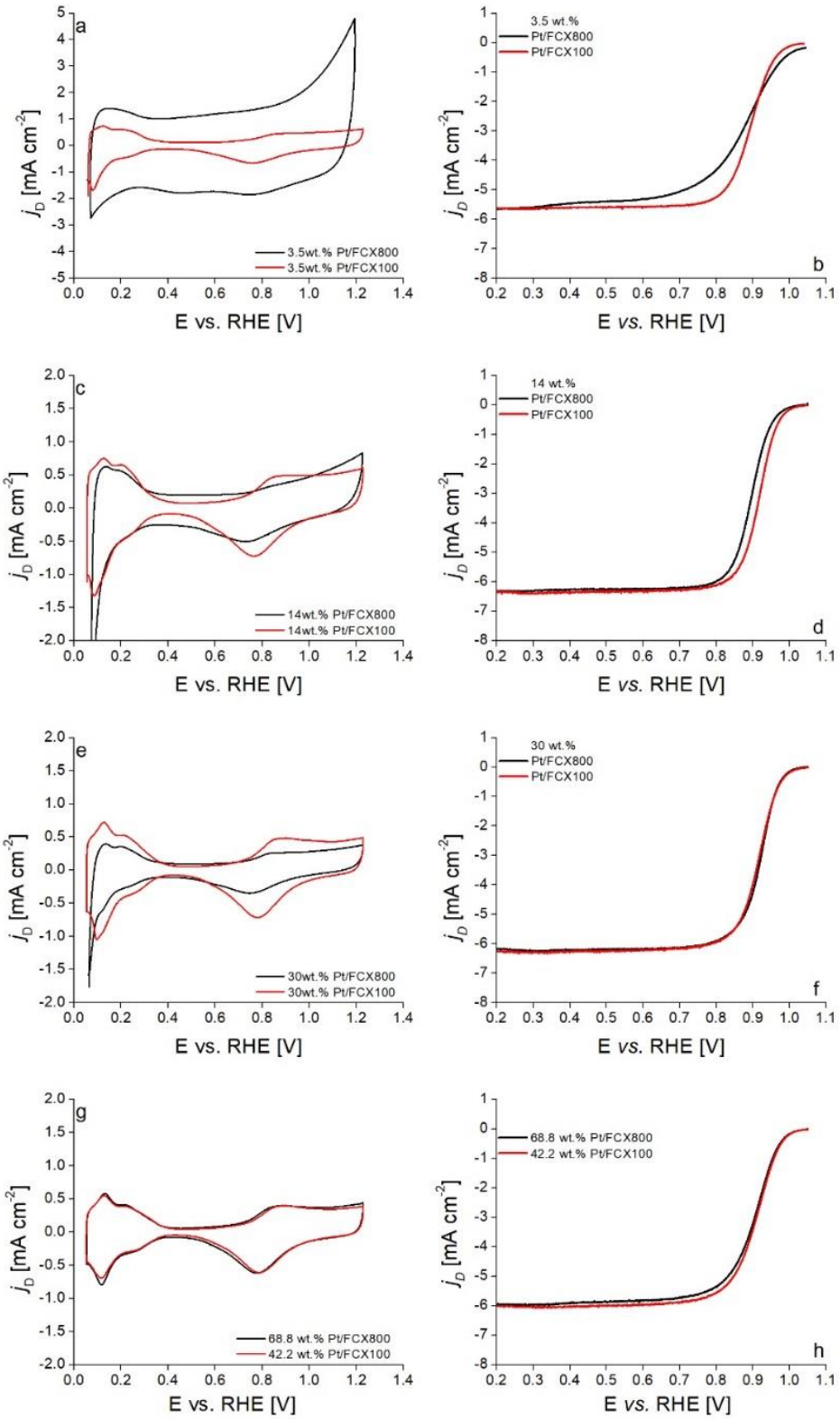

Figure 3.1 N_2-saturated cyclic voltammetry of the electrocatalysts for 3.5 wt.% (a), 14 wt.% (c), 30 wt.% (e) and max (42.2 wt.% for Pt/FCX100, 68.8 wt.% for Pt/FCX800, g) loading and linear sweep voltammetry in O_2 saturated electrolyte, at 1600 RPM, for 3.5 wt.% (b), 14 wt.% (d), 30 wt.% (f) and max (h). All experiments were performed in 0.1 M $HClO_4$, the N_2-saturated experiments at 20 mV s^{-1} scan rate & the O_2-saturated experiments at 5 mV s^{-1}.

This results of the constant loading in platinum of the electrodes during the liquid electrolyte characterization (40 µg cm^{-2}), which induced various loading of carbon being deposited in the electrodes. The high capacitance and the resulting thickness of the working electrode in turns impact the electrochemical signal in O_2-saturated electrolyte (see **Figure 3.1b**), by decreasing the performances in the 0.7 – 0.9 V vs. the reversible hydrogen electrode (RHE) region, potentially by the presence of an additional limitation to the diffusion in solution & and the intrinsic kinetics of the electrocatalysts, *i.e.* the O_2 diffusion inside the carbon porous network.

Table 3.1. Physical properties of the carbon supports discussed in this work.

Carbon Support	**L_c (nm)**	**L_a (nm)**	**Crystallinity (%)**	**S_{carbon} ($m^2\ g^{-1}$)**	**Micropores volume ($cm^3\ g^{-1}$)**	**Mesopores volume ($cm^3\ g^{-1}$)**	**Macropores volume ($cm^3\ g^{-1}$)**
FCX100	5	2.4	51	93	0.01	0.17	0.24
FCX800	-	3.6	38	890	0.20	1.03	0.95

All electrocatalysts maintain similar limiting current densities in diffusion limited potential region, indicating *(i)* a proper coverage of the working electrode surface *(ii)* a similar number of electrons transferred for both electrocatalysts in potentials between 0.1 V and 0.7 V *vs.* RHE. This indicates that the carbons support has little impact on the number of electrons exchanged in this potential region. However, in the low overpotential region, differences are observed, namely *(i)* superior catalytic activity at 0.95 V vs. RHE (see **Figure 3.2**) for the Pt/FCX800 vs. Pt/FCX100 at 3.5wt.% and *(ii)* superior catalytic activity at 0.95 V vs. RHE (see **Figure 3.2**) for the Pt/FCX100 vs. Pt/FCX800. For *(i)*, a possible explanation arises from a large contribution of the carbon support to the electrocatalyst reactivity. In a recent work, our group evidenced that, for low density of Pt NPs on a support surface, a kinetic isotope effect was observed, without depreciation of the electrocatalyst activity. This was assumed to arise to a modification of the Pt electronic structure

by the neighboring carbon and/or a multisite mechanism, with the carbon structural defects contributing to part of the electrochemical reduction process.

Table 3.2. Platinum specific surface ($S_{Pt,HUPD}$), mass activity at 0.90 V vs. RHE ($MA_{0.90}$) and 0.95 V vs. RHE ($MA_{0.95}$) and specific activity at 0.90 V vs. RHE and 0.95 V vs. RHE ($SA_{0.90}$) of the different electrocatalysts

Catalyst	Loading (wt.%)	$S_{Pt,HUPD}$ (m^2/g_{Pt})	$SA_{0.90}$ (μAcm_{Pt}^{-2})	$SA_{0.95}$ (μAcm_{Pt}^{-2})	$MA_{0.90}$ (A/g_{Pt})	$MA_{0.95}$ (A/g_{Pt})
Pt/FCX100	3.5	56.47 ± 2.72	187.6 ± 39.22	44.24 ± 5.78	107.29 ± 17.18	22.61 ± 3.56
	14	59.64 ± 3.08	392.15 ± 14.08	60.42 ± 9.73	257.59 ± 22.19	33.74 ± 7.86
	30	59.74 ± 3.54	341.42 ± 9.31	55.19 ± 4.42	203.44 ± 11.41	33.06 ± 4.56
	42.2	48.78 ± 2.92	287.33 ± 14.65	41.97 ± 1.82	139.27 ± 16.17	24.49 ± 5.96
Pt/FCX800	3.5	39.84 ± 5.89	199.42 ± 32.64	87.21 ± 6.84	89.41 ± 9.13	32.74 ± 2.12
	14	40.48 ± 4.39	240.00 ± 0.63	40.70 ± 7.50	121.97 ± 19.33	15.18 ± 3.65
	30	36.68 ± 8.80	493.33 ± 20.4	49.91 ± 0.46	285.09 ± 10.92	31.38 ± 2.13
	68.8	58.91 ± 4.04	331.7 ± 23.90	59.93 ± 2.29	165.25 ± 10.45	28.27 ± 5.82

The results presented in **Figure 3.1b** and **Figure 3.2** leans toward the carbon contribution to the ORR at low overpotentials, with a dramatically increased activity at 0.95 V vs. RHE for Pt/FCX800 *vs.* Pt/FCX100 when the loading is of 3.5 wt. % (i.e. for the catalyst with the maximal carbon to Pt surface ratio). The explanation could also not be mechanistic-based, but a result of the data treatment: the large capacitive current observed for the Pt/FCX800 3.5 wt.% could have led to imprecision in the baseline measurement and correction (see **Figure 3.3** for a non-baseline corrected measurement). All the activities calculated at both potentials (0.9 V *vs.* RHE and 0.95 V *vs.* RHE) show parallel behavior for both electrocatalysts however the values are in different scales.

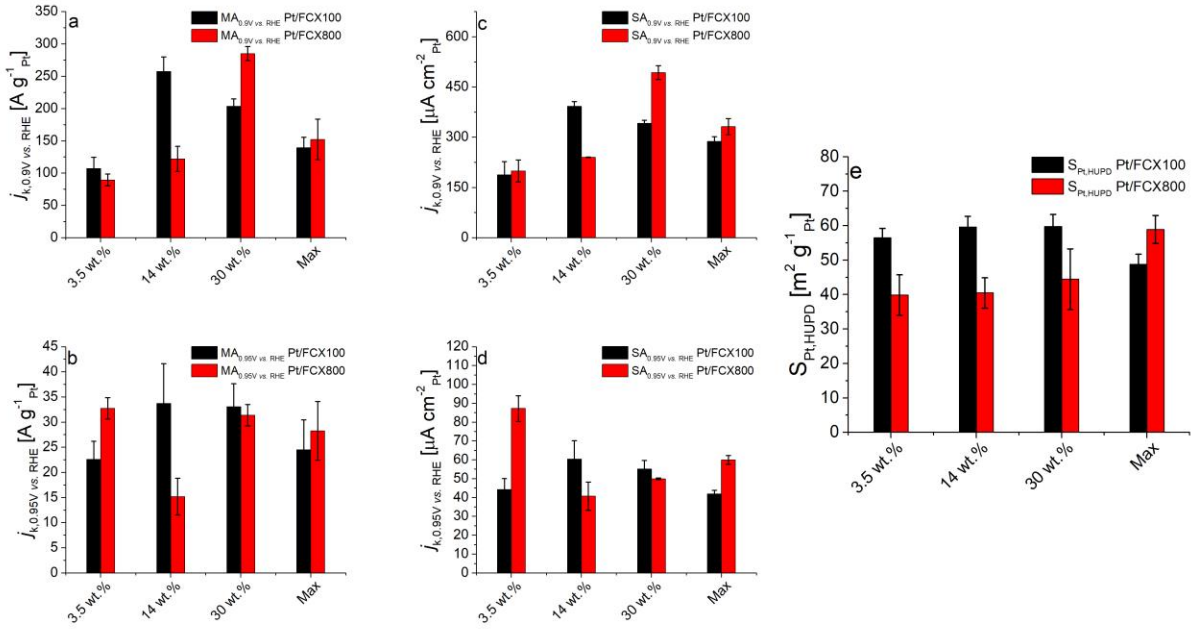

Figure 3.2mass (a,b) and specific (c,d) activity at 0.9 V *vs.* RHE and 0.95 V *vs.* RHE for the different catalysts studied in this work. The activities were corrected from the ohmic losses, the N_2-electrolyte baseline, and the transport in solution; specific surface (c) measured from the H_{UPD} for the different electrocatalysts studied in this work. The numeric values are provided in Table S1, along with the performances at 0.90 V *vs.* RHE.

The second notable discrepancy arises from the higher activity exhibited by the 14wt.% Pt/FCX100 *vs.* its FCX800 counterpart. This could be explained by the notable difference in average NPs size (see **Figure 3.5.** and **Table 3.2.**, *ca.* 2.4 nm *vs. ca.* 1.9 nm, the transmission electron micrographs being provided in **Figure 3.4.**), which result in a higher average coordination number for 14wt.% Pt/FCX100 and, thus, a closer-to-optimal oxygen intermediate binding.

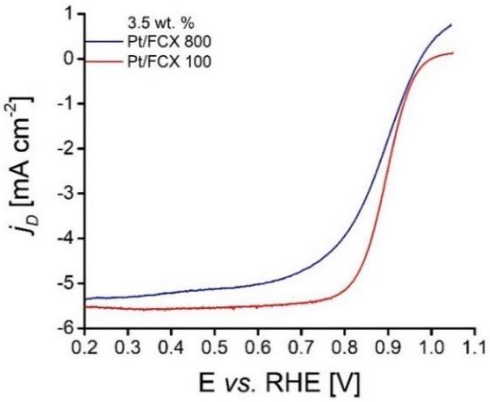

Figure 3.3. linear sweep voltammetry in O_2 saturated electrolyte, at 1600 RPM, for 3.5 wt. %, without baseline correction. All experiments were performed in O_2-saturated 0.1 M $HClO_4$, at 5 mV s^{-1}.

Such differences are no longer observed at higher loading (max and 30wt.%), indicating that an increased proximity between the Pt nanoparticles appears to decrease the relative effect of (i) the carbon contribution and (ii) the nanoparticles size. More specifically, the Pt/FCX800 exhibits, for 30 wt. % & max, a slightly higher specific activity.

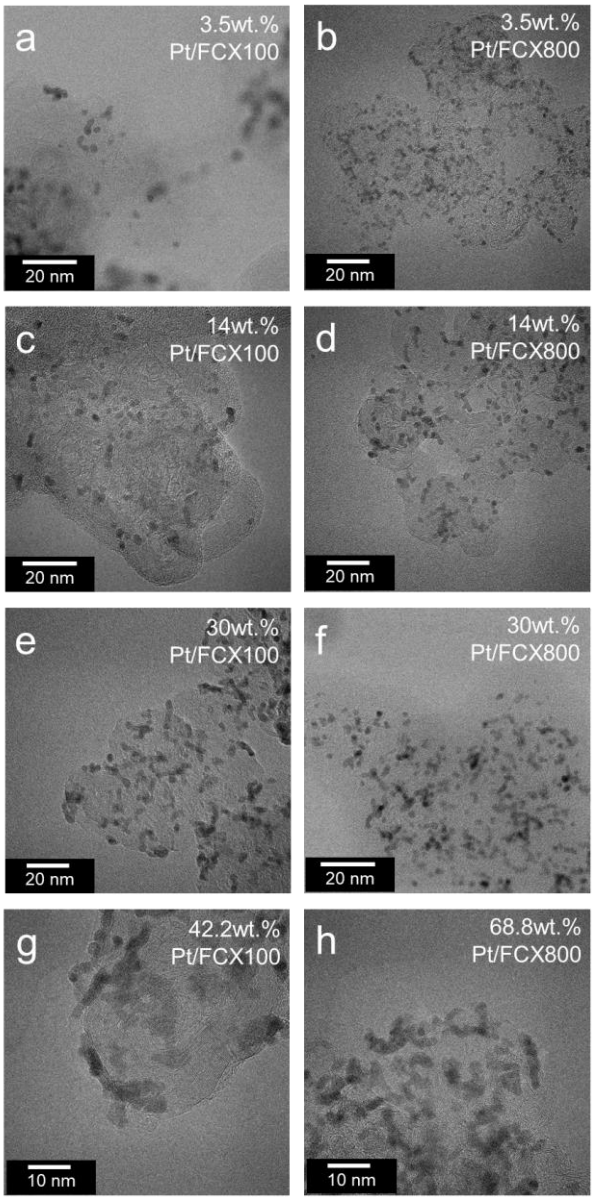

Figure 3.4. TEM images of Pt NPs deposited on the FCX carbon supports, *i.e.* 3.5wt.% Pt/FCX100 (a), 3.5wt.% Pt/FCX800 (b), 14wt.% Pt/FCX100 (c), 14wt.% Pt/FCX800 (d), 30 wt.% Pt/FCX100 (e), 30wt.% Pt/FCX800 (f), 42.2wt.% Pt/FCX100 (g) and 68.8wt.% Pt/FCX800.

As presented earlier, we attempted to achieve the maximum possible loading of Pt NPs on both carbon supports, which appeared to be 42.2 wt.% on PtFCX100 and 68.8 wt.% on PtFCX800. Those differences in loadings are directly related to their morphological and surface differences such as specific surface area (see **Table 3.1**), which significantly affects the number of anchoring sites available on the two supports. Assuming a similar density of anchoring sites on both supports, they are to be observed in much higher numbers of the FCX800, due to its superior specific surface. When addressing their electrochemical characteristics, they are similar, which indicates *(i)* a good coverage of the carbon supports' surface with deposited Pt NPs and *(ii)* very little (or none) contribution of the carbon supports to the ORR due to almost identical performances of the two electrocatalysts at low overpotentials.

Table 3.3. The particle size distribution of the different electrocatalysts studied in this work.

Catalyst	Loading (wt.%)	Particle Size Distribution (nm)
Pt/FCX100	3.5	1.99 ± 0.58
	14	2.42 ± 0.60
	30	2.48 ± 0.56
	42.2	3.08 ± 0.83
Pt/FCX800	3.5	1.77 ± 0.43
	14	1.93 ± 0.63
	30	1.81 ± 0.33
	68.8	2.45 ± 0.59

Due to the high surface density of the Pt NPs, the N_2-saturated voltammograms show clear H_{UPD} peaks with minimal capacitive current and a clear plateau in the Pt oxidation region. An increase in the average diameter (*ca.* 3 nm) of the NPs was observed on the Pt/FCX100 42.2 wt.%, likely induced by the NPs agglomeration, as a result of the lower specific surface of the FCX100 vs. the FCX800. Although the latter also exhibited an increase in NPs diameter, the latter remained smaller, i.e. ca. 2.5 nm (see **Table 3.2.** and **Figure 3.5.**). **Figure 3.4.g-h** shows the TEM micrographs of these two electrocatalysts, agglomeration being a clear phenomenon.

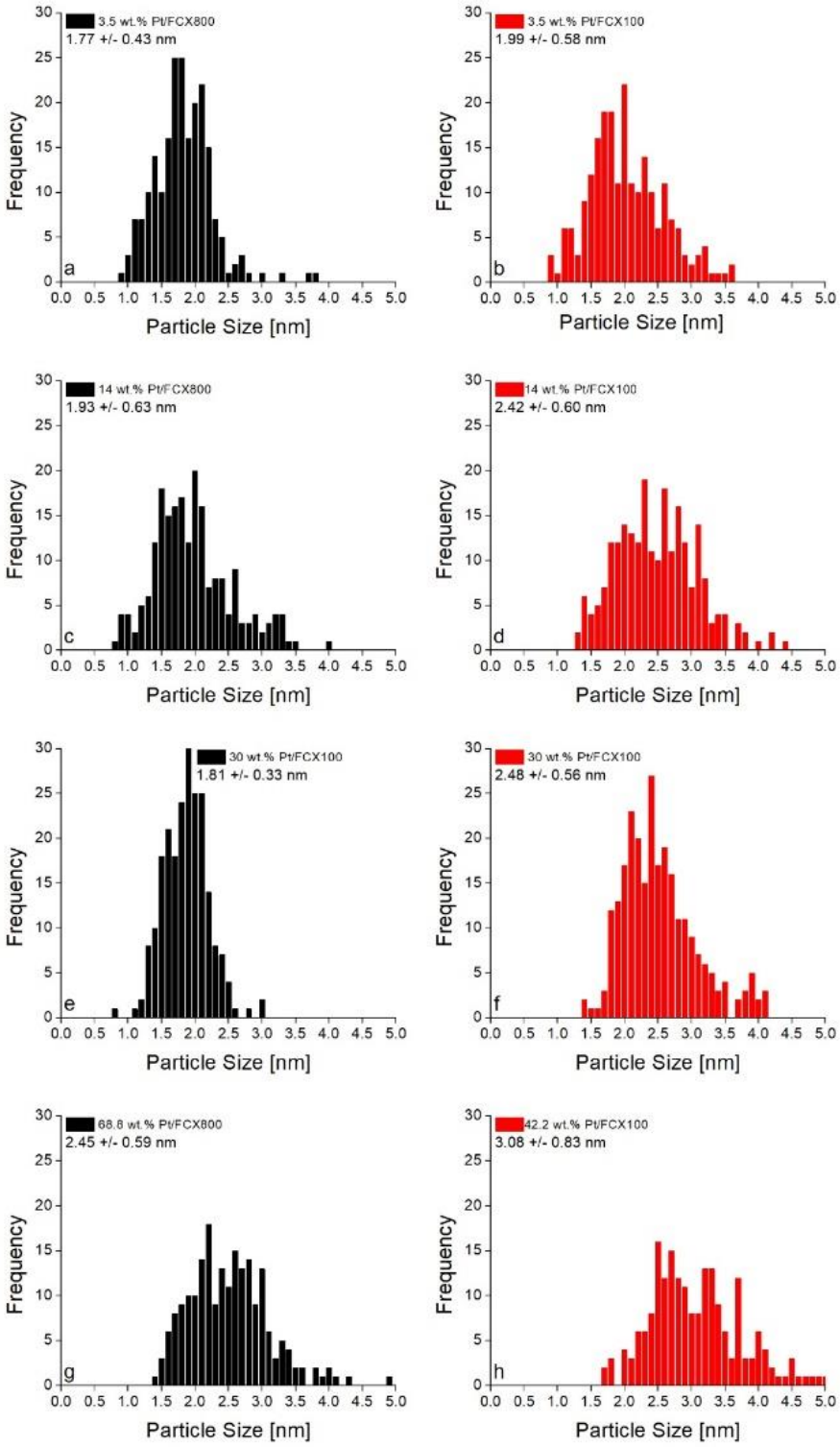

Figure 3.5. Particle size distribution for the different electrocatalysts studied in this work (the numeric values are also provided in **Table 3.2**).

To further investigate the catalytic activity and durability of maximum loaded Pt/FCX800 (*i.e.* 68.8 wt.% Pt/FCX800) we have tested the mentioned electrocatalyst in a polymer electrolyte membrane fuel cell (PEMFC) setting.

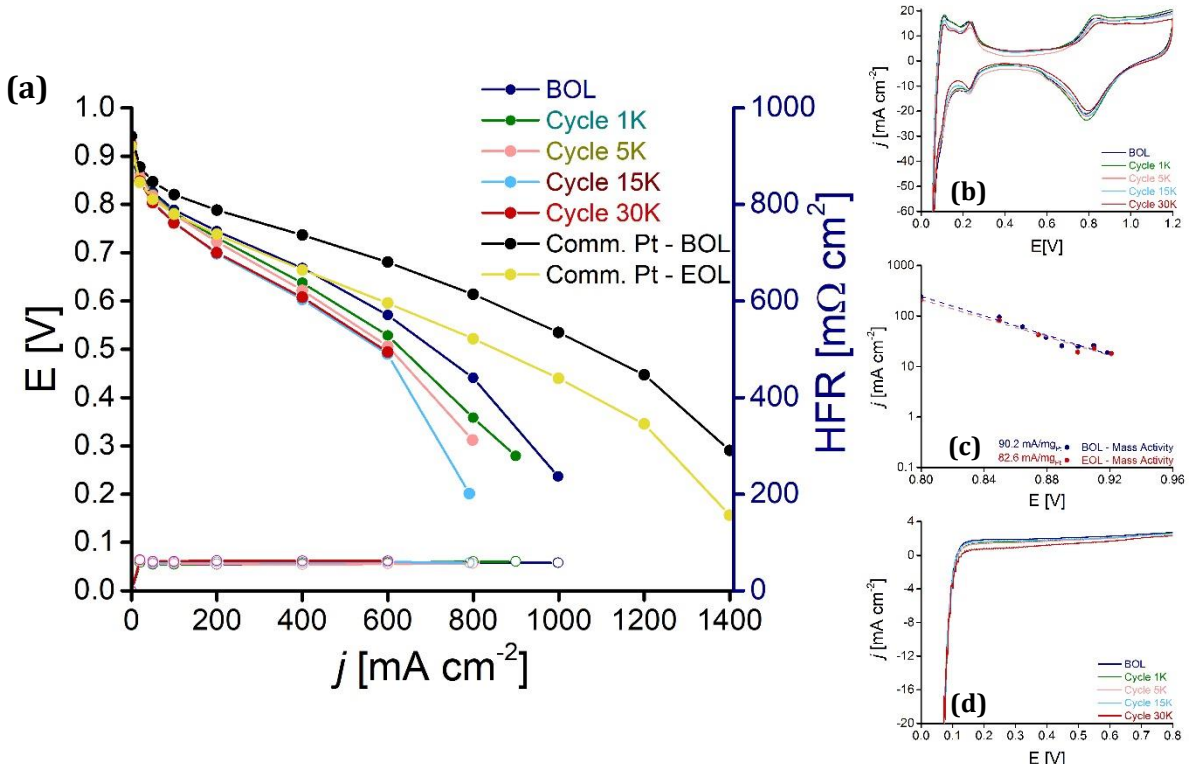

Figure 3.6 *Performance of the MEA (a) Electrochemical characterization (b) Mass Activity (c) H_2 crossover of the MEA under H_2/Air (d)*

We used decal method to load this catalyst on the cathode side with a loading of 0.3 mg cm^{-2} and the anode side was consisted of commercial Pt/C with the loading of 0.1 mg cm^{-2}. Fuel cell testing included durability tests under different environments (*i.e.* H_2/N_2 and H_2/Air at cathode/anode) and electrochemical characterizations were performed in between, to show the gradual degradation of the membrane electrode assembly (MEA). We conformed to DOE's protocol for accelerated stress testing (AST) where we continued the cycling of the MEA for 30,000 square wave cycles (equal to 50 hours) at potentials of 0.6 V and 0.95 V for 3 s at each of the potentials.

Electrochemical characterizations were then performed at the beginning of life (BOL), cycle 1000, 5000, 15000 and the end of life (EOL) or 30,000 cycles.

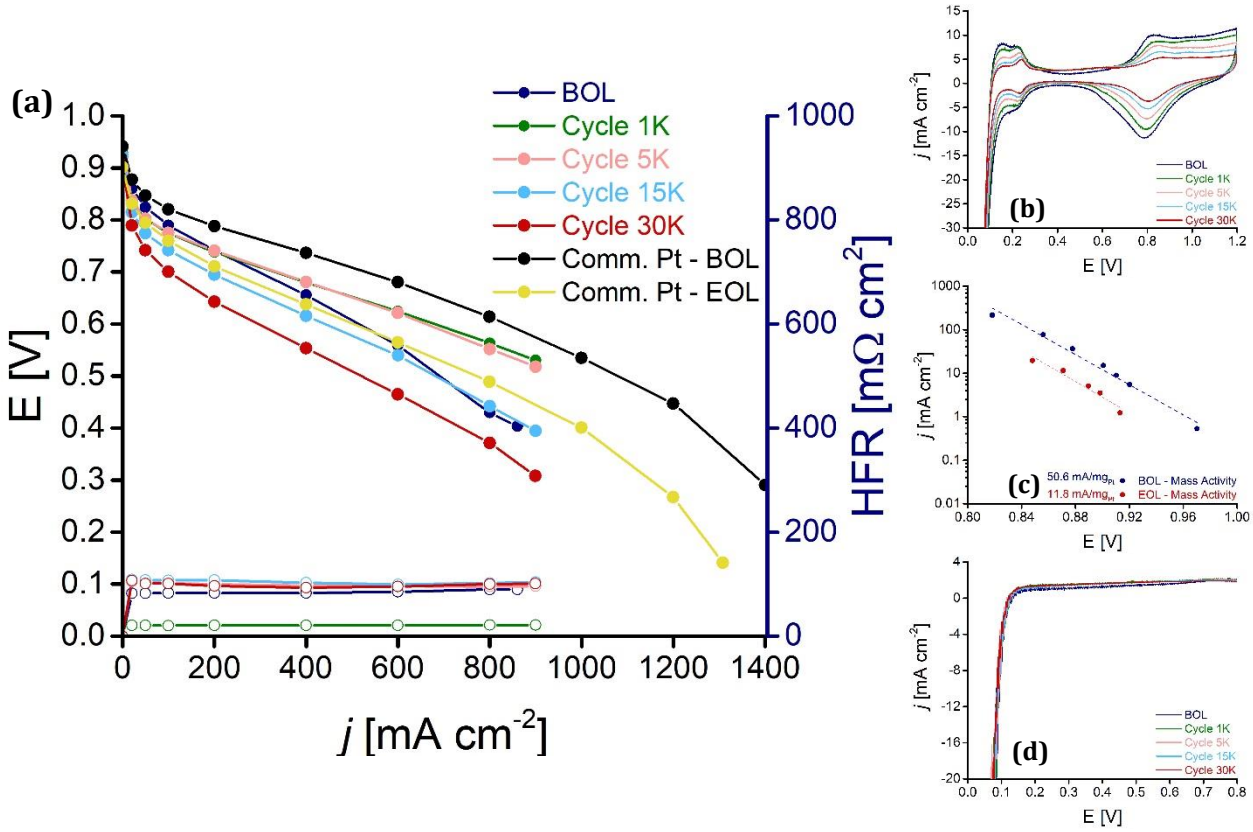

Figure 3.7 *Performance of the MEA (a) Electrochemical characterization (b) Mass Activity (c) H_2 crossover (d) of the MEA under H_2/N_2*

Figure 3.6.b shows cyclic voltammograms of the MEA in H_2/Air environment at each given cycle of the AST where there is a clear degradation with the pass of cycling at every Pt characteristic peak. **Figure 3.6.d** shows the H_2 crossover current that remains low which is a confirmation of no pinholes or other significant convections of the gas across the membrane in the MEA. The gradual decay of the MEA is seen in **Figure 3.6.a** where the polarization curves where there is a decrease in the current density of the MEA at any given potential with the pass of cycling. However, the drop of performance becomes more pronounced in the transport region of the polarization curve which could be a sign of fuel starvation. The polarization curves also, become more ohmic with

the pass of AST cycling. **Figure 3.7** shows the performance polarization curves, cyclic voltammogram, mass activity and H_2 crossover current of the MEA, aged in H_2/N_2 environment. As it can be seen from the performance polarization curves, the degradation of the MEA after 30,000 cycles (50 hrs) of cycling was more severe in H_2/N_2 environment as it can be seen that the performance has dropped more severely in that case.

With the loss of the ECSA the change of activation overpotential of ORR can be calculated by taking the ratio of two Tafel equations for BOL and that during ageing and rearranging to obtain the following equation:

$$\Delta\eta = \frac{2.303RT}{\alpha F}\log\left(\frac{i_0 \cdot ECSA_{BOL}}{i_0 \cdot ECSA_{Aging}}\right) \quad (3.1)$$

where $\Delta\eta$ is the change in ORR overpotential from BOL during ageing, i_0 is exchange current density that is assumed to be constant,[185] R is gas constant, T is temperature, F is Faraday's constant and α is the symmetry coefficient that is taken to be 1 at low current densities. The only changing factor during ageing is the ECSA. When $\Delta\eta$ is plotted against log($ECSA_{ratio}$), a Tafel slope can be calculated (see **Table3.4**) and compared to the expected 70 mV/dec if all the overpotential losses during ageing are due to ECSA loss.

Table 3.4 *Tafel slopes at 50 and 100 mA/cm^2 current densities*

Condition	**Tafel slope at 50 mA/cm^2 [mV/Dec]**	**Tafel slope at 100 mA/cm^2 [mV/Dec]**
H_2/Air	89.5	108.5
H_2/N_2	55.9	61.1

Using **Eq. 3.1** we calculate Tafel slopes at low current densities, which are 50 and 100 mA/cm^2 and show them in **Table 3,4**. At 50 mA/cm^2 we observed Tafel slopes of 89 and 56 mV/decade

for H_2/Air and H_2/N_2, respectively. Thus, these values show close to expected 70 mV/dec loss of overpotential, which is indicative that the polarization loss for these two cases is mainly due to the ECSA loss. However, for confirmation, we performed these calculations at 100 mA/cm^2 and the Tafel slope values were confirmed in case of H_2/N_2 environment but showed a slight increase to 108 mV/Dec for H_2/Air environment. This indicates that the polarization loss in H_2/Air environment can be due to other factors besides ECSA loss such as ohmic, mass transport and kinetic losses.

3.4 Conclusion and Outlook

In this chapter, we have prepared and tested different weight loadings of Pt NPs supported on two carbon supports with a wide difference in specific surface area (FCX100 and FCX800 with specific surface areas of 97 and 890 m^2/g, respectively). Particle size distribution showed more agglomeration on the support with lower surface area (*i.e.* FCX100) where it showed no significant agglomerations in FCX800 until for the saturated surface where there was a slight increase in the average particle size distribution. The 80 wt.% Pt/FCX800 was then integrated in a fuel cell system for further testing and it was shown that degradation of the MEA under H_2/N_2 environment is more severe that confirms our previous works in fuel cells. To deduce that conclusion, we performed 30,000 square wave cycles of accelerated stress testing (AST) with 3 s potential holds at 0.6 and 0.95 V and one of the reasons for higher degradation for H_2/N_2 case was shown to be the OCV drop of the MEA during the AST test. This causes the upper potential limit of the AST for H_2/Air case to drop and as in is know from previous researchers' work, potential holds at lower UPL values cause less degradation to the Pt NPs. However, to find the source of performance loss we plotted the natural log of ECSA loss versus potential difference at different stages of the AST at

low current densities and it turns out that for H_2/Air case. From Tafel slopes of this plot at 100 mA/cm^2, it is possible that the performance loss is not solely due to ECSA loss as ohmic, kinetic or transport losses are not negligible. This is not the case in H_2/N_2 case and Tafel slopes show no involvement of other factors rather than the ECSA loss.

To summarize, high surface area carbon supports promote the possibility of higher accessibility of deposited platinum nanoparticles mainly due to their morphology that is consisted of a higher volume of mesopores which increases the chance of a deposition turning into an active site. This quality makes electrocatalysts deposited on such support better candidates for high performance electrocatalysts compared to nanoparticles deposited on more graphitic carbon supports. As a result, high surface area carbon supports as supporting material for deposition of Pt NPs for heavy duty automotive fuel cell applications is plausible.

Chapter 4

Probing Heterogenous Degradation of Catalyst in PEM Fuel Cells Under Realistic Automotive Conditions with Multimodal Techniques

4.1 Introduction

Polymer electrolyte fuel cell (PEFCs) technology has advanced to reach commercialization stage with more automotive manufactures announcing new PEFC-based light and heavy-duty vehicles.[186] However, life span and cost of such systems still remains a challenge.[37,187] Using the Department of Energy (DOE) cost-breakdown for the 80-kW_{net} stack for light-duty vehicles, the cost of precious metal electrocatalysts remains almost unchanged as production rate increases to 0.5 M PEFC stacks per year.[188] The cost of the electrocatalysts amounts to 31 % of stack cost, for 0.5 M systems per year production rate.[188] Platinum (Pt) or Pt-alloys are used as electrocatalysts for the oxygen reduction reaction (ORR) on the cathode side and the hydrogen oxidation reaction (HOR) on the anode side of PEFCs. Pt or Pt-alloy electrocatalysts are dispersed as nanoparticles (NPs) onto a carbon-black support. DOE set a target of reducing Pt loading to 0.125 mg/cm^2 to achieve the goal of \$12.6/kW_{net} for stack with a power density target of 1.8 W/cm^2. MEAs with lower catalyst loading are less durable[186], thus, the cost issue cannot be resolved without focusing on the catalyst durability issue of the PEFC stack.

More generally, catalyst degradation occurring during PEFC operation impacts the performance by decreasing the power density of the stack and by increasing fuel consumption per generated kWh.[84,189] PEFC catalyst durability has been previously studied extensively.[87,128,190–192] Platinum electrocatalysts are more prone to degradation on the cathode side of the PEFCs, rather than anode due to higher potentials and more oxidizing conditions.[193,194] Previously, Wang *et al.*[195] reported

electrochemically active surface area (ECSA) loss of 54.5 % and 30.2 % for cathode and anode, respectively. They reported higher degradation rates (more ECSA loss) on the cathode side which is due to several factors including *(i)* wider range of potential, *(ii)* higher difference in pH values and *(iii)* higher water content.

In automotive applications load changing, startup-shutdown, idling and higher power density operation contribute 56.5 %, 33 %, 4.7 % and 5.8 %, respectively to overall performance degradation.[196] The dynamic load changing is the largest contributor to degradation for various reasons: i) it induces humidity and thermal cycling, ii) it may cause gas starvation and ii) potential cycling due to dynamic load degrades Pt electrocatalyst. The basic metrics for the degradation evaluation are polarization and ECSA loss. Pt degradation and ECSA loss is mainly due to three mechanisms: Pt dissolution/precipitation, Ostwald ripening, Pt agglomeration.[197] Pt dissolution occurs at high potentials at both anodic and cathodic sweeps of potential cycling[26,27] and it is a function of particle size and oxide coverage.[28] According to Gibbs-Thomson equation, smaller particles are more susceptible to dissolution (due to the inverse dependency of surface energy with particle size) and Pt ions are more likely to redeposit onto larger particles to induce Ostwald ripening.[198] For this to happen, both particles have to be electrically connected (carbon support) and ionically connected for Pt^{2+} ions to transport. Ostwald ripening is slower for uniform particle sizes. Water content in ionomer dictates ionic conductivity in ionomer and high-water content intensifies electrochemical Ostwald ripening.

To assess a PEFC durability, accelerated stress tests (ASTs) are used because of their shorter time of experiments compared to using real drive-cycle of vehicle, that typically (according to DOE durability targets[52]) needs to last from 6,000 to 40,000 hours for automotive and stationary applications, respectively. ASTs generally include potential cycling between two potentials to

simulate load change and accelerate degradation of the catalyst layer.[30,31,199] Degradation includes morphological changes in the CL that cause damages, such as crack formation, thickness losses, ECSA losses and diffusive, ionic and electric pathway connectivity loss leading to transport losses.[32,200] Degradation of PEFC has been both physically modeled[201] and experimentally investigated.[202] The influence of voltage cycle profiles on degradation of MEAs has been comprehensively reported by Stariha *et al.*[23] They used square wave and triangular wave potential cycling and evaluated degradations of both the catalyst and the support in different potential ranges. ASTs with square wave voltage cycling showed the highest rate of catalyst degradation. This is due to the fact that degradation rates, and ECSA loss increase with the increase of dwell time at the upper potential limit (UPL).[203] The reason for the UPL dwell time in H_2/Air environment affecting the catalyst durability, is due to larger amount of Pt oxide coverage, which will result in higher Pt dissolution rates. [204–206]

Repeated oxidation and reduction of Pt nanoparticle surface leads to dissolution of Pt which, is a principal catalyst degradation mechanism.[198] This dissolution of Pt leads to two different ECSA loss pathways. In the first pathway, Pt ions redeposit on nearby larger Pt nanoparticles due to electrochemical Ostwald ripening, thereby increasing the Pt nanoparticle size.[207] Second, Pt ions diffuse through the ionomer phase towards the membrane and are reduced in the membrane by the crossover hydrogen.[207,208] **Figure 4.** shows the schematic of AST potential cycle with the possible Pt degradation reaction mechanisms considered in this study. During the anodic scan (from low to high potential), pristine Pt surface is present at lower potential limit (LPL). Dissolution of Pt through defect sites at very low rate happens during the sweep from LPL to upper potential limit (UPL)[209]. As potential crosses 0.8 V, OH groups are adsorbed on the Pt surface ultimately leading to the formation of PtO as the potential reaches UPL.[210] During the hold time at UPL, increase in

the PtO coverage and place-exchange is seen with simultaneous Pt dissolution at low rate.[209,211] As the potential sweeps to LPL, in the cathodic scan PtO is reduced (~0.8 V) to PtOH. In an alternative reaction pathway PtO reacts with protons to form dissolved Pt and water. If the LPL is in low re-deposition potential range, then unavailability of pristine Pt surface for the Pt ions to redeposit on causes Pt band formation in the membrane. If the LPL is in high re-deposition range, then availability of pristine Pt surface for Pt ions to redeposit on makes Ostwald ripening as the principal ECSA loss mechanism. Then more PtO formation is followed in the next AST cycle due to availability of pristine Pt surface. [31,212] At lower UPLs, PtO coverage is lower, leading to lower Pt ions formation consequently causing less degradation over the AST duration.[205]

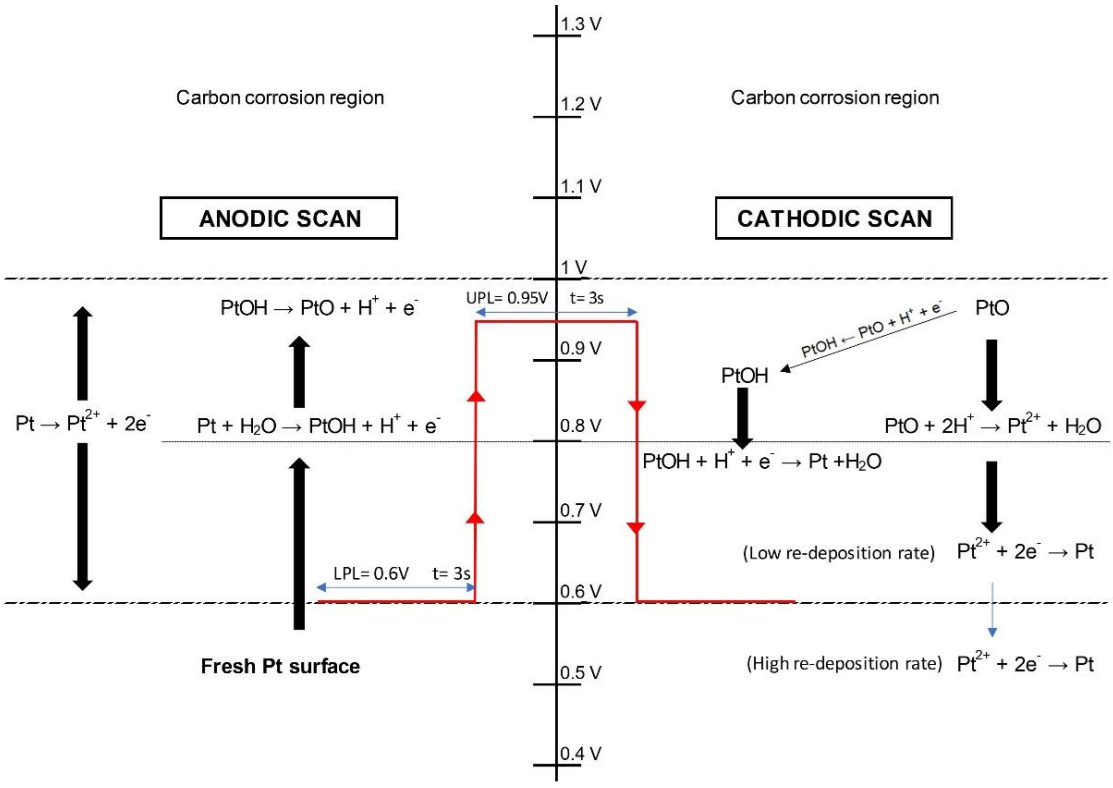

Figure 4.1 *A schematic of AST potential profile used in this study and associated Pt degradation reaction mechanisms.*

The degradation of the PEFC materials is a heterogenous process due to land-channel geometry of the flow-field, and non-uniform distribution of the reactant gases in the catalyst layer under land

and channel, as well as, inlet and outlet.[213] The inhomogeneity in reactant distribution also creates non-uniform temperature distribution, where heat due to ORR is the largest contributor to the overall heat generation at high current density.[214] Local hot spots in catalyst layer lead to membrane and catalyst layer degradation.[189] Heterogeneity of distribution of fuel in the CL cause hydrogen starvation in some regions of the cell resulting in higher degradation rates.[215] General characterization tools for CL degradation include in-situ and post-mortem techniques. In-situ, during cell operation, the CL degradation can be analyzed with electrochemical techniques, such as ECSA measurements,[216,217] hydrogen crossover determination through linear sweep voltammetry[218] and polarization resistance characterization through electrochemical impedance spectrometry (EIS).[219,220] Imaging post-mortem techniques include SEM and TEM for morphology investigation and particle size and elemental distribution analysis of a cross-section of a MEA.[221222,223] In addition, 3D imaging techniques, such as X-ray computer tomography (X-ray CT) have been used to provide information about heterogenous degradation, adding time as a fourth dimension. [224]

Our earlier study showed first time use of synchrotron micro-XRD technique to map Pt size distribution post-mortem for MEA aged in H_2/Air humidified conditions using square-wave AST protocols under land-channel geometry[225]. We build upon the earlier study to investigate catalyst degradation rates under H_2/N_2 and H_2/Air environments in dry and wet conditions. We further investigate the effect of land and channel using the US DRIVE FCTT adopted AST protocols. A combination of electrochemical characterization and post-mortem characterization techniques (SEM/EDS, micro XRD, X-ray CT, X-ray fluorescence (XRF), X-ray photoelectron spectroscopy (XPS)) is used to unravel the mechanisms behind Pt degradation at inlet/outlet and land/channel locations under various gas and humidity conditions. In order to represent automotive conditions

in the experiments, the UPL did not exceed the open circuit voltage which also limited carbon corrosion during the AST.

4.2 Materials and Methods

Pt/C based MEAs were purchased from Ion Power Inc., New Castle, Delaware, with an active area of 25 cm^2 and loading of 0.3 $mg_{Pt}cm^{-2}$ and ionomer to carbon (I/C) ratio of 1 on both anode and cathode. These MEAs contained Nafion XL reinforced membrane of thickness 27.5 µm. A non-woven carbon paper, Sigracet 29 BC, with 5 wt % PTFE treatment and hydrophobic microporous layer (MPL) was used as gas diffusion layer (GDL). The total thickness of the GDL is reported by manufacturer as 235 µm.

4.2.1 Testing Equipment

Fuel cell fixture hardware from Scribner Associates with POCO graphite 3X serpentine flow field (0.92 mm/0.79 mm width lands/channels) was used. Hard-stop PTFE-coated fiberglass gaskets (150 µm thickness) and PTFE gaskets (27.5 µm thickness) were used to achieve GDL compression of 22 %. 13.5 Nm torque was used during the cell assembly. Accelerated stress tests (AST), polarization curves and mass activity measurements were all performed using the 850e Fuel Cell Test Stand (Scribner Associates, Connecticut, USA) with maximum current load of 100 A. Cyclic voltammograms (CV), linear sweep voltammograms (LSV) and electrochemical impedance spectroscopy (EIS) were measured using VSP-BioLogic potentiostat (potential resolution of 5 µV and maximum current of 4 A)

4.2.2 Accelerated Stress Testing Protocols (AST)

Four square wave ASTs were conducted. The conditions for ASTs were either H_2/N_2 or H_2/Air on anode/cathode both in 40 % and 100 % RH. The ASTs were conducted with potential cycling from 0.6 V to 0.95 V in N_2 on cathode, or 0.6 V to 0.95 V or OCV, if OCV < 0.95 V for air gas on cathode with a dwell time of 3 s at each potential for 30,000 cycles, resulting in a total test time of 50 hours. A schematic of AST single cycle for AST in N_2 and air is shown by **Schematic 4.1 a-b**. The AST was performed at atmospheric pressure and in H_2/air (anode/cathode) and H_2/N_2 environments at 100 % and 40 % relative humidity (RH) with gas flowrates of 210 sccm/830 sccm (anode/cathode) for H_2/Air and 200 sccm/200 sccm for H_2/N_2. For the AST performed in air the OCV decreased with cycle number and for this reason the UPL was reduced. The OCV was partially recovered during voltage recovery protocol. Flowrates were calculated for stoichiometric ratio of 1.2/2 (anode/cathode) assuming maximum current density of $1A/cm^2$ at 0.6 V. During the AST, each MEA was characterized at stages of 0, 1000, 5000, 15000 and 30,000 cycles. Error! R eference source not found.**b** lists the summary of all the ASTs and characterization experiments. **Table 4.1** shows the four ageing tests selected in this study and also the naming convention for this work.

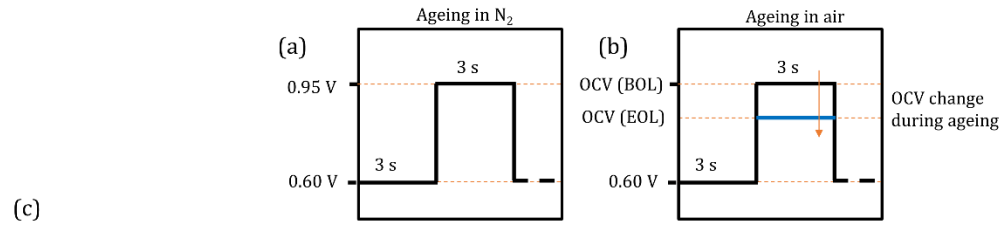

(c)

	T_{cell} (°C)	H_2 -	Air -	N_2 -	O_2 -	RH %	DP (°C)	Pressure (a) Kpa (a)	Flow A slpm	Flow C slpm	
Conditioning	80	A	C			100	80	100	0.8	1.5	Square wave, 0.8V, 0.6V, 0.3V, 30s each
Characterization											
Voltage Recovery	40	A	C			150	59	150	0.45	0.25	Constant voltage 0.1V, 2h
Polarization Curve	80	A	C			100	80	150	ST 1.5	ST 1.8	
Mass Activity	80	A			C	105	81	150	1.5	2	
CV **H_2 Crossover LSV** **EIS**	80 80 80	A A A		C C C		100 100 100	80 80 80	100 100 100	0.25 0.25 0.25	0.25 0.25 0.25	20 mV/s 1 mV/s 0.2V, 20,000-0.1 Hz, 0.01V AC
AST Cycle	80	A		C		100	80	100	0.25	0.25	Square wave, 0.6V, 0.95V, 3s each

Schematic 4.1. *a) A schematic of the square wave cycle of the AST and (b) testing procedure and sequence of characterization experiments for a single cycle of the AST.*

Table 4.1 *Relative humidity, gas type and gas flow rates of different MEAs*

MEA name	AST RH (%)	Gas used during AST	Gas flowrate, anode/cathode (sccm)
N_2 Dry	40	N_2	200/200
N_2 Wet	100	N_2	200/200
Air Dry	40	Air	210/830
Air Wet	100	Air	210/830

4.2.3 Electrochemical Characterization

Cyclic voltammetry measurements were conducted with potential sweep from 0.095 V to 0.8 V at a scan rate of 20 mVs^{-1}. LSVs were used to measure H_2 cross-over and were conducted from 0.05 V to 0.8 V at a scan rate of 1 mVs^{-1}. EIS was done from 10 kHz to 0.01 Hz at 0 V vs OCV with 5 points per decade. All the previously mentioned tests were performed in H_2/N_2 environment with 200 sccm/300 sccm flow rates at anode/cathode, with 100% relative humidity (RH) at atmospheric pressure. Polarization curves were generated by holding the cell at constant currents for 3 minutes and measuring the corresponding voltage values with six points in the activation region. Voltage

values were averaged over these 3 minutes for both forward and backward scans. The test was performed at 150 kPa(a) backpressure with a stoichiometry of 1.5/1.8 in H_2/Air environment (anode/cathode) in 100% RH according to the fuel cell tech team (FCTT) polarization protocol. The polarization curves were preceded with a recovery protocol, which consisted of holding the cell voltage at 0.2 V, at 40 ˚C, 150 % RH and with flowrates of 300 sccm/200 sccm to retrieve all the recoverable losses and to ensure the polarization data is collected at the same starting conditions for all MEAs. BOL stage data was achieved by performing a cell break-in procedure on a fresh MEA which consisted of potential holds of 30 seconds at 0.8V, 0.6V and 0.3V respectively until constant current was achieved. Mass activity measurements were only done at the beginning of life (BOL) and at the end of life (EOL) by holding the cell potential at 0.9 V for 15 minutes, measuring the corresponding current in H_2/O_2 environment at high flow rates of 1000 sccm/2500 sccm and 150 kPa(a) backpressure.

4.2.4 Electrochemically Active Surface Area (ECSA) calculation

The ECSA was calculated using the standard hydrogen under potential deposition (H_{UPD}) region, where the area under the H_{UPD} region of the CV, was integrated to acquire the ECSA:

$$ECSA = \frac{i \times V}{L \times \upsilon \times 210} \tag{4.1}$$

where, the nominator represents the area of the H_{UPD} region of the CV, L is the loading of the electrocatalyst, 210μCcm^{-2} is the unit charge and υ is the scan rate under which the CVs were performed.

4.2.5 Post-mortem analysis

Cross-sectional scanning electron microscopy (SEM) was performed to identify degradation of Pt nanoparticles and also to identify morphological changes on the catalyst layer due to degradation. The following procedure was followed to obtain sample cross-sections from the SEM. First, an area of about 1 cm × 1 cm in the middle of the MEA was cut from the MEA, which was then sandwiched between stainless steel or glass plate to keep flat. The assembly was then mounted in epoxy and sectioned to expose the cross-section. Multiple polishing paper was used to polish the cross-section with finish progressively increasing from 320 grit to 1200 grit. The polished cross-section was imaged in a JOEL-7200F field emission scanning electron microscope, equipped with an Oxford Instruments X-MaxN EDS detector. Catalyst layer thickness measurement was carried out using ImageJ. Multiple measurements were taken at various locations across the entire 1 cm length of the cross-section.

4.2.6 Micro X-ray Diffraction

Post-mortem synchrotron X-ray micro-diffraction mapping were conducted at Beamline 12.3.2 of the Advanced Light Source (ALS) at Lawrence Berkeley National Laboratory. A 10 keV monochromatic X-ray beam was focused to ~2×5 μm^2 by Kirkpatrick−Baez mirrors. The degraded MEA dissembled from testing hardware was mounted on a x−y scan stage and tilted 25° relative to the incident beam. Diffraction images were recorded in reflection mode with a two-dimensional Pilatus-1 M detector mounted at 60° to the incoming X-ray, approximately 150 mm away from the probe spot. Exposure time at each position was 10 s. Calibrations for distance, center channel position, and tilt of detector were performed on the basis of a powder pattern obtained from a reference Al_2O_3 particles taken at the same geometry. For mapping/imaging of each 1×1 cm^2 area

of each MEA samples. A scan of 50 × 20 points was performed with a step size of 200 µm on x-axis and 500 µm on y-axis. Finer 200 µm step size in x-axis was adopted to resolve the flow field channel (~0.78 mm) and land (~0.92 mm). The X-ray scan diffraction data was then processed by XMAS[226]. Diffraction rings were integrated along the azimuthal direction and the peak width were determined by fitting of a 2d Lorentzian function with an angular resolution of~0.02°. Instrumental broadening was estimated using large Al_2O_3 crystals powder in the exact same detector configuration. The estimated Pt particle size is an average from both cathode and anode catalyst for each measured location, since the synchrotron X-ray penetrates both cathode and anode, In our measurement, change of Pt particle size before and after AST is dominated by the cathode Pt catalyst particle size increase, as minimal particle size growth occurred on the anode side, when the anode was fixed at 0 V vs S.H.E in pure H_2 environment during AST.

4.2.7 X-ray CT

Ex-situ X-ray computed tomography (CT) of MEAs was performed at Beamline 8.3.2 at Advanced Light Source (ALS) synchrotron at Lawrence Berkeley National Laboratory (LBNL), Berkeley, CA. Monochromatic x-rays with 25 keV energy were selected. 50 µm LuAg:Ce scintillator, 10x lenses and sCMOS PCO Edge camera were used to produce image with 0.65 um/pix. 200 ms exposure time was used with 1300 images collected per scan. To create the X-ray CT images, a three-dimensional image stack is reconstructed using two-dimensional radiographs collected from 0 to 180^o rotation. The reconstructions and phase retrieval were performed using the Gridrec algorithm [227,228] with open-source TomoPy.[229] The reconstruction parameters and details are described previously.[230,231] Image processing and 8-bit conversion were carried out with open-source Fiji/ImageJ[232] Dragonfly was used for 3D rendering.

4.2.8 X-ray Photoelectron Spectroscopy (XPS)

The XPS data were measured by Kratos AXIS Supra X-ray photoelectron spectrometer, with a monochromatic Al Kα operating at 225 W for survey spectra and 300 W for high-resolution spectra. The survey spectra were acquired using 160 eV pass energy, 1 eV step size, 100 ms dwell time, while the high-resolution spectra were acquired using 20 eV pass energy, 0.1 eV step size, 100 ms dwell time. For each spectrum, the data were averaged by three random sample points and each sample point was averaged by specific cycles of scanning. All spectra were analyzed using CasaXPS software and fitted with 70 % Gaussian / 30 % Lorentzian line shape.

4.3 Results and Discussion

Error! Reference source not found. shows polarization curves for four MEAs during AST protocol. O ver the course of 30,000 cycles (~ 50 hours) all four MEAs showed potential loss that is an indication of degradation taking place. Comparing the polarizaton curves for BOL and EOL for four MAEs the clear trend emerges, where higher potential loss at medium and high current densities is observed for MEAs cycled with ASTs in N_2 compared to those in air. Over the course of 30,000 AST cycles, N_2 Wet MEA has the largest polarization loss, which amounts to 0.2 V at 0.8 A/cm^2. For all of four MEAs the polarization curves at the BOL and after 1000 cycles either showed minimal difference (N_2 Wet), showed improved performance after 1000 cycles (Air Dry) or did not show any differences (N_2 Dry and Air Wet). 1,000 AST cycles translates to 1.67 hours of testing. The improvement or no change of polarization is possibly because the cell was not fully conditioned, and these 1.67 hours were still conditioning the cell. Previous study has shown that for Pt/C (low surface area) the mass activity improves during first three voltage recovery cycles.[233] For the Air Dry MEA we observe OCV of 0.95 V at BOL and decrease to, 0.94 V, 0.93 V at 15,000 and 30,000 cycles respectively. The OCV reported here is collected after voltage recovery, as

shown by Schematic 1. During AST cycle the OCV decreases to 0.87 V, which is lower than 0.95 V used for N_2 ASTs. The OCV decrease during the cycling caused the AST cycling to be performed at lower values of UPL, which reduced the amount of Pt being dissolved. As discussed in Introduction section this lower rate of degradation is due to lower amount of PtO at lower potential.[111,234,235] The potential loss during AST for all four MEAs from 1000 to 5000 cycles, from 5000 to 15,000 cycles and from 15,000 to 30,000 cycles can be approximated as equipotential within MEA but different between MEAs. We will discuss the correlation between the polarization loss and ECSA loss in the upcoming sections.

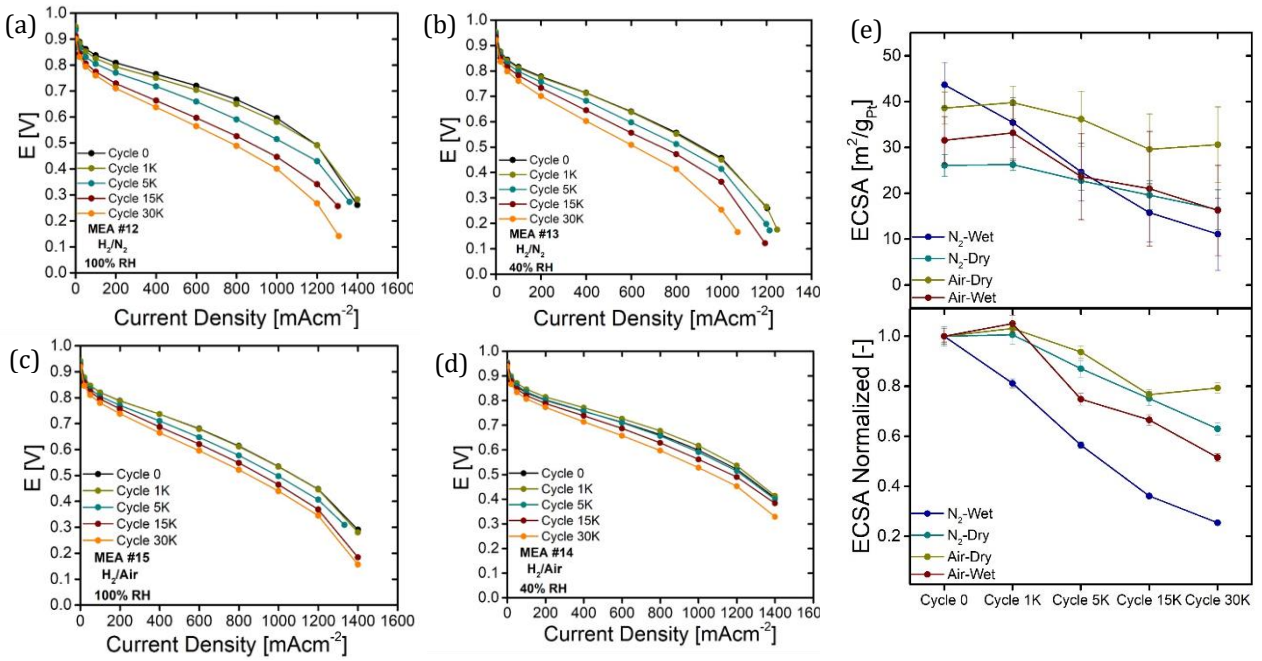

Figure 4.2 *Polarization curves collected after 0, 1000, 5000, 15000 and 30000 AST cycles for a) N_2 Dry, b) N_2 Wet, c) Air Dry and d) Air Wet. The AST conditions are reported in Table 4.1. The polarization curves were carried at 80°C, 100 % RH, 210 sccm/830 sccm anode/cathode. e) ECSA as a function of AST cycle number for N_2 Dry, N_2 Wet, Air Dry and Air Wet MEAs (top). Normalized ECSA as a function of AST cycle number (bottom).*

Figure a-d show cyclic voltammetry curves for four MEAs from BOL to cycle 30,000. The ECSA of each experiment was calculated from the charge integrated under the H_{UPD} region with **Eq. (4.1)**. For all MEAs with ageing the following observations were made regarding the CVs: 1) the loss of the H_{UPD} region, 2) the loss of adsorbed oxide species on Pt surface and 3) an increase

in double layer capacitive current between 0.5 and 0.65 V. The most pronounced reduction in H_{UPD} region was observed for N_2 Wet and N_2 Dry, where, together with the decrease in ECSA, we recognize a reorganization in the Pt crystal structure, as we see almost complete disappearance of the peak in the region between 0.1 and 0.15 V, generally associated with the Pt(110) direction.[236] Pt(110) has shown to be the most unstable surface in rotating disk experiments, hence it is not surprising that its loss is the most pronounced in this study.[236]

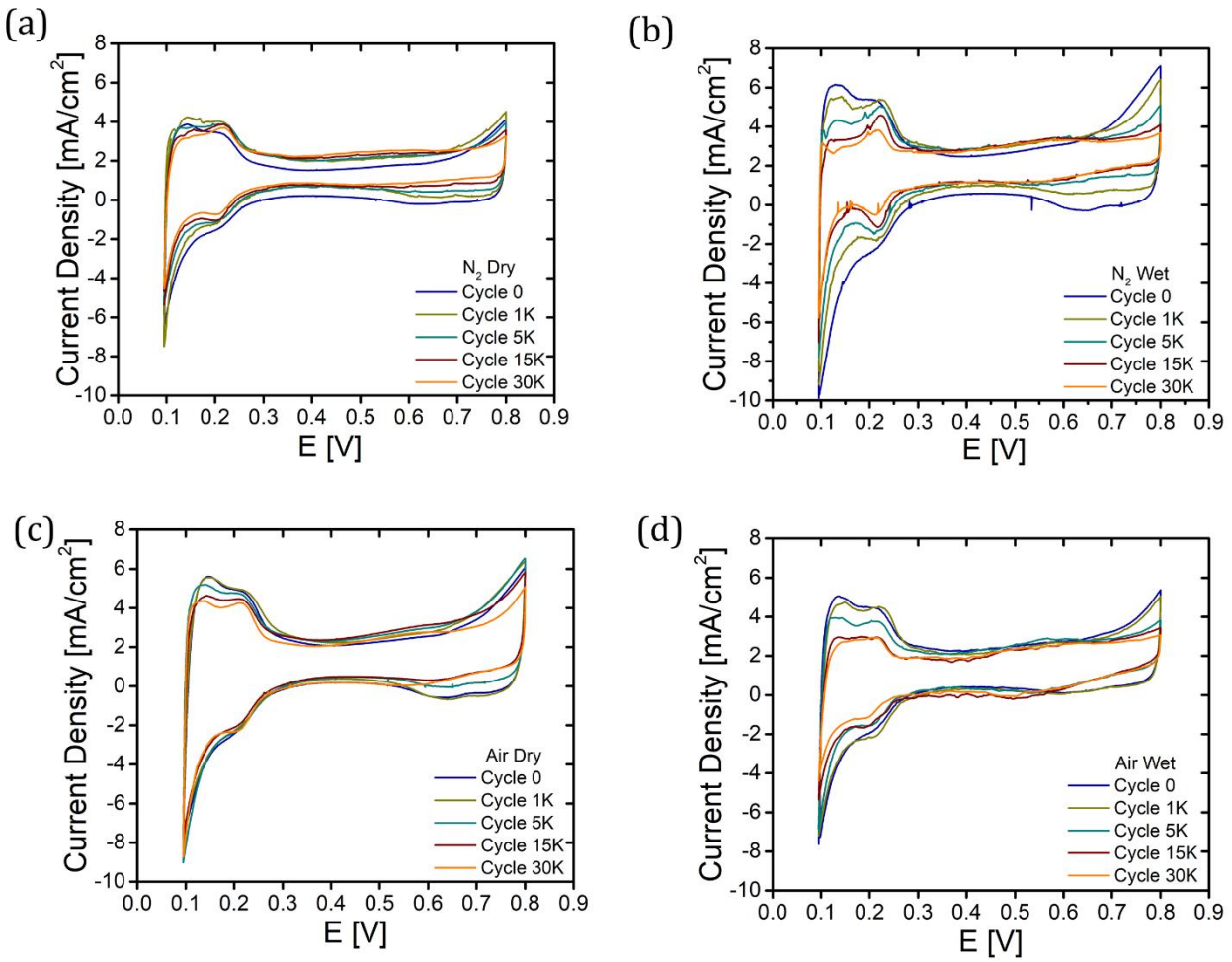

Figure 4.3. *Cyclic voltammograms collected after 0, 1000, 5000, 15000, 30000 AST cycles for a) N_2 Dry, b) N_2 Wet, c) Air Dry and d) Air Wet. The AST conditions are reported in Table 1. The CVs were carried with H_2/N_2 at 80C, 100 % RH, 200 sccm/300 sccm anode/cathode.*

Figure 4.2 e shows the relationship between the calculated (top) and normalized (Bottom) ECSA and the cycle number. We observe a variation in BOL ECSA between 25 and 43 m^2/g. N_2 Dry

MEA has the lowest ECSA at the BOL and this is also due to catalyst layer being thinner than the other three MEAs (**Table 4.**). There is a slight increase in the ECSA values at 1000 cycles for 3 MEAs but N_2 Wet, which can be attributed to the possibility that the cell was not completely conditioned. This increase has also been reported before.[237] A decrease in ECSA is observed for all MEAs during AST cycling after 1000 cycles. Undoubtfully, N_2 Wet MEA shows the highest catalyst degradation, from 43 m^2/g at BOL to 10 m^2/g after 30,000 cycles. Compared to the other three MEAs, this MEA started out with the highest ECSA and ended up with the lowest. Only 25% of ECSA is left at the EOL. This is mostly due to the UPL that remains at 0.95 V. As already discussed in Introduction section, the ECSA loss scales with the UPL. Air Dry has the least ECSA loss and it maintains 80 % of its ECSA at the EOL (from 38 m^2/g at BOL to 32 m^2/g at EOL). Whereas Air Wet and N_2 Dry show somewhat similar ECSA loss, maintaining 52 % and 62 % of the BOL ECSA and having 18 m^2/g at the EOL. During Air AST the UPL was reduced to slightly below 0.9 V for both cases for air. This lower UPL results in lower ECSA loss. Due to numerous repetitions of oxidation and reduction of the Pt during AST cycle, Ostwald ripening and particle dissolution are the dominant degradation mechanisms in the cells which lead to loss of ECSA and larger Pt particle size.

With the loss of the ECSA the change of activation overpotential of ORR can be calculated by taking the ratio of two Tafel equations for BOL and that during ageing and rearranging to obtain the following:

$$\Delta\eta = \frac{2.303RT}{\alpha F}\log\left(\frac{i_0 \cdot ECSA_{BOL}}{i_0 \cdot ECSA_{Aging}}\right) \tag{4.2}$$

where $\Delta\eta$ is the change in ORR overpotential from BOL to that during ageing, i_0 is exchange current density that is assumed to be constant,[185] R is gas constant, T is temperature, F is Faraday's

constant and α is the symmetry coefficient that is taken to be 1 at low current densities. Only ECSA changes during the ageing. When $\Delta\eta$ is plotted against log($ECSA_{ratio}$), a Tafel slope can be calculated and compared to the expected 70 mV/dec if all the overpotential losses during ageing are due to ECSA loss. Using **Eq. 4.2** we calculate Tafel slopes at low and high current densities, which are 100 and 800 mA/cm^2 and show them in **Table 4.2.** At 100 mA/cm^2 we observed Tafel slopes of 90, 134 and 74 mV/decade for N_2 Wet, Air Dry and Air Wet MEAs, respectively. Thus, N_2 Wet and Air Wet show close to expected 70 mV/dec loss of overpotential, which is indicative that the polarization loss for these two cases is mainly due to the ECSA loss. For Air Dry the high Tafel slope value of 134 mV/decade was observed, which is indicative that the polarization loss is not only due to ORR kinetics but might be affected by mass-transport or other phenomena. At 800 mA/cm^2 we calculated the Tafel slopes to be 200, 270 and 162 mV/decade for Wet N_2, Dry Air and Wet Air MEAs, respectively. At 800 mA/cm^2 we expect these Tafel slopes to be high, as activation, Ohmic and mass-transport losses are all significant. These values for N_2 Dry MEA were 195 and 507 mV/decade at 100 mA/cm^2 and 800 mA/cm^2, respectively. Again, the ECSA loss alone is insufficient for explaining the polarization loss. Overall, since the average electrode thickness was not changed during the AST cycling (see **Table 4.**), degradation of the catalyst support due to ageing is negligible.

Table 4.2 *Tafel slopes at low and high current densities*

Condition	Tafel slope at low current density (mV/decade)	Tafel slope at High current density (mV/decade)
Typical Value (Theoretical Value)	70	140
Air Dry	134	270
N_2 Dry	195	507
Air Wet	74	162
N_2 Wet	90	200

Figure shows the cross-sectional SEM images and EDS spectra. We observe that the membrane is reinforced with ~15 µm layer of PTFE in the middle. The cathode catalyst layers are observed on the right and show uniformity in thickness. There is a Pt-band seen in case of N_2 Wet conditions where Pt nanoparticles were reduced by H_2 and deposited inside the PEM (see **Figure f**).

Table 4.3 *Catalyst layer thickness of the four MEAs acquired with cross-sectional SEM*

	Control	**Air Wet**	**N_2 Wet**	**Air Dry**	**N_2 Dry**
SEM-Average Thickness (µm)	8.13 ± 0.59	9.32 ± 0.27	8.76 ± 0.26	8.13 ± 0.48	7.45 ± 0.17

The large loss of ECSA for N_2 Wet is possibly due to this loss of Pt. It is possible that the Pt band was formed in the other MEAs too, but it was not sufficiently pronounced to be observed by SEM. The Pt band formation is due to Pt dissolution and transport into the membrane and further reduction by crossing H_2 gas. The MEA thickness values are shown by **Figure g** and also tabulated in **Table 4.**, where thickness ranged from 8.13 to 9.32 µm for three MEAs but N_2 Dry, which had lower thickness of 7.45 µm. Furthermore, the two thicknesses from X-ray CT for Baseline and for Air Wet are reported in **Figure g**.

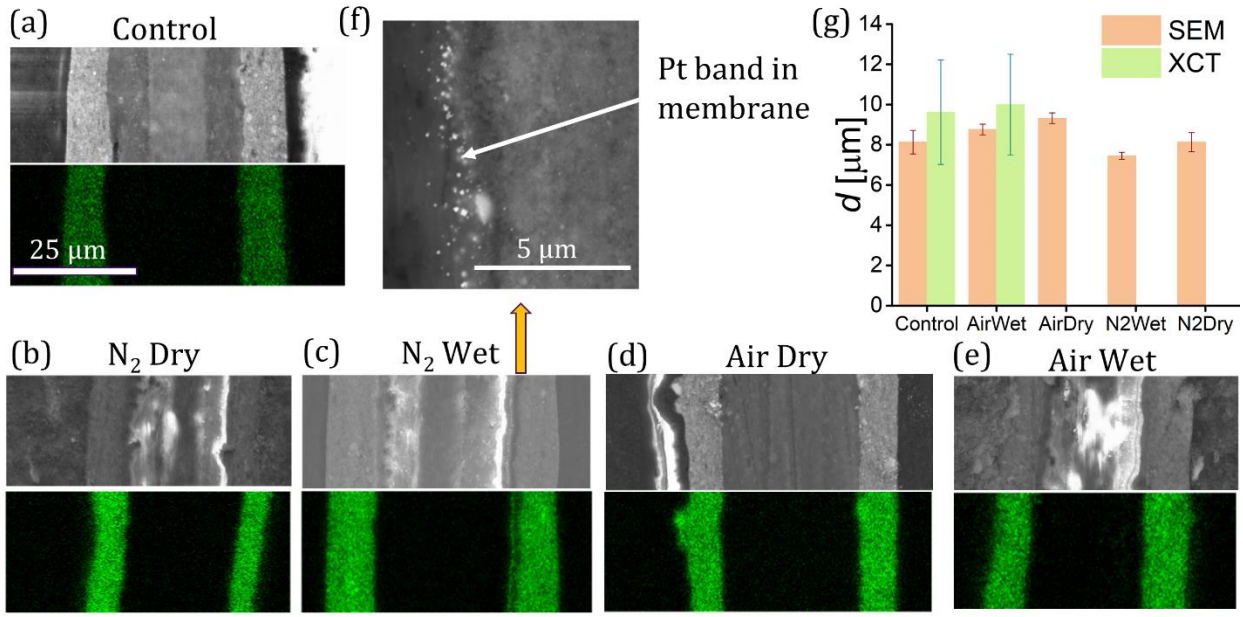

Figure 4.4. *(a-e top) Cross-sectional SEM images of the anode (left), PEM and cathode (right) catalyst layers and their respective EDS images, (f) SEM image of the Pt-band formed within PEM for N_2 Wet AST and (g) the bar plot of the average thicknesses acquired from SEM and X-ray CT.*

Micro-XRD experiments were performed on the MEAs and the XRD maps for catalyst area near the inlet, outlet and in the middle are shown in **Figure 4.5**. The Control sample has uniform particle-size distribution of average 3.2 nm. These particle sizes are consistent with previously reported values of 2.9 and 3.0 nm with local TEM methods [238,239], and to the 3.3 nm estimated by XRD[240] for TKK TEC10E50E catalyst, which has also been used in this study and our earlier study[225]. At dry conditions (see **Figure 4.5 b**) the particle size growth is not significant compared to wet conditions (see **Figure 4.5 c**). For Air Dry, there is no observable particle size change compared to the Control sample. This is also the sample that maintained 80 % of its ECSA at the EOL, the condition for the XRD imaging, hence we didn't expect significant particles redistribution. N_2 Dry has some Pt particles size increase under the land in the middle and near the gas outlet. Maximum particle sizes that were observed were 7.0 nm in size. From the ECSA plots N_2 Dry maintained 62 % of its ECSA at the EOL. Thus, the loss of 38 % of ECSA can be attributed

to Pt dissolution and Ostwald ripening into 3.2- 7.0 nm particles. Air Wet and N_2 Wet showed the highest Pt particles growth under the lands and closer to outlet. The maximum Pt particles observed for N_2 Wet were 14 nm, which is 4.5 higher than the Control sample. For N_2 Wet the difference in particle sizes between the lands and channels is not as pronounced at the inlet and in the middle of the cell. Air Wet and N_2 Wet maintained 50 % and 25 % of their ECSA at the EOL. Air Wet had more significant change than N2 Wet from inlet to outlet. For Air Wet we expect higher water content near the gas outlet in this co-flow configuration as both gas feeds will be more humidified as they pass through the cell. This is due to current density and water generated at LPL of 0.6 V in air environment during cycling. In N_2 Wet no ORR current is generated at 0.6 V therefore we expect to have more uniform water distribution from inlet to outlet. Similar inlet/outlet degradation changes in air were observed previously.[241] The land-channel differences for Dry N_2, Wet Air and Wet N_2 can be attributed to lower temperatures under the lands and hence higher water content in the catalyst layer. Catalyst layer locations under the lands are colder, as lands conduct heat more

effectively. Higher water content in catalyst layers under the lands contributes to higher Pt ion mobility and dissolution, hence higher particle size-distribution under the land.

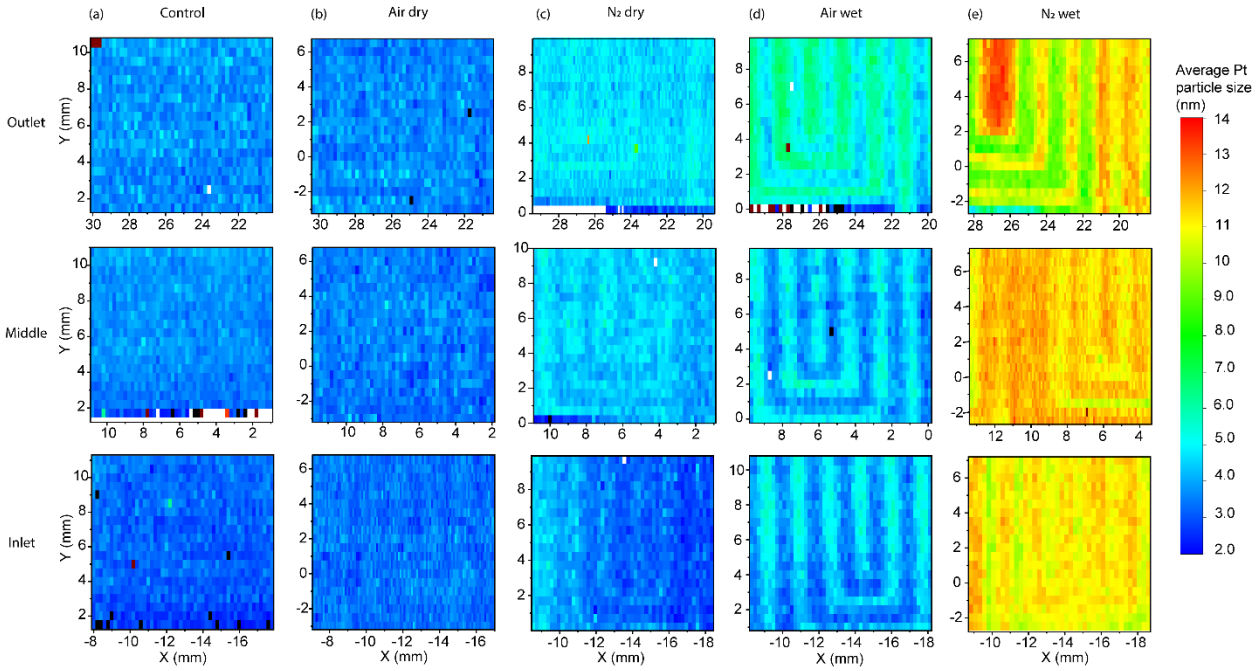

Figure 4.5. *BOL and post-mortem catalyst particle size distribution in three locations (outlet, inlet and middle) of the MEAs at BOL (a) control, post-mortem with (b) air in dry condition. (c) N_2 in dry condition, (d) air in wet condition and (d) N_2 in wet condition.*

The data from **Figure 4.4.** is summarized into particle size distribution plot, shown in **Figure 4.5**, where three locations, the fuel inlet, outlet and the middle of the MEAs are shown. The Control sample showed log-normal size distribution with mean particle sizes of 3 nm near inlet and increasing to 3.5 nm near the outlet. The inlet and outlet differences in particle sizes is mainly due to some Pt redistribution during conditioning procedure for the Control sample. For the Air Dry, the mean radius increased from 3.3 nm at the inlet to 3.6 at the outlet. For N_2 Dry the bi-modal Pt distribution was observed near the inlet with 3 and 4 nm mean Pt diameters, whereas for the outlet the mean increased to 4.6 nm.

For the Air Wet we report data published in our earlier manuscript[225], where bi-modal distribution is observed, with mean diameters increasing from 4 nm near inlet to 5.5 nm near outlet. Lastly, single log-normal sharp distribution is observed near inlet and in the middle of the cell for N_2 Wet, with mean diameters of 11 and 15 nm. The unimodal Pt distribution is due to the fact that Pt distribution is more uniform under land and channel, as observed in **Figure 4.6**. Near the outlet, we observe bimodal distribution again, due to smaller particles under the channel and larger Pt particles under the land, with mean radii of 9.5 nm and 11.5 nm. Ostwald ripening is more pronounced for inhomogeneous particle size distribution, as smaller particles within nanometer distance to larger particles will dissolve and redeposit onto the larger particles. Here, it is important to emphasize that locally (under land or under channel) a unimodal distribution is observed and only at land/channel interface these are bimodal.

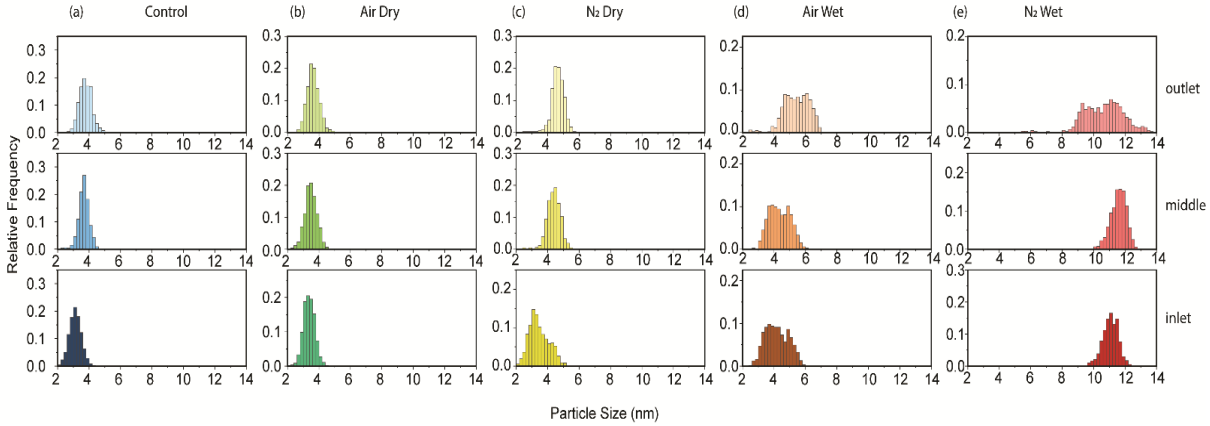

Figure 4.6 *BOL and post-mortem catalyst particle size distribution in three locations (outlet, middle and inlet) for four MEAs*

The XPS survey spectra results were shown in **Figure 4.7**, with the corresponding data listed **Table 4.4.** The high-resolution Pt 4f spectra in **Figure 4.9** reveals the surface environment from the metal view, as Pt^0, Pt^{2+} and Pt^{4+} represent metallic Pt, surface oxidized platinum and edge oxidized

platinum, respectively. XPS observed that N_2 Wet has the highest relative Pt^0 atomic concentration *ca.* 56% and Air Wet is the 2nd highest, about 48%, while the one of Control is only *ca.* 44%. Higher metallic Pt reveals a larger nanoparticle size as more platinum atoms will be located inside the nanoparticle and be catalytically inactive. In addition, the relative atomic concentrations of edge Pt^{4+} are found to be about 19.4%, 17.4%, 16.0%, 20.9%, and 18.4% for Control, N_2 Dry, N_2 Wet, Air Dry and Air Wet, respectively.

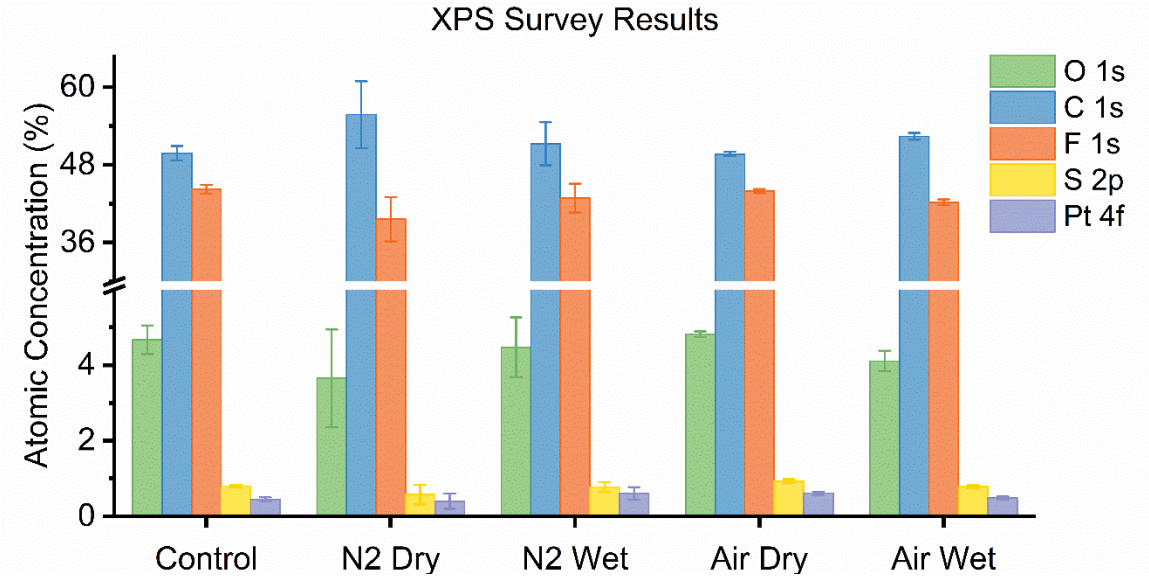

Figure 4.7 *The XPS survey results of five MEAs. The corresponding data was listed in Table 4.4.*

Table 4.4. *XPS Survey Results Corresponding Data*

	O 1s		C 1s		F 1s		S 2p		Pt 4f	
Sample	At%	Std	At%	Std	At%	Std	At%	Std	At%	Std
Control	4.67	0.38	49.80	1.12	44.27	0.68	0.80	0.04	0.45	0.06
N_2 Dry	3.65	1.29	55.76	5.16	39.61	3.42	0.58	0.26	0.40	0.20
N_2 Wet	4.47	0.79	51.28	3.31	42.86	2.23	0.78	0.13	0.61	0.16
Air Dry	4.82	0.07	49.67	0.34	43.97	0.31	0.93	0.05	0.61	0.04
Air Wet	4.11	0.27	52.41	0.52	42.21	0.45	0.79	0.04	0.48	0.04

In contrast with Pt^0, larger Pt nanoparticle size leads to smaller surface area and hence less edge platinum. In general, the high-resolution Pt 4f is also consistent with the Pt size distributions and

Pt band formation in cross-section SEM and micro-XRD described above, confirming that N_2 Wet has severe platinum dissolution and re-agglomeration. From **Figure 4.8 a** it is also interesting to observe that relative atomic concentrations of sp2 carbon (graphitic), which is the main chemical state of the carbon support but doesn't exist in ionomer structure, were ~32% for Control and Air Dry, about 36% for N_2 Wet and Air Wet, and as high as 41% for N_2 Dry.

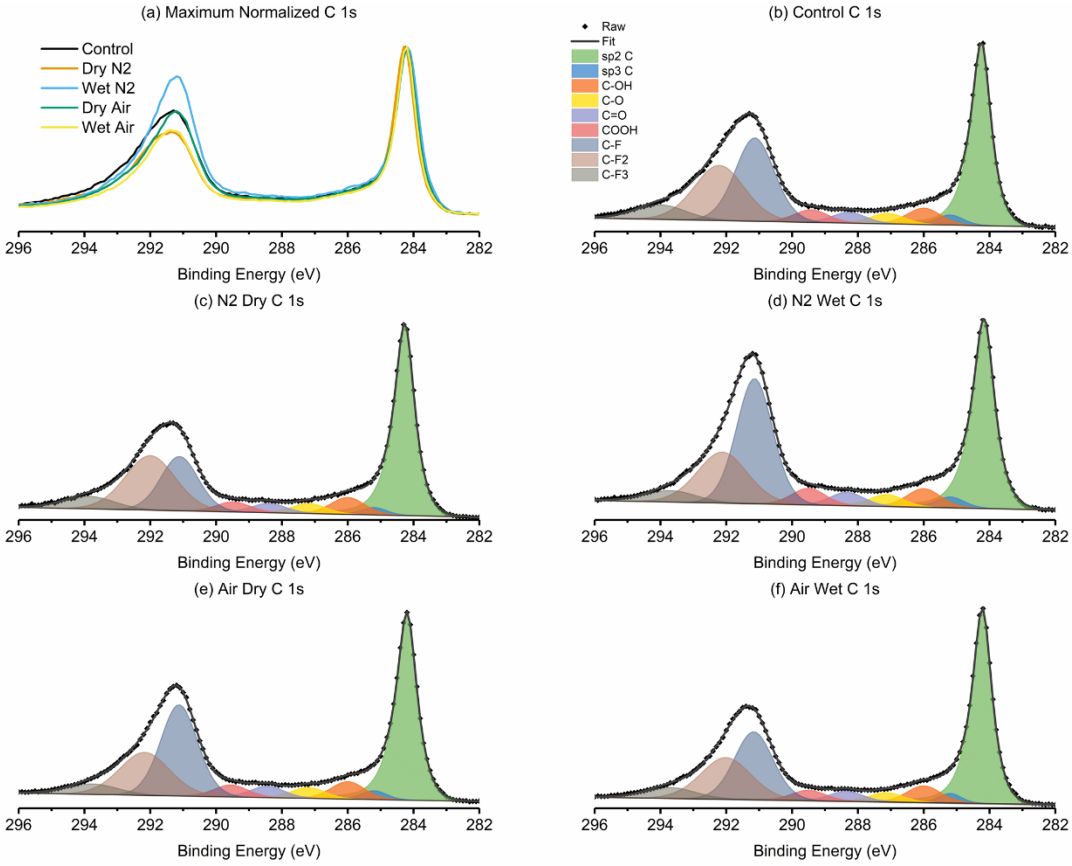

Figure 4.8. *Curve fitted high-resolution C 1s of five MEA: (a) Overlapped spectra with the maximum intensities normalized to 1 (a.u.); (b) Control; (c) N_2 Dry; (d) N_2 Wet; (e) Air Dry; (f) Air Wet.*

The high sp^2 concentration in N_2 Dry is consistent with the survey result indicating that it has the most nonuniform ionomer content. Another interesting region is the carbon-fluorine region ranges from 290-296 eV binding energy (the higher the BE is, the more F atoms are bonded with the C). Considering C-F, C-F_2 and C-F_3 are the characteristic states of sulfonate moiety node, the ionomer

backbone and the ionomer backbone terminal (not important) separately, the ratios of C-F/C-F_2 are calculated to be 1.17-0.84 for Control, 1.46-0.47 for N_2 Dry, 1.62-0.79 for N_2 Wet, 1.43-1.10 for Air Dry and 1.41-0.93 for Air Wet. The high deviations for N_2 Dry and N_2 Wet imply that they have worse sulfonate distributions, consistent with C/F ratios in survey spectra. The reason why N_2 Dry has the highest deviation in both C/F ratio (survey) and C-F/C-F_2 ratios (high-resolution) is probably that the sulfonate terminal group is hydrophilic and has less mobility in lower humidity.

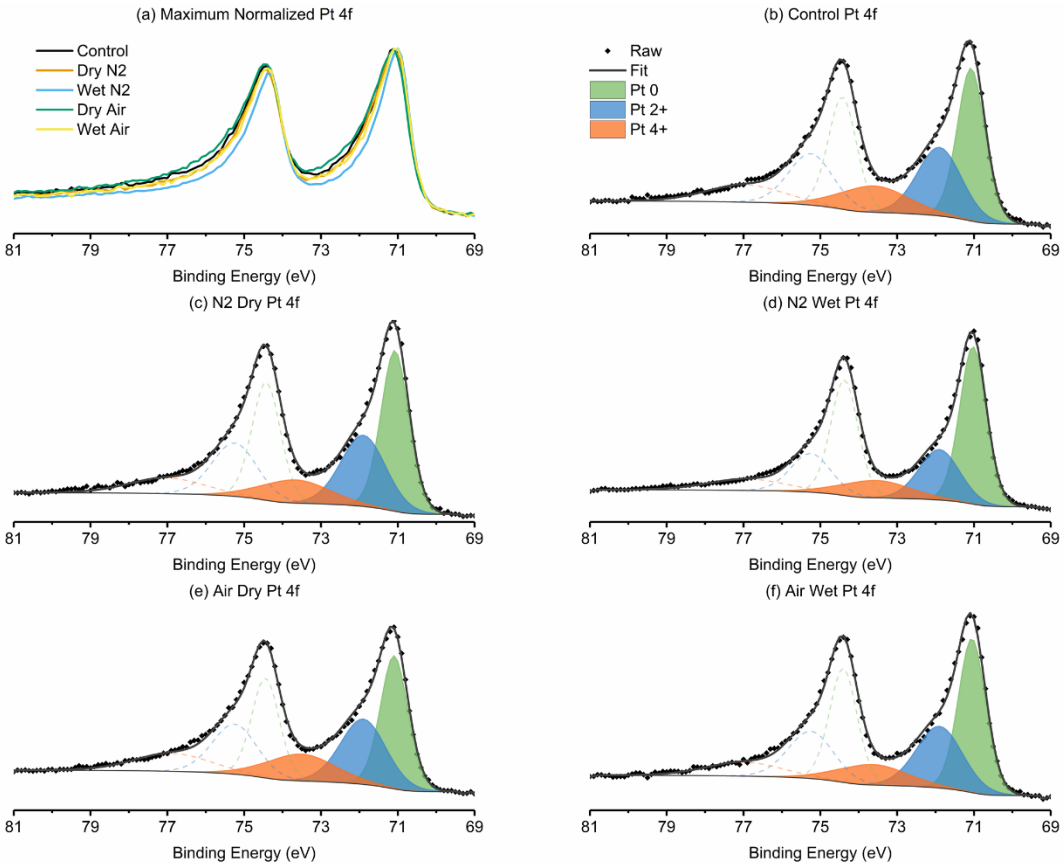

Figure 4.9. *Curve fitted high-resolution Pt 4f of five MEA: (a) Overlapped spectra with the maximum intensities of Pt 4f 7/2 normalized to 1 (a.u.); (b) Control; (c) N_2 Dry; (d) N_2 Wet; (e) Air Dry; (f) Air Wet.*

Figure 4.10 shows the X-ray computed tomography volume rendered images of the control MEA (**Figure 4.10 a**) and the MEA with AST cycling in wet conditions under air environment (**Figure b**). These images reveal the woven structure of the catalyst layer. After ageing some of the catalyst layer is swollen into a gap in microporous layer, which is a confirmation of the woven structure of

the catalyst layer (**Figure b**). As it was shown in **Table 4.** the CL thickness remains approximately unchanged during the AST, a result that has been confirmed via the X-ray CT data, where through comparing **Figure c** and **Figure 4.10 d** it is seen that the thickness of the CL remains unchanged after ageing. The inhomogeneity in catalyst layer thickness is mainly due to it being woven.

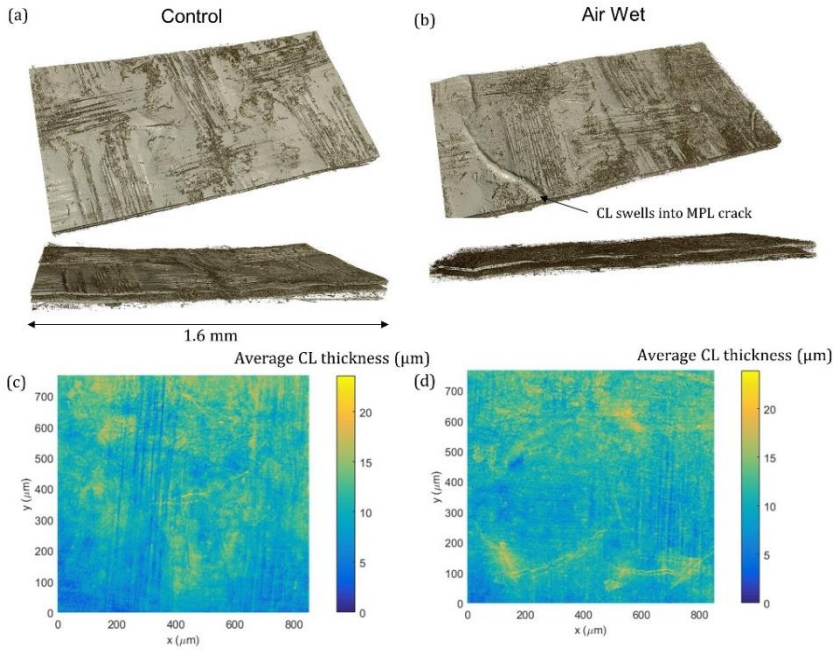

Figure 4.10. *X-ray CT volume-rendering of a) control and b) Air Wet MEA. The average CL thickness is shown as a 2D map for control (c) and Air Wet MEA. (d)*

To understand whether Pt loading distribution followed Pt particles distribution, or Pt particle growth was a local phenomenon, we perform synchrotron XRF experiments for Pristine and N_2 Wet MEA at the EOL. N_2 Wet MEA was selected because it showed the highest Pt particles size changes from land to channels. **Figure a**, shows the two imaged locations at the second serpentine bend near inlet and at the outlet. The XRF signal comes from both anode and cathode catalyst layers. We observe Pt loading reduction by 50 % between the Pristine sample and N_2 Wet sample. The ECSA loss was 80 %, whereas loading loss is 50 %. Some of these discrepancies

between the ECSA and loading loss is due to the fact that some of the Pt was dissolved and redeposited within membrane. This Pt is not electrically connected to the catalyst layer and thus does not contribute to ECSA, but it will be detected by XRF. **Figure 4.11 c** shows the Pristine XRF map of MEA, where inhomogeneity in Pt coating is observed. The spots with no catalyst show up to be around 500 µm in size. XRF also maps the woven structure of the catalyst layer, where optical image of catalyst layer is shown by **Figure 4.11 d**. Optical image clearly confirms that the structure of the catalyst layer is woven with thread size of 250 µm. Optical image of catalyst layer after N_2 Wet AST is shown by **Figure 4.11 d** (right), where imprint of lands is clearly seen. **Figure 4.11 e** shows the XRF map of the N_2 Wet MEA, where no significant Pt loading redistribution is observed under land and channel. Overall, the loading decreased by 50 % and the 2D XRF map shows slightly lower Pt loadings under the bends of the flow field. This observation confirms that Pt particle size growth under lands is primarily due to Ostwald ripening and is local phenomena.

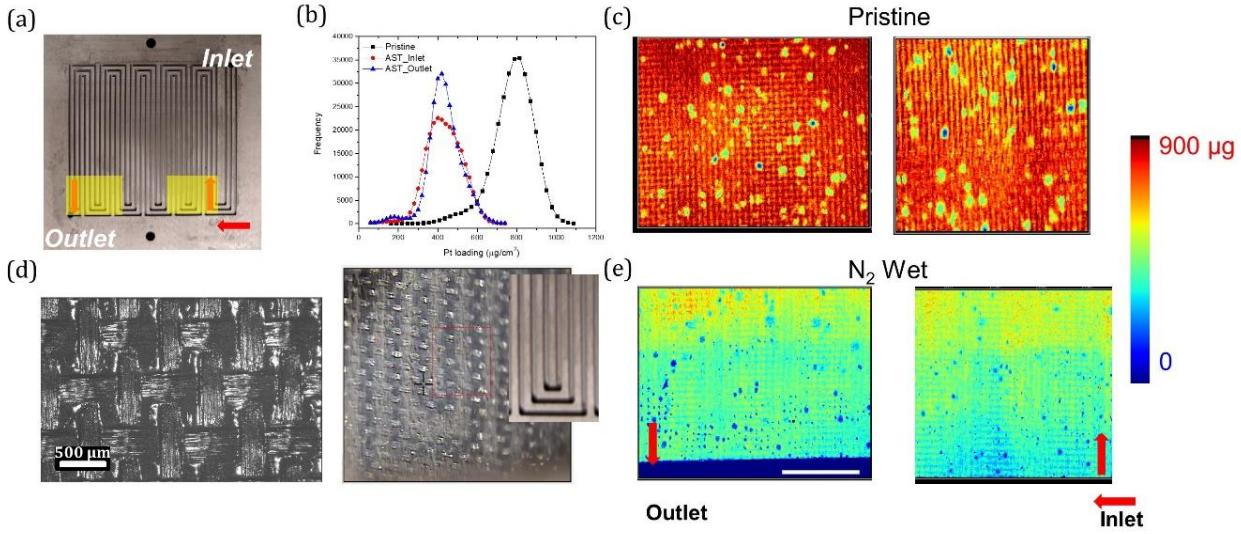

Figure 4.11. *Bipolar plates used in the fuel cell assembly and highlighted is where X-Ray CT (computer tomography) of the MEAs have been taken (a), the loading of Pt on the MEAs taken from X-ray CT (b) and the image of pristine MEA (c) and wet N_2 MEA (e). Optical images of the catalyst layer before and after cell assembly is also shown in (d)*

Figure 4.12 summarizes the land and channel differences in Pt dissolution during N_2 Wet and Air Wet ASTs. Under the land and in N_2 Wet AST Pt particles-sizes increases mainly due to high mobility of Pt ions and high redeposition rates. Furthermore, in this scenario we observed Pt-band formation within the membrane, which is also due to high Pt ions mobility. For N_2 Wet AST under the channel lower Pt dissolution rates are expected because of less water presence in the catalyst layer under the channel. For Air Wet AST smaller Pt particle sizes are observed under land compared to that in N_2 Wet and we attribute mainly due to decreasing UPL, due to reduced OCV during cycling. Fewer Pt^{2+} ions are observed due to lower amount of PtO formation at decreasing UPL. Also, under these AST conditions no Pt band formation was observed in membrane. For Air Wet AST under the channel Pt particles sizes are smaller, as there is less water and also lower UPL during cycling.

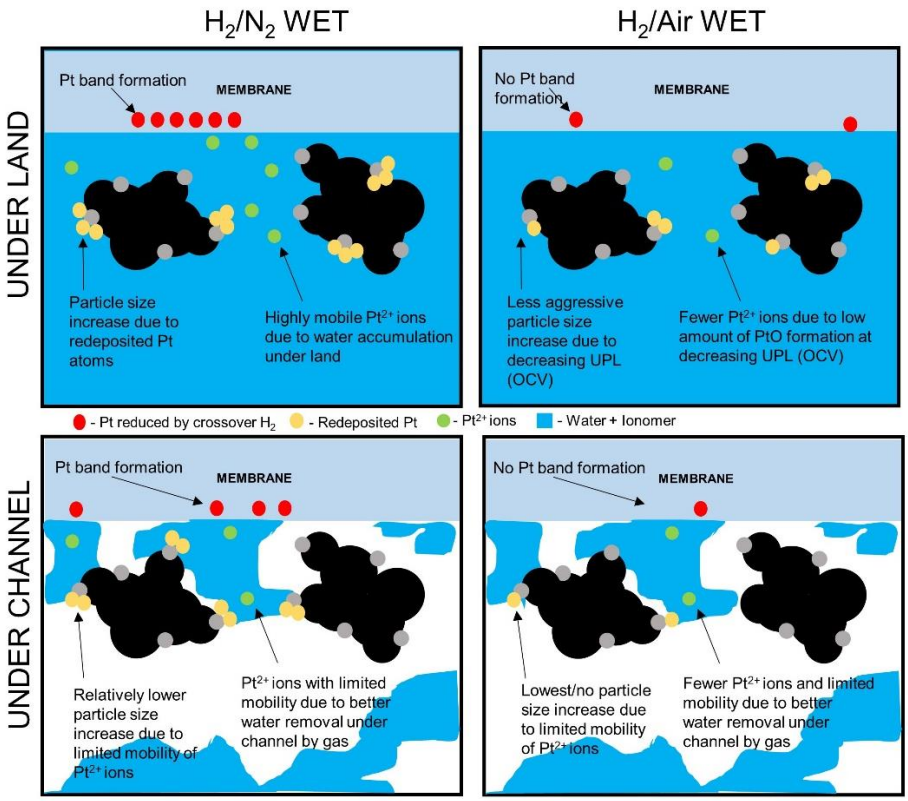

Figure 4.12. *A mechanistic summary of observed Pt degradation mechanisms in N2 and Air, Dry and Wet AST conditions.*

4.4 Conclusion

In this study the heterogenous degradation of PEM fuel cell MEAs under different RH and gas feeds was investigated. Four MEAs were tested under standard DOE FCTO AST conducted at 0.6 V – 0.95 V (or OCV) for 30,000 cycles. The ASTs conducted were in 40 % or 100 % RH H_2/Air and H_2/N_2, termed here as Air Dry, Air Wet or N_2 Dry and N_2 Wet. For H_2/Air experiments the UPL during AST was limited by the cell OCV, which decreased to about 0.87 V during 30,000 cycles. Polarization curves showed that potential decreased in all the regions: activation, ohmic and mass-transport from 1,000 cycles to 30,000 cycles. From BOL to 1,000 cycles the polarization did not change significantly perhaps due to the fact that the MEAs were still conditioning. Cyclic voltammetry plots showed that different Pt facets disappear at different rates (Pt(110) had highest dissolution rate) in the H_{UPD} region during cycling. Largest ECSA loss was observed for N_2 Wet, then Air Wet, N_2 Dry and Air Dry. MEA under N_2 Wet condition maintained only 25 % of its BOL ECSA. We calculated Tafel plots that plot potential differences between BOL and during ageing as functions of log ($ECSA_{ratio}$) at 100 mA/cm^2. For both N_2 and Air Wet the Tafel slopes were close to expected 70 mV/dec, whereas for N_2 and Air Dry they were significantly (twice or more) higher. The loss in polarization for MEAs in wet conditions is mainly due to ECSA loss, whereas for dry conditions there are additional losses in polarization that cannot be explained by ECSA loss only. Cross-sectional SEM, X-ray CT and EDS showed that the catalyst layer thickness remained approximately unchanged at the EOL. Optical imaging and micro X-ray CT showed that catalyst layers are woven. Micro-diffraction corroborated the ECSA change data during AST, showing the largest Pt particles (~14 nm) for N_2 Wet AST, second largest for Air Wet AST (~7 nm) and smaller for N_2 and Air Dry (~4-5 nm). For Air ASTs the UPL decreased during cycling, having lower amount of PtO and therefore lower Pt dissolution rate in the cathodic sweep.

Furthermore, micro-XRD shows significant differences in Pt sizes between lands and channels for both N_2 and Air Wet ASTs. The land-channel effects are due to higher water content in catalyst layer under the land, promoting Pt ion mobility. The Pt bimodal distribution is also observed at N_2 Wet outlet and Air Wet throughout, due to different particle sizes under lands and channels. We also observe significantly higher changes in Pt size from inlet to outlet for Air Wet compared to N_2 Wet AST. The growth of Pt particles in Air Wet from inlet to outlet is due to higher water content, as in Air at 0.6 V current density and water is generated and water or humidified gas is transported from inlet to outlet further humidifying MEA away from inlet. The XPS study showed that relative Pt^0 atomic concentration increased in a sequence N_2 Wet, Air Wet Air ASTs and Control. Higher metallic Pt content is due to larger nanoparticle size, as Pt^0 will be located inside the nanoparticle. The micro XRF study shows that Pt particle agglomeration is a local phenomenon, as Pt loading does not follow land-channel pattern or inlet-outlet and remains approximately uniform throughout the MEA. From the MEA design perspective for durable operation under dynamic load it is desirable to minimize the lands area to reduce colder locations under the land. Furthermore, operating in crossflow or using different gas flow-field configuration can help alleviate inlet-outlet differences in degradation. Lastly, designing dynamic load cycle with lower UPL by using system level control can lower Pt particles growth due to Ostwald ripening. Overall, for durability purposes it is desirable to operate at sub humidified conditions due to reduced Pt ion migration in ionomer, which is a function of water content. Therefore, higher temperature operation can help keeping lower relative humidity in the stack but at the same time it will contribute to other component (non-catalyst) degradation, therefore a careful optimization is needed.

Acknowledgements

The micro X-ray CT experiments used Beamline 8.3.2 and micro-diffraction mapping used Beamline 12.3.2 of the Advanced Light Source, which is a DOE Office of Science User Facility under contract no. DE-AC02-05CH11231. We thank Dr. Dilworth Parkinson for beamtime support. The X-ray CT volume-rendering data for this paper was generated using Dragonfly software, Version 3.6 for Windows. Object Research Systems (ORS) Inc, Montreal, Canada, 2018; software available at http://www.theobjects.com/dragonfly.

Chapter 5

Conclusion, Summary and Outlook

5.1 Conclusion, Summary and Outlook

The motivation of this thesis was to elucidate and separately investigate the influence of the carbon support and platinum nanoparticles loading and particle size on the rate determining step and reaction kinetics and transport limitation of oxygen reduction reaction. Additionally, we designed experiments to investigate such effects in a membrane electrode assembly set up. Furthermore, we explored the heterogenous degradation of industrially-made platinum nanoparticle supported on carbon using multi-modal characterizations.

Firstly, discussed the role of Pt nanoparticles (NPs) density and of the carbon support on the reactivity of Pt/C electrocatalysts for the oxygen reduction reaction (ORR). The electrocatalysts were synthesized using the polyol method, resulting in NPs with a diameter of ~ 2 – 3 nm, independent of the carbon support. HAADF-STEM images and XPS evidenced a preferential deposition of the NPs on the edges of the carbon sheets and the carbon structural defects. The investigation of the ORR reactivity was performed using kinetic isotope effect studies and it showed no involvement of protons in the rate determining step of the ORR when there is a high density of Pt NPs on the surface. However, when the density of Pt NPs decreases, a KIE appears, thus, which indicates an involvement of protons in the RDS. This implies that the carbon supports affect the mechanism of the ORR either by: *(i)* acting as a secondary catalyst, thus, promoting a parallel ORR to that of catalyzed by Pt NPs or by *(ii)* modifying the dispersion of the Pt NPs, thus leading in changes in their agglomeration or in the particle proximity effect and, thus, in their reactivity. The latter hypothesis was introduced due to stronger Pt-O2 bonds as the support specific surface area increases.

In a subsequent study, we selected two of the previously investigated carbon supports with a wide difference in their morphology and characterization, (*i.e.* specific surface areas of 97 and 890 m^2/g) and used these supports to synthesize different weight loadings of Pt electrocatalysts (3.5, 14, 30 wt.% and an attempt to saturate the surface of the support which lead to loadings of 42.2 wt.% and 68.8 wt.% for FCX100 and FCX800 respectively).

We confirmed that the degradation of the MEA is more severe under H2/N2 environments and in case of H2/Air, performance loss of the MEA in not only due to ECSA loss as other losses such as ohmic, transport and kinetic losses are also not negligible. We successfully eliminated the carbon support involvement in the ORR; thus, all the performance is due to Pt NPs participation in the ORR reactivity.

Finally, we studied the heterogenous degradation of PEM fuel cell MEAs under different relative humidity (RH) conditions and gas feeds was investigated. Four MEAs were tested under standard DOE FCTT AST conducted at 0.6 V – 0.95 V (or OCV) for 30,000 cycles. The ASTs conducted were in 40 % or 100 % RH H_2/Air and H_2/N_2. We calculated Tafel plots that plot potential differences between BOL and during ageing as functions of log ($ECSA_{ratio}$) at 100 mA/cm^2. For both N_2 and Air Wet the Tafel slopes were close to expected 70 mV/dec, whereas for N_2 and Air Dry they were significantly (at least with a factor of 2) higher. Micro-diffraction corroborated the ECSA change data during AST, showing the largest Pt particles (~14 nm) for N_2 Wet AST, second largest for Air Wet AST (~7 nm) and smaller for N_2 and Air Dry (~4-5 nm). Furthermore, micro-XRD shows significant differences in Pt sizes between lands and channels for both N_2 and Air Wet ASTs. The land-channel effects are due to higher water content in catalyst layer under the land, promoting Pt ion mobility. The micro XRF study shows that Pt particle agglomeration is a local phenomenon, as Pt loading does not follow land-channel pattern or inlet-outlet and remains

approximately uniform throughout the MEA. From the MEA design perspective for durable operation under dynamic load it is desirable to minimize the lands area to reduce colder locations under the land. Furthermore, operating in crossflow or using different gas flow-field configuration can help alleviate inlet-outlet differences in degradation. Lastly, designing dynamic load cycle with lower UPL by using system level control can lower Pt particles growth due to Ostwald ripening.

In short, our work has contributed to current problems within the fuel cell research community in several ways. Carbon support study has shown the parallel effect of the support in ORR reactivity and by eliminating such effect we were able to elucidate the proximity effect and particle size importance and the coverage effect of the Pt NPs on ORR. With our study on MEA degradation we were able to identify different effective factors in degradation and their importance under each circumstance under realistic automotive operation conditions. Overall, these results represent various ways for fuel cell manufacturers to increase MEA performance by optimizing catalyst coverage and loading with catalyst layer thickness and degradation by carefully controlling the operating conditions.

The continuation of this work lies in the investigation of the carbon support corrosion during startup/shutdown conditions of the fuel cell operation conditions, degradation tests under differential flow rate conditions and fuel starvation effects. As stated before, particle detachment is the dominant Pt NP degradation mechanism in potentials over 1 V in automotive operating conditions. Particle detachment occurs as a result of carbon support corrosion which diminishes the favorable deposition sites for Pt NPs leading to loss of active material. Fuel flow rates play a significant role as it can possibly cause fuel starvation throughout the membrane electrode assembly and induce oxidation of carbon, thus accelerate the degradation of the cell.

References

(1) Armaroli, N.; Balzani, V. The Future of Energy Supply: Challenges and Opportunities. *Angew. Chemie - Int. Ed.* **2007**, *46* (1–2), 52–66. https://doi.org/10.1002/anie.200602373.

(2) Lewis, N. S.; Nocera, D. G. Powering the Planet: Chemical Challenges in Solar Energy Utilization. *PNAS* **2006**, *103* (43), 15729–15735. https://doi.org/https://doi.org/10.1073/pnas.0603395103.

(3) Jacobson, M. Z. Review of Solutions to Global Warming, Air Pollution, and Energy Security. *Energy Environ. Sci.* **2009**, *2* (2), 148–173. https://doi.org/10.1039/b809990c.

(4) Tripkovic, V.; Vegge, T. Potential- and Rate-Determining Step for Oxygen Reduction on Pt(111). *J. Phys. Chem. C* **2017**, *121* (48), 26785–26793. https://doi.org/10.1021/acs.jpcc.7b07472.

(5) Cheng, X.; Shi, Z.; Glass, N.; Zhang, L.; Zhang, J.; Song, D.; Liu, Z. S.; Wang, H.; Shen, J. A Review of PEM Hydrogen Fuel Cell Contamination: Impacts, Mechanisms, and Mitigation. *J. Power Sources* **2007**, *165* (2), 739–756. https://doi.org/10.1016/j.jpowsour.2006.12.012.

(6) Bidault, F.; Brett, D. J. L.; Middleton, P. H.; Brandon, N. P. Review of Gas Diffusion Cathodes for Alkaline Fuel Cells. *J. Power Sources* **2009**, *187* (1), 39–48. https://doi.org/10.1016/j.jpowsour.2008.10.106.

(7) Farooque, M.; Maru, H. C. Fuel Cells - The Clean and Efficient Power Generators. *Proc. IEEE* **2001**, *89* (12), 1819–1829. https://doi.org/10.1109/5.975917.

(8) García, B. L.; Sethuraman, V. A.; Weidner, J. W.; White, R. E.; Dougal, R. Mathematical Model of a Direct Methanol Fuel Cell. *J. Fuel Cell Sci. Technol.* **2004**, *1* (1), 43. https://doi.org/10.1115/1.1782927.

(9) Swider-Lyons, K. E.; Carlin, R. T.; Rosenfeld, R. L.; Nowak, R. J. Technical Issues and Opportunities for Fuel Cell Development for Autonomous Underwater Vehicles. *Power Eng. Soc.* **2003**, 61–64. https://doi.org/10.1109/auv.2002.1177204.

(10) O'Sullivan, J. B. Fuel Cells in Distributed Generation. *Power Eng. Soc.* **1999**, 568–572.

(11) Kirubakaran, A.; Jain, S.; Nema, R. K. A Review on Fuel Cell Technologies and Power Electronic Interface. *Renew. Sustain. Energy Rev.* **2009**, *13* (9), 2430–2440. https://doi.org/10.1016/j.rser.2009.04.004.

(12) Saha, M. S.; Gullá, A. F.; Allen, R. J.; Mukerjee, S. High Performance Polymer Electrolyte Fuel Cells with Ultra-Low Pt Loading Electrodes Prepared by Dual Ion-Beam Assisted Deposition. *Electrochim. Acta* **2006**, *51* (22), 4680–4692. https://doi.org/10.1016/j.electacta.2006.01.006.

(13) Parker, J.; Karpiuk, R. S. Report of the Electrolytic Industries for the Year 1973. *J. Electrochem. Soc.* **2007**, *121* (11), 361C. https://doi.org/10.1149/1.2402356.

(14) Wilson, M. S. High Performance Catalyzed Membranes of Ultra-Low Pt Loadings for Polymer Electrolyte Fuel Cells. *J. Electrochem. Soc.* **2006**, *139* (2), L28. https://doi.org/10.1149/1.2069277.

(15) Appleby, A. J. Fuel Cell Technology and Innovation. *J. Power Sources* **1992**, *37* (1–2), 223–239. https://doi.org/10.1016/0378-7753(92)80080-U.

(16) Sasaki, K.; Naohara, H.; Cai, Y.; Choi, Y. M.; Liu, P.; Vukmirovic, M. B.; Wang, J. X.; Adzic, R. R. Core-Protected Platinum Monolayer Shell High-Stability Electrocatalysts for Fuel-Cell Cathodes. *Angew. Chemie - Int. Ed.* **2010**, *49* (46), 8602–8607. https://doi.org/10.1002/anie.201004287.

(17) Markovic, N. M.; Wang, G.; Fowler, B.; Ross, P. N.; Lucas, C. A.; Stamenkovic, V. R.; Mun, B. S. Improved Oxygen Reduction Activity on Pt3Ni(111) via Increased Surface Site Availability. *Science (80-.).* **2007**, *315* (5811), 493–497. https://doi.org/10.1126/science.1135941.

(18) Zhang, J.; Mo, Y.; Vukmirovic, M. B.; Klie, R.; Sasaki, K.; Adzic, R. R. Platinum Monolayer Electrocatalysts for O 2 Reduction: Pt Monolayer on Pd(111) and on Carbon-Supported Pd Nanoparticles. *J. Phys. Chem. B* **2004**, *108* (30), 10955–10964. https://doi.org/10.1021/jp0379953.

(19) Spiegel, C. https://www.fuelcellstore.com/blog-section/fuel-cell-modeling-basics.

(20) Wu, J.; Yang, H. Platinum-Based Oxygen Reduction Electrocatalysts. *Acc. Chem. Res.* **2013**, *46* (8), 1848–1857. https://doi.org/10.1021/ar300359w.

(21) Strmcnik, D.; Uchimura, M.; Wang, C.; Subbaraman, R.; Danilovic, N.; van der Vliet, D.; Paulikas, A. P.; Stamenkovic, V. R.; Markovic, N. M. Improving the Hydrogen Oxidation Reaction Rate by Promotion of Hydroxyl Adsorption. *Nat. Chem.* **2013**, *5* (4), 300–306. https://doi.org/10.1038/nchem.1574.

(22) Nørskov, J. K.; Rossmeisl, J.; Logadottir, A.; Lindqvist, L.; Kitchin, J. R.; Bligaard, T.; Jónsson, H. Origin of the Overpotential for Oxygen Reduction at a Fuel-Cell Cathode. *J. Phys. Chem. B* **2004**, *108* (46), 17886–17892. https://doi.org/10.1021/jp047349j.

(23) Stariha, S.; Macauley, N.; Sneed, B. T.; Langlois, D.; More, K. L.; Mukundan, R.; Borup, R. L. Recent Advances in Catalyst Accelerated Stress Tests for Polymer Electrolyte Membrane Fuel Cells. *J. Electrochem. Soc.* **2018**, *165* (7), F492–F501. https://doi.org/10.1149/2.0881807jes.

(24) Meier, J. C.; Galeano, C.; Katsounaros, I.; Topalov, A. A.; Kostka, A.; Schüth, F.; Mayrhofer, K. J. J. Degradation Mechanisms of Pt/C Fuel Cell Catalysts under Simulated Start-Stop Conditions. *ACS Catal.* **2012**, *2* (5), 832–843. https://doi.org/10.1021/cs300024h.

(25) Sharma, R.; Gyergyek, S.; Li, Q.; Andersen, S. M. Evolution of the Degradation Mechanisms with the Number of Stress Cycles during an Accelerated Stress Test of Carbon Supported Platinum Nanoparticles. *J. Electroanal. Chem.* **2019**, *838* (December 2018), 82–88. https://doi.org/10.1016/j.jelechem.2019.02.052.

(26) Topalov, A. A.; Cherevko, S.; Zeradjanin, A. R.; Meier, J. C.; Katsounaros, I.; Mayrhofer, K. J. J. Towards a Comprehensive Understanding of Platinum Dissolution in Acidic Media. *Chem. Sci.* **2014**, *5* (2), 631–638. https://doi.org/10.1039/c3sc52411f.

(27) Cherevko, S.; Keeley, G. P.; Geiger, S.; Zeradjanin, A. R.; Hodnik, N.; Kulyk, N.; Mayrhofer, K. J. J. Dissolution of Platinum in the Operational Range of Fuel Cells. *ChemElectroChem* **2015**, *2* (10), 1471–1478. https://doi.org/10.1002/celc.201500098.

(28) Jahnke, T.; Futter, G. A.; Baricci, A.; Rabissi, C.; Casalegno, A. Physical Modeling of Catalyst Degradation in Low Temperature Fuel Cells: Platinum Oxidation, Dissolution, Particle Growth and Platinum Band Formation. *J. Electrochem. Soc.* **2020**, *167* (1), 013523. https://doi.org/10.1149/2.0232001jes.

(29) Du, L.; Shao, Y.; Sun, J.; Yin, G.; Liu, J.; Wang, Y. Advanced Catalyst Supports for PEM Fuel Cell Cathodes. *Nano Energy* **2016**, *29*, 314–322. https://doi.org/10.1016/j.nanoen.2016.03.016.

(30) Mitsushima, S.; Kawahara, S.; Ota, K. I.; Kamiya, N. Consumption Rate of Pt under Potential Cycling. *J. Electrochem. Soc.* **2007**, *154* (2), 153–158. https://doi.org/10.1149/1.2400596.

(31) Uchimura, M.; Kocha, S. The Impact of Cycle Profile on PEMFC Durability. *ECS Trans.* **2007**, *11* (1 PART 2), 1215–1226. https://doi.org/10.1149/1.2781035.

(32) Pokhrel, A.; El Hannach, M.; Orfino, F. P.; Dutta, M.; Kjeang, E. Failure Analysis of Fuel Cell Electrodes Using Three-Dimensional Multi-Length Scale X-Ray Computed Tomography. *J. Power Sources* **2016**, *329*, 330–338. https://doi.org/10.1016/j.jpowsour.2016.08.092.

(33) Huang, S. Y.; Ganesan, P.; Park, S.; Popov, B. N. Development of a Titanium Dioxide-Supported Platinum Catalyst with Ultrahigh Stability for Polymer Electrolyte Membrane Fuel Cell Applications. *J. Am. Chem. Soc.* **2009**, *131* (39), 13898–13899. https://doi.org/10.1021/ja904810h.

(34) Selvaganesh, S. V.; Sridhar, P.; Pitchumani, S.; Shukla, A. K. A Durable Graphitic-Carbon Support for Pt and Pt3Co Cathode Catalysts in Polymer Electrolyte Fuel Cells. *J. Electrochem. Soc.* **2012**, *160* (1), F49–F59. https://doi.org/10.1149/2.051301jes.

(35) Burch, H. J.; Davies, J. A.; Brown, E.; Hao, L.; Contera, S. A.; Grobert, N.; Ryan, J. F. Electrical Conductance and Breakdown in Individual CN x Multiwalled Nanotubes. *Appl. Phys. Lett.* **2006**, *89* (14), 1–4. https://doi.org/10.1063/1.2358308.

(36) Shao, Y.; Sui, J.; Yin, G.; Gao, Y. Nitrogen-Doped Carbon Nanostructures and Their Composites as Catalytic Materials for Proton Exchange Membrane Fuel Cell. *Appl. Catal. B Environ.* **2008**, *79* (1), 89–99. https://doi.org/10.1016/j.apcatb.2007.09.047.

(37) Shao, Y.; Yin, G.; Gao, Y. Understanding and Approaches for the Durability Issues of Pt-Based Catalysts for PEM Fuel Cell. *J. Power Sources* **2007**, *171* (2), 558–566. https://doi.org/10.1016/j.jpowsour.2007.07.004.

(38) Imran Jafri, R.; Rajalakshmi, N.; Ramaprabhu, S. Nitrogen Doped Graphene Nanoplatelets as Catalyst Support for Oxygen Reduction Reaction in Proton Exchange Membrane Fuel Cell. *J. Mater. Chem.* **2010**, *20* (34), 7114–7117. https://doi.org/10.1039/c0jm00467g.
(39) Hagaman, E. W.; Murray, D. K.; Del Cul, G. D. Solid State 13 C and 19 F NMR Characterization of Fluorinated Charcoal . *Energy & Fuels* **2002**, *12* (2), 399–408. https://doi.org/10.1021/ef970156t.
(40) Guérin, K.; Pinheiro, J. P.; Dubois, M.; Fawal, Z.; Masin, F.; Yazami, R.; Hamwi, A. Synthesis and Characterization of Highly Fluorinated Graphite Containing Sp2 and Sp3 Carbon. *Chem. Mater.* **2004**, *16* (9), 1786–1792. https://doi.org/10.1021/cm034974c.
(41) Nansé, G.; Papirer, E.; Fioux, P.; Moguet, F.; Tressaud, A. Fluorination of Carbon Blacks: An X-Ray Photoelectron Spectroscopy Study: I. A Literature Review of XPS Studies of Fluorinated Carbons. XPS Investigation of Some Reference Compounds. *Carbon N. Y.* **1997**, *35* (2), 175–194. https://doi.org/10.1016/S0008-6223(96)00095-4.
(42) Yi, S.; Jiang, H.; Bao, X.; Zou, S.; Liao, J.; Zhang, Z. Recent Progress of Pt-Based Catalysts for Oxygen Reduction Reaction in Preparation Strategies and Catalytic Mechanism. *J. Electroanal. Chem.* **2019**, *848* (July), 113279. https://doi.org/10.1016/j.jelechem.2019.113279.
(43) Damjanovic, A.; Dey, A.; Bockris, J. O. M. Kinetics of Oxygen Evolution and Dissolution on Platinum Electrodes. *Electrochim. Acta* **1966**, *11* (7), 791–814. https://doi.org/10.1016/0013-4686(66)87056-1.
(44) Ruvinskiy, P. S.; Bonnefont, A.; Pham-Huu, C.; Savinova, E. R. Using Ordered Carbon Nanomaterials for Shedding Light on the Mechanism of the Cathodic Oxygen Reduction Reaction. *Langmuir* **2011**, *27* (14), 9018–9027. https://doi.org/10.1021/la2006343.
(45) Adzic, R. Recent Advances in Kinetics of Oxygen Reduction. 1996, pp 1–78.
(46) Damjanovic, A.; Brusic, V. Electrode Kinetics of Oxygen Reduction on Oxide-Free Platinum Electrodes. *Electrochim. Acta* **1967**, *12* (6), 615–628. https://doi.org/10.1016/0013-4686(67)85030-8.
(47) Garapati, M. S.; Sundara, R. Highly Efficient and ORR Active Platinum-Scandium Alloy-Partially Exfoliated Carbon Nanotubes Electrocatalyst for Proton Exchange Membrane Fuel Cell. *Int. J. Hydrogen Energy* **2019**, *44* (21), 10951–10963. https://doi.org/10.1016/j.ijhydene.2019.02.161.
(48) Wang, B. Recent Development of Non-Platinum Catalysts for Oxygen Reduction Reaction. *J. Power Sources* **2005**, *152* (1–2), 1–15. https://doi.org/10.1016/j.jpowsour.2005.05.098.
(49) Whiston, M. M.; Azevedo, I. L.; Litster, S.; Whitefoot, K. S.; Samaras, C.; Whitacre, J. F. Expert Assessments of the Cost and Expected Future Performance of Proton Exchange Membrane Fuel Cells for Vehicles. *Proc. Natl. Acad. Sci.* **2019**, *116* (11), 4899–4904. https://doi.org/10.1073/pnas.1804221116.
(50) H. Inoue, S.R. Brankovic, J.X. Wang, R. R. A. Oxygen Reduction on Bare and Pt Monolayer-Modified Ru(0001), Ru(10-10) and Ru Nanostructured Surfaces. *Electrochim. Acta* **2002**, *47*, 3777–3785. https://doi.org/10.1016/S0013-4686(02)00348-1.
(51) Matanović, I.; Garzon, F. H.; Henson, N. J. Theoretical Study of Electrochemical Processes on Pt-Ni Alloys. *J. Phys. Chem. C* **2011**, *115* (21), 10640–10650. https://doi.org/10.1021/jp111930w.
(52) Marcinkoski, J.; Spendelow, J.; Wilson, A.; Papageorgopoulos, D. DOE Hydrogen and Fuel Cells Program Record - Fuel Cell System Cost - 2017. *J. Mech. Robot.* **2017**, *9* (4), 1–9. https://doi.org/10.1115/1.4036738.
(53) Kongkanand, A.; Mathias, M. F. The Priority and Challenge of High-Power Performance of Low-Platinum Proton-Exchange Membrane Fuel Cells. *J. Phys. Chem. Lett.* **2016**, *7* (7), 1127–1137. https://doi.org/10.1021/acs.jpclett.6b00216.
(54) Kongkanand, A.; Subramanian, N. P.; Yu, Y.; Liu, Z.; Igarashi, H.; Muller, D. A. Achieving High-Power PEM Fuel Cell Performance with an Ultralow-Pt-Content Core-Shell Catalyst. *ACS Catal.* **2016**, *6* (3), 1578–1583. https://doi.org/10.1021/acscatal.5b02819.
(55) Greszler, T. A.; Caulk, D.; Sinha, P. The Impact of Platinum Loading on Oxygen Transport Resistance. *J. Electrochem. Soc.* **2012**, *159* (12), F831–F840. https://doi.org/10.1149/2.061212jes.
(56) Higashi, K.; Samjeské, G.; Takao, S.; Kaneko, T.; Sekizawa, O.; Uruga, T.; Iwasawa, Y. The

Relationship between the Active Pt Fraction in a PEFC Pt/C Catalyst and the ECSA and Mass Activity during Start-Up/Shut-Down Degradation by in Situ Time-Resolved XAFS Technique. *J. Phys. Chem. C* **2017**, *121* (40), 22164–22177. https://doi.org/10.1021/acs.jpcc.7b07264.

(57) Gasteiger, H. A.; Panels, J. E.; Yan, S. G. Dependence of PEM Fuel Cell Performance on Catalyst Loading. *J. Power Sources* **2004**, *127* (1–2), 162–171. https://doi.org/10.1016/j.jpowsour.2003.09.013.

(58) Rao, Y.; Zhou, F.; Fu, K.; Guo, W.; Pan, M. A Electrochemical Performance Analysis of High and Low Pt Loading in Pt/C Catalysts by Rotating Disk Electrode. *Int. J. Electrochem. Sci.* **2017**, *12* (6), 4630–4639. https://doi.org/10.20964/2017.06.91.

(59) A. Pozio*, M. De Francesco, A. Cemmi, F.Cardellini, L. G. Comparison of High Surface Pt/C Catalyssts by Cyclic Voltammetry. *J. Power Sources* **2002**, *105* (May 2001), 13–19.

(60) Lukaszewski, M.; Soszko, M.; Czerwiński, A. Electrochemical Methods of Real Surface Area Determination of Noble Metal Electrodes - an Overview. *Int. J. Electrochem. Sci.* **2016**, *11* (6), 4442–4469. https://doi.org/10.20964/2016.06.71.

(61) Vidaković, T.; Christov, M.; Sundmacher, K. The Use of CO Stripping for in Situ Fuel Cell Catalyst Characterization. *Electrochim. Acta* **2007**, *52* (18), 5606–5613. https://doi.org/10.1016/j.electacta.2006.12.057.

(62) S.Trasatti; Petrii, A. Real Surface Area Measurements in Ekectrochemistry. *Pure Appl. Chem.* **1991**, *63* (5), 711–734. https://doi.org/10.1351/pac199163050711.

(63) Strmcnik, D.; Tripkovic, D.; van der Vliet, D.; Stamenkovic, V.; Marković, N. M. Adsorption of Hydrogen on Pt(1 1 1) and Pt(1 0 0) Surfaces and Its Role in the HOR. *Electrochem. commun.* **2008**, *10* (10), 1602–1605. https://doi.org/10.1016/j.elecom.2008.08.019.

(64) Chen, Q. S.; Solla-Gullón, J.; Sun, S. G.; Feliu, J. M. The Potential of Zero Total Charge of Pt Nanoparticles and Polycrystalline Electrodes with Different Surface Structure: The Role of Anion Adsorption in Fundamental Electrocatalysis. *Electrochim. Acta* **2010**, *55* (27), 7982–7994. https://doi.org/10.1016/j.electacta.2010.03.050.

(65) Ciureanu, M. Electrochemical Impedance Study of Electrode-Membrane Assemblies in PEM Fuel Cells: I. Electro-Oxidation of H[Sub 2] and H[Sub 2]/CO Mixtures on Pt-Based Gas-Diffusion Electrodes. *J. Electrochem. Soc.* **1999**, *146* (11), 4031. https://doi.org/10.1149/1.1392588.

(66) Weaver, M. J.; Chang, S. C.; Leung, L. W. H.; Jiang, X.; Rubel, M.; Szklarczyk, M.; Zurawski, D.; Wieckowski, A. Evaluation of Absolute Saturation Coverages of Carbon Monoxide on Ordered Low-Index Platinum and Rhodium Electrodes. *J. Electroanal. Chem.* **1992**, *327* (1–2), 247–260. https://doi.org/10.1016/0022-0728(92)80151-S.

(67) Chattot, R.; Asset, T.; Bordet, P.; Drnec, J.; Dubau, L.; Maillard, F. Beyond Strain and Ligand Effects: Microstrain-Induced Enhancement of the Oxygen Reduction Reaction Kinetics on Various PtNi/C Nanostructures. *ACS Catal.* **2017**, *7* (1), 398–408. https://doi.org/10.1021/acscatal.6b02356.

(68) Yan, X.; Ge, X.; Cui, S. Pt-Decorated Nanoporous Gold for Glucose Electrooxidation in Neutral and Alkaline Solutions. *Nanoscale Res. Lett.* **2011**, *6* (1), 1–7. https://doi.org/10.1186/1556-276X-6-313.

(69) Wee, J. H.; Lee, K. Y.; Kim, S. H. Fabrication Methods for Low-Pt-Loading Electrocatalysts in Proton Exchange Membrane Fuel Cell Systems. *J. Power Sources* **2007**, *165* (2), 667–677. https://doi.org/10.1016/j.jpowsour.2006.12.051.

(70) Yingke Zhou, Kenneth Neyerlin, Tim S. Olson, Svitlana Pylypenko, Justin Bult, Huyen N. Dinh, Thomas Gennett, Z. S. and R. O. Enhancement of PEM Fuel Cell Performance by Steaming or Boiling the Electrode. *J. Power Sources* **2002**, *109* (1), 227–229. https://doi.org/10.1016/S0378-7753(02)00060-5.

(71) Qi, Z.; Kaufman, A. Low Pt Loading High Performance Cathodes for PEM Fuel Cells. *J. Power Sources* **2003**, *113* (1), 37–43. https://doi.org/10.1016/S0378-7753(02)00477-9.

(72) Lee, S. J.; McBreen, J.; Mukerjee, S.; Kho, Y. T.; Lee, T. H.; Rho, Y. W. Effects of Nafion Impregnation on Performances of PEMFC Electrodes. *Electrochim. Acta* **2002**, *43* (24), 3693–3701. https://doi.org/10.1016/s0013-4686(98)00127-3.

(73) O'hayre, R.; Lee, S. J.; Cha, S. W.; Prinz, F. B. A Sharp Peak in the Performance of Sputtered Platinum Fuel Cells at Ultra-Low Platinum Loading. *J. Power Sources* **2002**, *109* (2), 483–493. https://doi.org/10.1016/S0378-7753(02)00238-0.

(74) Wilson, M. S.; Gottesfeld, S. Thin-Film Catalyst Layers for Polymer Electrolyte Fuel Cell Electrodes. *J. Appl. Electrochem.* **1992**, *22* (1), 1–7. https://doi.org/10.1007/BF01093004.

(75) Makoto Uchida, Yuko Aoyama, N. E. and A. O. Investigation of the Microstructure in the Catalyst Layer and Effects of Both Perfluorosulfonate Ionomer and PTFE-Loaded Carbon on the Catalyst Layer of Polymer Electrolyte Fuel Cells. *J. Electrochem. Soc.* **2006**, *142* (12), 4143. https://doi.org/10.1149/1.2048477.

(76) Fang, B.; Chaudhari, N. K.; Kim, M. S.; Jung, H. K.; Yu, J. S. Homogeneous Deposition of Platinum Nanoparticles on Carbon Black for Proton Exchange Membrane Fuel Cell. *J. Am. Chem. Soc.* **2009**, *131* (42), 15330–15338. https://doi.org/10.1021/ja905749e.

(77) Jayawickrama, S. M.; Han, Z.; Kido, S.; Nakashima, N.; Fujigaya, T. Enhanced Platinum Utilization Efficiency of Polymer-Coated Carbon Black as an Electrocatalyst in Polymer Electrolyte Membrane Fuel Cells. *Electrochim. Acta* **2019**, *312*, 349–357. https://doi.org/10.1016/j.electacta.2019.05.007.

(78) Wang, M.; Chen, M.; Yang, Z.; Liu, G.; Kee Lee, J.; Yang, W.; Wang, X. High-Performance and Durable Cathode Catalyst Layer with Hydrophobic C@PTFE Particles for Low-Pt Loading Membrane Assembly Electrode of PEMFC. *Energy Convers. Manag.* **2019**, *191* (February), 132–140. https://doi.org/10.1016/j.enconman.2019.04.014.

(79) Martin, S.; Martinez-Vazquez, B.; Garcia-Ybarra, P. L.; Castillo, J. L. Peak Utilization of Catalyst with Ultra-Low Pt Loaded PEM Fuel Cell Electrodes Prepared by the Electrospray Method. *J. Power Sources* **2013**, *229* (2013), 179–184. https://doi.org/10.1016/j.jpowsour.2012.12.029.

(80) Ohma, A.; Mashio, T.; Sato, K.; Iden, H.; Ono, Y.; Sakai, K.; Akizuki, K.; Takaichi, S.; Shinohara, K. Analysis of Proton Exchange Membrane Fuel Cell Catalyst Layers for Reduction of Platinum Loading at Nissan. *Electrochim. Acta* **2011**, *56* (28), 10832–10841. https://doi.org/10.1016/j.electacta.2011.04.058.

(81) Dietz, H. Gas-Diffusion-Controlled Solid-Electrolyte Oxygen Sensors. *Solid State Ionics* **1982**, *6* (2), 175–183. https://doi.org/10.1016/0167-2738(82)90085-6.

(82) Baker, D. R.; Caulk, D. A.; Neyerlin, K. C.; Murphy, M. W. Measurement of Oxygen Transport Resistance in PEM Fuel Cells by Limiting Current Methods. *J. Electrochem. Soc.* **2009**, *156* (9), B991. https://doi.org/10.1149/1.3152226.

(83) Owejan, J. P.; Owejan, J. E.; Gu, W. Impact of Platinum Loading and Catalyst Layer Structure on PEMFC Performance. *J. Electrochem. Soc.* **2013**, *160* (8), F824–F833. https://doi.org/10.1149/2.072308jes.

(84) Wagner, F. T.; Lakshmanan, B.; Mathias, M. F. Electrochemistry and the Future of the Automobile. *J. Phys. Chem. Lett.* **2010**, *1* (14), 2204–2219. https://doi.org/10.1021/jz100553m.

(85) Nonoyama, N.; Okazaki, S.; Weber, A. Z.; Ikogi, Y.; Yoshida, T. Analysis of Oxygen-Transport Diffusion Resistance in Proton-Exchange-Membrane Fuel Cells. *J. Electrochem. Soc.* **2011**, *158* (4), B416. https://doi.org/10.1149/1.3546038.

(86) Clancey, J. W.; Cavanagh, A. S.; Kukreja, R. S.; Kongkanand, A.; George, S. M. Atomic Layer Deposition of Ultrathin Platinum Films on Tungsten Atomic Layer Deposition Adhesion Layers: Application to High Surface Area Substrates. *J. Vac. Sci. Technol. A Vacuum, Surfaces, Film.* **2014**, *33* (1), 01A130. https://doi.org/10.1116/1.4901459.

(87) Yoshida, T.; Kojima, K. Toyota MIRAI Fuel Cell Vehicle and Progress Toward a Future Hydrogen Society. *Interface Mag.* **2015**, *24* (2), 45–49. https://doi.org/10.1149/2.f03152if.

(88) Gröger, O.; Gasteiger, H. A.; Suchsland, J.-P. Electromobility: Batteries or Fuel Cells? *J. Electrochem. Soc.* **2016**, *163* (7), X3. https://doi.org/10.1149/2.0431607jes.

(89) Chen Chen, Yijin Kang, Ziyang Huo, Zhongwei Zhu, Wenyu Huang, Huolin L. Xin, Joshua D. Snyder, Dongguo Li, Jeffery A. Herron, Manos Mavrikakis, Miaofang Chi, Karren L. More, Yadong Li, Nenad M. Markovic, Gabor A. Somorjai, Peidong Yang, V. R. S. Highly Crystalline Multimetallic Nanoframes with Three-Dimensional Electrocatalytic Surfaces. *Science (80-.).* **2014**,

343 (21 March), 1339–1343. https://doi.org/10.1126/science.1249061.
(90) Han, B.; Carlton, C. E.; Kongkanand, A.; Kukreja, R. S.; Theobald, B. R.; Gan, L.; O'Malley, R.; Strasser, P.; Wagner, F. T.; Shao-Horn, Y. Record Activity and Stability of Dealloyed Bimetallic Catalysts for Proton Exchange Membrane Fuel Cells. *Energy Environ. Sci.* **2015**, *8* (1), 258–266. https://doi.org/10.1039/c4ee02144d.
(91) Zhang, J.; Lima, F. H. B.; Shao, M. H.; Sasaki, K.; Wang, J. X.; Hanson, J.; Adzic, R. R. Platinum Monolayer on Nonnoble Metal-Noble Metal Core-Shell Nanoparticle Electrocatalysts for O2 Reduction. *J. Phys. Chem. B* **2005**, *109* (48), 22701–22704. https://doi.org/10.1021/jp055634c.
(92) Zhang, Y.; Hsieh, Y. C.; Volkov, V.; Su, D.; An, W.; Si, R.; Zhu, Y.; Liu, P.; Wang, J. X.; Adzic, R. R. High Performance Pt Monolayer Catalysts Produced via Core-Catalyzed Coating in Ethanol. *ACS Catal.* **2014**, *4* (3), 738–742. https://doi.org/10.1021/cs401091u.
(93) Debe, M. K. Nanostructured Thin FIlm Electrocatalysts for PEM Fuel Cells - A Tutorial on the Fundamental Characteristics and Practical Properties of NSTF Catalysts. *ECS Trans.* **2012**, *45* (2), 47–68.
(94) Tse, E. C. M.; Hoang, T. T. H.; Varnell, J. A.; Gewirth, A. A. Observation of an Inverse Kinetic Isotope Effect in Oxygen Evolution Electrochemistry. *ACS Catal.* **2016**, *6* (9), 5706–5714. https://doi.org/10.1021/acscatal.6b01170.
(95) Malko, D.; Kucernak, A. Kinetic Isotope Effect in the Oxygen Reduction Reaction (ORR) over Fe-N/C Catalysts under Acidic and Alkaline Conditions. *Electrochem. commun.* **2017**, *83* (June), 67–71. https://doi.org/10.1016/j.elecom.2017.09.004.
(96) Tse, E. C. M.; Barile, C. J.; Kirchschlager, N. A.; Li, Y.; Gewargis, J. P.; Zimmerman, S. C.; Hosseini, A.; Gewirth, A. A. Proton Transfer Dynamics Control the Mechanism of O2reduction by a Non-Precious Metal Electrocatalyst. *Nat. Mater.* **2016**, *15* (7), 754–759. https://doi.org/10.1038/nmat4636.
(97) M. M. Ghoneim, S. C. and E. Y. Oxygen Reduction Kinetics in Deuterated Phosphoric Acid. *J. Electrochem. Soc.* **1985**, *132* (5), 1160–1162. https://doi.org/10.1149/1.2114050.
(98) Tse, E. C. M.; Varnell, J. A.; Hoang, T. T. H.; Gewirth, A. A. Elucidating Proton Involvement in the Rate-Determining Step for Pt/Pd-Based and Non-Precious-Metal Oxygen Reduction Reaction Catalysts Using the Kinetic Isotope Effect. *J. Phys. Chem. Lett.* **2016**, *7* (18), 3542–3547. https://doi.org/10.1021/acs.jpclett.6b01235.
(99) Kunz, H. R. and G. A. G. The Catalytic Activity of Platinum Supported on Carbon for Electrochemical Oxygen Reduction in Phosphoric Acid. *J. Electrochem. Soc.* **1975**, *122* (10), 1279–1287. https://doi.org/10.1149/1.2134000.
(100) Union, I.; Pure, O. F.; Chemistry, A. Recommendations for the Characterization of Porous Solids. *Pure Appl. Chem.* **1994**, *66* (8), 1739–1758. https://doi.org/10.1001/jama.1902.02480490036009.
(101) Robertson, A. C. F. and J. Interpretation of Raman Spectra of Disordered and Amorphous Carbon. *Am. Phys. Soc.* **2000**, *61* (20), 14095–14107. https://doi.org/10.1136/ip.2010.029215.730.
(102) Cherstiouk, O. V.; Simonov, A. N.; Moseva, N. S.; Cherepanova, S. V.; Simonov, P. A.; Zaikovskii, V. I.; Savinova, E. R. Microstructure Effects on the Electrochemical Corrosion of Carbon Materials and Carbon-Supported Pt Catalysts. *Electrochim. Acta* **2010**, *55* (28), 8453–8460. https://doi.org/10.1016/j.electacta.2010.07.047.
(103) Katsnelson, M. I. Graphene: Carbon in Two Dimensions. *Mater. Today* **2007**, *10* (1), 20–27. https://doi.org/10.1017/CBO9781139031080.
(104) Guo, H.-L.; Wang, X.-F.; Qian, Q.-Y.; Wang, F.-B.; Xia, X.-H. A Green Approach to the Synthesis of Graphene Nanosheets. *ACS Nano* **2009**, *3* (9), 2653–2659. https://doi.org/10.1021/nn900227d.
(105) Bett, J. A.; Kinoshita, K.; Stonehart, P. Crystallite Growth of Platinum Dispersed on Graphitized Carbon Black. *J. Catal.* **1974**, *35* (2), 307–316. https://doi.org/10.1016/0021-9517(74)90209-7.
(106) Rodriguez-Reinoso, F. The Role Of Carbon Materials in Heterogenous Catalysis. *Carbon N. Y.* **1998**, *36* (3), 159–175. https://doi.org/10.1109/ICL-GNSS.2013.6577279.
(107) Wang, X.; Zhang, H.; Zhang, J.; Xu, H.; Zhu, X.; Chen, J.; Yi, B. Micro-Porous Layer with Composite Carbon Black for PEM Fuel Cells. *Electrochim. Acta* **2006**, *51* (1), 4909–4915.

https://doi.org/10.1016/j.jpowsour.2006.06.064.
(108) Watanabe, M.; Tryk, D. A. *Nanocarbons for Energy Conversion: Supramolecular Approaches*; Springer International Publishing, 2019. https://doi.org/10.1007/978-3-319-92917-0.
(109) Maillard, F.; Simonov, P. A.; Savinova, E. R. *Carbon Materials as Supports for Fuel Cell Electrocatalysts." Carbon Materials for Catalysis. John Wiley & Sons, Inc.*; 2008.
(110) Passalacqua, E.; Antonucci, P. L.; Vivaldi, M.; Patti, A.; Antonucci, V.; Giordano, N.; Kinoshita, K. The Influence of Pt on the Electrooxidation Behaviour of Carbon in Phosphoric Acid. *Electrochim. Acta* **1992**, *37* (15), 2725–2730. https://doi.org/10.1016/0013-4686(92)85199-U.
(111) Linse, N.; Gubler, L.; Scherer, G. G.; Wokaun, A. The Effect of Platinum on Carbon Corrosion Behavior in Polymer Electrolyte Fuel Cells. *Electrochim. Acta* **2011**, *56* (22), 7541–7549. https://doi.org/10.1016/j.electacta.2011.06.093.
(112) Maillard, F.; Bonnefont, A.; Micoud, F. An EC-FTIR Study on the Catalytic Role of Pt in Carbon Corrosion. *Electrochem. commun.* **2011**, *13* (10), 1109–1111. https://doi.org/10.1016/j.elecom.2011.07.011.
(113) Sihvonen, V. The Influence of Keto- and Ketene Groups, Adsorbed Molecules and Ions on the Mechanism of Carbon Oxidation. *J. Am. Chem. Soc.* **1938**, *37*, 1062–1074.
(114) Artyushkova, K.; Pylypenko, S.; Dowlapalli, M.; Atanassov, P. Structure-to-Property Relationships in Fuel Cell Catalyst Supports: Correlation of Surface Chemistry and Morphology with Oxidation Resistance of Carbon Blacks. *J. Power Sources* **2012**, *214*, 303–313. https://doi.org/10.1016/j.jpowsour.2012.04.095.
(115) Mathias, M.; Makharia, R. Two Fuel Cell Cars in Every Garage? *Electrochem. Soc. Interface* **2005**, *14* (June 2014), 24–35. https://doi.org/10.1039/B808370C.
(116) Makharia, R.; Kocha, S.; Yu, P.; Sweikart, M. A.; Gu, W.; Wagner, F.; Gasteiger, H. A. Durable PEM Fuel Cell Electrode Materials: Requirements and Benchmarking Methodologies. *ECS Trans.* **2006**, *1* (8), 3–18. https://doi.org/10.1149/1.2214540.
(117) Castanheira, L.; Dubau, L.; Mermoux, M.; Berthomé, G.; Caqué, N.; Rossinot, E.; Chatenet, M.; Maillard, F. Carbon Corrosion in Proton-Exchange Membrane Fuel Cells: From Model Experiments to Real-Life Operation in Membrane Electrode Assemblies. *ACS Catal.* **2014**, *4* (7), 2258–2267. https://doi.org/10.1021/cs500449q.
(118) Lim, D. H.; Wilcox, J. Mechanisms of the Oxygen Reduction Reaction on Defective Graphene-Supported Pt Nanoparticles from First-Principles. *J. Phys. Chem. C* **2012**, *116* (5), 3653–3660. https://doi.org/10.1021/jp210796e.
(119) Liu, H.; Li, J.; Xu, X.; Wang, F.; Liu, J.; Li, Z.; Ji, J. Highly Graphitic Carbon Black-Supported Platinum Nanoparticle Catalyst and Its Enhanced Electrocatalytic Activity for the Oxygen Reduction Reaction in Acidic Medium. *Electrochim. Acta* **2013**, *93*, 25–31. https://doi.org/10.1016/j.electacta.2013.01.090.
(120) Sharma, R.; Kar, K. K. Particle Size and Crystallographic Orientation Controlled Electrodeposition of Platinum Nanoparticles on Carbon Nanotubes. *Electrochim. Acta* **2015**, *156*, 199–206. https://doi.org/10.1016/j.electacta.2015.01.046.
(121) Shi, F.; Baker, L. R.; Hervier, A.; Somorjai, G. A.; Komvopoulos, K. Tuning the Electronic Structure of Titanium Oxide Support to Enhance the Electrochemical Activity of Platinum Nanoparticles. *Nano Lett.* **2013**, *13* (9), 4469–4474. https://doi.org/10.1021/nl402392u.
(122) Iden, H.; Sato, K.; Ohma, A.; Shinohara, K. Relationship among Microstructure, Ionomer Property and Proton Transport in Pseudo Catalyst Layers. *J. Electrochem. Soc.* **2011**, *158* (8), B987. https://doi.org/10.1149/1.3598141.
(123) Kusoglu, A.; Kushner, D.; Paul, D. K.; Karan, K.; Hickner, M. A.; Weber, A. Z. Impact of Substrate and Processing on Confinement of Nafion Thin Films. *Adv. Funct. Mater.* **2014**, *24* (30), 4763–4774. https://doi.org/10.1002/adfm.201304311.
(124) Page, K. A.; Kusoglu, A.; Stafford, C. M.; Kim, S.; Kline, R. J.; Weber, A. Z. Confinement-Driven Increase in Ionomer Thin-Film Modulus. *Nano Lett.* **2014**, *14* (5), 2299–2304. https://doi.org/10.1021/nl501233g.

(125) Wang, C.; Cheng, X.; Yan, X.; Shen, S.; Ke, C.; Wei, G.; Zhang, J. Respective Influence of Ionomer Content on Local and Bulk Oxygen Transport Resistance in the Catalyst Layer of PEMFCs with Low Pt Loading. *J. Electrochem. Soc.* **2019**, *166* (4), F239–F245. https://doi.org/10.1149/2.0401904jes.
(126) Ott, S.; Orfanidi, A.; Schmies, H.; Anke, B.; Nong, H. N.; Hübner, J.; Gernert, U.; Gliech, M.; Lerch, M.; Strasser, P. Ionomer Distribution Control in Porous Carbon-Supported Catalyst Layers for High-Power and Low Pt-Loaded Proton Exchange Membrane Fuel Cells. *Nat. Mater.* **2020**, *19* (1), 77–85. https://doi.org/10.1038/s41563-019-0487-0.
(127) Debe, M. K. Effect of Electrode Surface Area Distribution on High Current Density Performance of PEM Fuel Cells. *J. Electrochem. Soc.* **2011**, *159* (1), B53–B66. https://doi.org/10.1149/2.032201jes.
(128) Jomori, S.; Nonoyama, N.; Yoshida, T. Analysis and Modeling of PEMFC Degradation: Effect on Oxygen Transport. *J. Power Sources* **2012**, *215*, 18–27. https://doi.org/10.1016/j.jpowsour.2012.04.069.
(129) Yoon, W.; Weber, A. Z. Modeling Low-Platinum-Loading Effects in Fuel-Cell Catalyst Layers. *J. Electrochem. Soc.* **2011**, *158* (8), B1007–B1018. https://doi.org/10.1149/1.3597644.
(130) Ono, Y.; Mashio, T.; Takaichi, S.; Ohma, A.; Kanasaka, H.; Shinohara, K. The Analysis of Performance Loss with Low Platinum Loaded Catalyst Layers. *ECS Trans.* **2010**, *28* (27), 69–78.
(131) Soboleva, T.; Malek, K.; Xie, Z.; Navessin, T.; Holdcroft, S. PEMFC Catalyst Layers: The Role of Micropores and Mesopores on Water Sorption and Fuel Cell Activity. *ACS Appl. Mater. Interfaces* **2011**, *3* (6), 1827–1837. https://doi.org/10.1021/am200590w.
(132) Kusoglu, A.; Kwong, A.; Clark, K. T.; Gunterman, H. P.; Weber, A. Z. Water Uptake of Fuel-Cell Catalyst Layers. *J. Electrochem. Soc.* **2012**, *159* (9), F530–F535. https://doi.org/10.1149/2.031209jes.
(133) Weber, A. Z.; Borup, R. L.; Darling, R. M.; Das, P. K.; Dursch, T. J.; Gu, W.; Harvey, D.; Kusoglu, A.; Litster, S.; Mench, M. M.; Mukundan, R.; Owejan, J. P.; Pharoah, J. G.; Secanell, M.; Zenyuk, I. V. A Critical Review of Modeling Transport Phenomena in Polymer-Electrolyte Fuel Cells. *J. Electrochem. Soc.* **2014**, *161* (12), F1254–F1299. https://doi.org/10.1149/2.0751412jes.
(134) Schalenbach, M. Pressurized PEM Water Electrolysis: Efficiency and Gas Crossover. *Int. J. Hydrogen Energy* **2016**, *41* (1), 729–732. https://doi.org/10.1016/j.ijhydene.2015.11.009.
(135) Trinke, P.; Haug, P.; Brauns, J.; Bensmann, B.; Hanke-Rauschenbach, R.; Turek, T. Hydrogen Crossover in PEM and Alkaline Water Electrolysis: Mechanisms, Direct Comparison and Mitigation Strategies. *J. Electrochem. Soc.* **2018**, *165* (7), F502–F513. https://doi.org/10.1149/2.0541807jes.
(136) Inaba, M.; Kinumoto, T.; Kiriake, M.; Umebayashi, R.; Tasaka, A.; Ogumi, Z. Gas Crossover and Membrane Degradation in Polymer Electrolyte Fuel Cells. *Electrochim. Acta* **2006**, *51* (26), 5746–5753. https://doi.org/10.1016/j.electacta.2006.03.008.
(137) Francia, C.; Ijeri, V. S.; Specchia, S.; Spinelli, P. Estimation of Hydrogen Crossover through Nafion® Membranes in PEMFCs. *J. Power Sources* **2011**, *196* (4), 1833–1839. https://doi.org/10.1016/j.jpowsour.2010.09.058.
(138) Ji, C.; Niu, H.; Wang, S.; Liang, C.; Li, X.; Yang, J. Research on Two-Phase Flow Considering Hydrogen Crossover in the Membrane for a Polymer Electrolyte Membrane Fuel Cell. *Int. J. Energy Res.* **2019**, No. November 2018, 2881–2896. https://doi.org/10.1002/er.4430.
(139) Yeager, H. L. Cation and Water Diffusion in Nafion Ion Exchange Membranes: Influence of Polymer Structure. *J. Electrochem. Soc.* **1981**, *128* (9), 1880. https://doi.org/10.1149/1.2127757.
(140) Sakai, T. Gas Diffusion in the Dried and Hydrated Nafions. *J. Electrochem. Soc.* **2006**, *133* (1), 88. https://doi.org/10.1149/1.2108551.
(141) Shyam S. Kocha, J. D. Y. and J. S. Y. Characterization of Gas Crossover and Its Implications in PEM Fuel Cells. *AIChE J.* **2006**, *52* (5), 1916–1625. https://doi.org/10.1002/aic.
(142) Cheng, X.; Zhang, J.; Tang, Y.; Song, C.; Shen, J.; Song, D.; Zhang, J. Hydrogen Crossover in High-Temperature PEM Fuel Cells. *Journal of Power Sources*. 2007, pp 25–31. https://doi.org/10.1016/j.jpowsour.2007.02.027.

(143) Springer, T. E. Polymer Electrolyte Fuel Cell Model. *J. Electrochem. Soc.* **2006**, *138* (8), 2334. https://doi.org/10.1149/1.2085971.
(144) Sharma, R.; Grahl-Madsen, L.; Andersen, S. M. Influence of Dispersion Media on Nafion ® Ionomer Distribution in Proton Exchange Membrane Fuel Cell Catalyst Carbon Support. *Mater. Chem. Phys.* **2019**, *226* (November 2018), 66–72. https://doi.org/10.1016/j.matchemphys.2019.01.015.
(145) Robson, M. H.; Serov, A.; Artyushkova, K.; Atanassov, P. A Mechanistic Study of 4-Aminoantipyrine and Iron Derived Non-Platinum Group Metal Catalyst on the Oxygen Reduction Reaction. *Electrochim. Acta* **2013**, *90*, 656–665. https://doi.org/10.1016/j.electacta.2012.11.025.
(146) Amadelli, R.; Marković, N.; Adžić, R.; Yeager, E. Oxygen Reduction on Electrode Surfaces Modified by Underpotential Deposited Species: Thallium on Gold. *J. Electroanal. Chem.* **1983**, *159* (2), 391–412. https://doi.org/10.1016/S0022-0728(83)80636-6.
(147) Tripković, V.; Skúlason, E.; Siahrostami, S.; Nørskov, J. K.; Rossmeisl, J. The Oxygen Reduction Reaction Mechanism on Pt(1 1 1) from Density Functional Theory Calculations. *Electrochim. Acta* **2010**, *55* (27), 7975–7981. https://doi.org/10.1016/j.electacta.2010.02.056.
(148) Masel, R. I. Principles of Adsorption and Reaction on Solid Surfaces. *Wiley Ser. Chem. Eng.* **1996**, xiv, 804 p. https://doi.org/10.1177/004209800904600711O5.
(149) Fletcher, S. Tafel Slopes From First Principles. *J. Solid State Electrochem.* **2009**, *13* (4), 537–549.
(150) Klinman, J. P. The Power of Integrating Kinetic Isotope Effects into the Formalism of the Michaelis-Menten Equation. *FEBS J.* **2014**, *281* (2), 489–497. https://doi.org/10.1111/febs.12477.
(151) SD, N.; WF., T. The Use of Deuterium Isotope Effects to Probe the Active Site Properties, Mechanism of Cytochrome P450-Catalyzed Reactions, and Mechanisms of Metabolically Dependent Toxicity. *Drug Metab. Dispos.* **2003**, *31* (12), 1481–1498.
(152) González-Lafont, À.; Lluch, J. M. Kinetic Isotope Effects in Chemical and Biochemical Reactions: Physical Basis and Theoretical Methods of Calculation. *Wiley Interdiscip. Rev. Comput. Mol. Sci.* **2016**, *6* (5), 584–603. https://doi.org/10.1002/wcms.1268.
(153) Christensen, N. J.; Fristrup, P. Kinetic Isotope Effects (KIE) and Density Functional Theory (DFT): A Match Made in Heaven? *Synlett* **2015**, *26* (4), 508–513. https://doi.org/10.1055/s-0034-1380097.
(154) Westheimer, F. H. The Magnitude of the Primary Kinetic Isotope Effect for Compounds of Hydrogen and Deuterium. *Chem. Rev.* **1961**, *61* (3), 265–273. https://doi.org/10.1021/cr60211a004.
(155) George, T. Y.; Asset, T.; Avid, A.; Atanassov, P.; Zenyuk, I. V. Kinetic Isotope Effect as a Tool to Investigate the Oxygen Reduction Reaction on Pt-based Electrocatalysts. Part I: High-loading Pt/C and Pt Extended Surface. *ChemPhysChem* **2020**, *21*, 1–8. https://doi.org/10.1002/cphc.201901091.
(156) Asset, T.; Dubau, L.; Maillard, F.; Berthon-Fabry, S.; Guérin, K.; Dubois, M.; Chatenet, M.; Labbé, F.; Metkemeijer, R.; Batisse, N.; Chattot, R.; Asset, T.; Ahmad, Y. Activity and Durability of Platinum-Based Electrocatalysts Supported on Bare or Fluorinated Nanostructured Carbon Substrates. *J. Electrochem. Soc.* **2018**, *165* (6), F3346–F3358. https://doi.org/10.1149/2.031806jes.
(157) Herricks, T.; Chen, J.; Xia, Y. Polyol Synthesis of Platinum Nanoparticles: Control of Morphology with Sodium Nitrate. *Nano Lett.* **2004**, *4* (12), 2367–2371. https://doi.org/10.1021/nl048570a.
(158) Oh, H. S.; Oh, J. G.; Hong, Y. G.; Kim, H. Investigation of Carbon-Supported Pt Nanocatalyst Preparation by the Polyol Process for Fuel Cell Applications. *Electrochim. Acta* **2007**, *52* (25), 7278–7285. https://doi.org/10.1016/j.electacta.2007.05.080.
(159) Oh, H. S.; Oh, J. G.; Kim, H. Modification of Polyol Process for Synthesis of Highly Platinum Loaded Platinum-Carbon Catalysts for Fuel Cells. *J. Power Sources* **2008**, *183* (2), 600–603. https://doi.org/10.1016/j.jpowsour.2008.05.070.
(160) Dzara, M. J.; Artyushkova, K.; Shulda, S.; Strand, M. B.; Ngo, C.; Crumlin, E. J.; Gennett, T.; Pylypenko, S. Characterization of Complex Interactions at the Gas-Solid Interface with in Situ Spectroscopy: The Case of Nitrogen-Functionalized Carbon. *J. Phys. Chem. C* **2019**, *123* (14), 9074–9086. https://doi.org/10.1021/acs.jpcc.9b00487.
(161) Sakaushi, K. Observation of Kinetic Isotope Effect in Electrocatalysis with Fully Deuterated Ultrapure Electrolytes. *J. Electroanal. Chem.* **2019**, *849*, 113372.

https://doi.org/10.1016/j.jelechem.2019.113372.
(162) Wang, J.; Yin, G.; Shao, Y.; Wang, Z.; Gao, Y. Investigation of Further Improvement of Platinum Catalyst Durability with Highly Graphitized Carbon Nanotubes Support. *J. Phys. Chem. C* **2008**, *112* (15), 5784–5789. https://doi.org/10.1021/jp800186p.
(163) Dresselhaus, M. S.; Dresselhaus, G.; Saito, R.; Jorio, A. Raman Spectroscopy of Carbon Nanotubes. *Phys. Rep.* **2005**, *409* (2), 47–99. https://doi.org/10.1016/j.physrep.2004.10.006.
(164) He, H.; Gao, C. Graphene Nanosheets Decorated with Pd, Pt, Au, and Ag Nanoparticles: Synthesis, Characterization, and Catalysis Applications. *Sci. China Chem.* **2011**, *54* (2), 397–404. https://doi.org/10.1007/s11426-010-4191-9.
(165) Sadezky, A.; Muckenhuber, H.; Grothe, H.; Niessner, R.; Pöschl, U. Raman Microspectroscopy of Soot and Related Carbonaceous Materials: Spectral Analysis and Structural Information. *Carbon N. Y.* **2005**, *43* (8), 1731–1742. https://doi.org/10.1016/j.carbon.2005.02.018.
(166) Knight, D. S.; White, W. B. Characterization of Diamond Films by Raman Spectroscopy. **1989**, 385–393.
(167) Bockris, J. O.; Srinivasan, S. Theoretical Calculations of the Separation Factors in the Hydrogen Evolution Reaction for the Slow Recombination Mechanism. *J. Electrochem. Soc.* **2007**, *111* (7), 858. https://doi.org/10.1149/1.2426268.
(168) Bevilacqua, M.; Bianchini, C.; Marchionni, A.; Filippi, J.; Lavacchi, A.; Miller, H.; Oberhauser, W.; Vizza, F.; Granozzi, G.; Artiglia, L.; Annen, S. P.; Krumeich, F.; Grützmacher, H. Improvement in the Efficiency of an OrganoMetallic Fuel Cell by Tuning the Molecular Architecture of the Anode Electrocatalyst and the Nature of the Carbon Support. *Energy Environ. Sci.* **2012**, *5* (9), 8608–8620. https://doi.org/10.1039/c2ee22055e.
(169) Nesselberger, M.; Roefzaad, M.; Fayçal Hamou, R.; Ulrich Biedermann, P.; Schweinberger, F. F.; Kunz, S.; Schloegl, K.; Wiberg, G. K. H.; Ashton, S.; Heiz, U.; Mayrhofer, K. J. J.; Arenz, M. The Effect of Particle Proximity on the Oxygen Reduction Rate of Size-Selected Platinum Clusters. *Nat. Mater.* **2013**, *12* (10), 919–924. https://doi.org/10.1038/nmat3712.
(170) Maillard, F.; Savinova, E. R.; Stimming, U. CO Monolayer Oxidation on Pt Nanoparticles: Further Insights into the Particle Size Effects. *J. Electroanal. Chem.* **2007**, *599* (2), 221–232. https://doi.org/10.1016/j.jelechem.2006.02.024.
(171) Jiang, P.; Porsgaard, S.; Borondics, F.; Kober, M.; Caballero, A.; Bluhm, H.; Besenbacher, F.; Salmero, M. Room-Temperature Reaction of Oxygen with Gold: An in Situ Ambient-Pressure x-Ray Photoelectron Spectroscopy Investigation. *J. Am. Chem. Soc.* **2010**, *132* (9), 2858–2859. https://doi.org/10.1021/ja909987j.
(172) Grass, M. E.; Zhang, Y.; Butcher, D. R.; Park, J. Y.; Li, Y.; Bluhm, H.; Bratlie, K. M.; Zhang, T.; Somorjai, G. A. A Reactive Oxide Overlayer on Rhodium Nanoparticles during CO Oxidation and Its Size Dependence Studied by In Situ Ambient-Pressure X-Ray Photoelectron Spectroscopy. *Angew. Chemie* **2008**, *120* (46), 9025–9028. https://doi.org/10.1002/ange.200803574.
(173) Qadir, K.; Joo, S. H.; Mun, B. S.; Butcher, D. R.; Renzas, J. R.; Aksoy, F.; Liu, Z.; Somorjai, G. A.; Park, J. Y. Intrinsic Relation between Catalytic Activity of CO Oxidation on Ru Nanoparticles and Ru Oxides Uncovered with Ambient Pressure XPS. *Nano Lett.* **2012**, *12* (11), 5761–5768. https://doi.org/10.1021/nl303072d.
(174) Lagarteira, T.; Delgado, S.; Fernandes, C.; Azenha, C.; Mateos-Pedrero, C.; Mendes, A. The Role of Pt Loading on Reduced Graphene Oxide Support in the Polyol Synthesis of Catalysts for Oxygen Reduction Reaction. *Int. J. Hydrogen Energy* **2020**, No. xxxx. https://doi.org/10.1016/j.ijhydene.2020.02.022.
(175) Wang, Y.; Seo, B.; Wang, B.; Zamel, N.; Jiao, K.; Adroher, X. C. Fundamentals, Materials, and Machine Learning of Polymer Electrolyte Membrane Fuel Cell Technology. *Energy AI* **2020**, *1*, 100014. https://doi.org/10.1016/j.egyai.2020.100014.
(176) Zhang, G.; Wu, J.; Wang, Y.; Yin, Y.; Jiao, K. Investigation of Current Density Spatial Distribution in PEM Fuel Cells Using a Comprehensively Validated Multi-Phase Non-Isothermal Model. *Int. J. Heat Mass Transf.* **2020**, *150*. https://doi.org/10.1016/j.ijheatmasstransfer.2019.119294.

(177) Andrić, I.; Pina, A.; Ferrão, P.; Fournier, J.; Lacarrière, B.; Corre, O. Le. Assessing the Feasibility of Using the Heat Demand-Outdoor Temperature Function for a Long-Term District Heat Demand Forecast. *Energy Procedia* **2017**, *116*, 460–469. https://doi.org/10.1016/j.egypro.2017.05.093.
(178) Taylor, S.; Fabbri, E.; Levecque, P.; Schmidt, T. J.; Conrad, O. The Effect of Platinum Loading and Surface Morphology on Oxygen Reduction Activity. *Electrocatalysis* **2016**, *7* (4), 287–296. https://doi.org/10.1007/s12678-016-0304-3.
(179) Zhang, G.; Bao, Z.; Xie, B.; Wang, Y.; Jiao, K. Three-Dimensional Multi-Phase Simulation of PEM Fuel Cell Considering the Full Morphology of Metal Foam Flow Field. *Int. J. Hydrogen Energy* **2020**, No. xxxx. https://doi.org/10.1016/j.ijhydene.2020.05.263.
(180) Rabis, A.; Rodriguez, P.; Schmidt, T. J. Electrocatalysis for Polymer Electrolyte Fuel Cells: Recent Achievements and Future Challenges. *ACS Catal.* **2012**, *2* (5), 864–890. https://doi.org/10.1021/cs3000864.
(181) Biddinger, E. J.; Deak, D. von; Singh, D.; Marsh, H.; Tan, B.; Knapke, D. S.; Ozkan, U. S. Examination of Catalyst Loading Effects on the Selectivity of CNx and Pt/VC ORR Catalysts Using RRDE. *J. Electrochem. Soc.* **2011**, *158* (4), B402. https://doi.org/10.1149/1.3552944.
(182) RezaeiTalarposhti, M.; Asset, T.; Garcia, S. T.; Chen, Y.; Herrera, S.; Dai, S.; Peterson, E. J.; Artyushkova, K.; Zenyuk, I.; Atanassov, P. Kinetic Isotope Effect as a Tool to Investigate the Oxygen Reduction Reaction on Pt-Based Electrocatalysts. Part II: Effect of the Platinum Dispersion. *ChemPhysChem* **2020**, No. April. https://doi.org/10.1002/cphc.201901092.
(183) Asset, T.; Dubau, L.; Ahmad, Y.; Batisse, N.; Dubois, M.; Gu, K.; Labb, F.; Metkemeijer, R.; Berthon-fabry, S.; Chatenet, M. JES F OCUS I SSUE ON P ROTON E XCHANGE M EMBRANE F UEL C ELL (PEMFC) D URABILITY Activity and Durability of Platinum-Based Electrocatalysts Supported on Bare or Fluorinated Nanostructured Carbon Substrates. **2018**, *165* (6), 3346–3358. https://doi.org/10.1149/2.031806jes.
(184) Fuel, U. S. D.; Tech, C. FCTT AST and Polarization Curve Protocols for PEMFCs - U.S. DRIVE Fuel Cell Tech Team Cell Component Accelerated Stress Test and Polarization Curve Protocols for PEM Fuel Cells. *U.S. DRIVE Fuel Cell Tech Team* **2013**.
(185) Neyerlin, K. C.; Gu, W.; Jorne, J.; Gasteiger, H. A. Determination of Catalyst Unique Parameters for the Oxygen Reduction Reaction in a PEMFC. *J. Electrochem. Soc.* **2006**, *153* (10), A1955. https://doi.org/10.1149/1.2266294.
(186) Harzer, G. S.; Schwämmlein, J. N.; Damjanović, A. M.; Ghosh, S.; Gasteiger, H. A. Cathode Loading Impact on Voltage Cycling Induced PEMFC Degradation: A Voltage Loss Analysis. *J. Electrochem. Soc.* **2018**, *165* (6), F3118–F3131. https://doi.org/10.1149/2.0161806jes.
(187) Kneer, A.; Jankovic, J.; Susac, D.; Putz, A.; Wagner, N.; Sabharwal, M.; Secanell, M. Correlation of Changes in Electrochemical and Structural Parameters Due to Voltage Cycling Induced Degradation in PEM Fuel Cells. *J. Electrochem. Soc.* **2018**, *165* (6), F3241–F3250. https://doi.org/10.1149/2.0271806jes.
(188) Gittleman, C. S.; Kongkanand, A.; Masten, D.; Gu, W. Materials Research and Development Focus Areas for Low Cost Automotive Proton-Exchange Membrane Fuel Cells. *Curr. Opin. Electrochem.* **2019**, *18*, 81–89. https://doi.org/10.1016/j.coelec.2019.10.009.
(189) Dubau, L.; Castanheira, L.; Maillard, F.; Chatenet, M.; Lottin, O.; Maranzana, G.; Dillet, J.; Lamibrac, A.; Perrin, J. C.; Moukheiber, E.; Elkaddouri, A.; De Moor, G.; Bas, C.; Flandin, L.; Caqué, N. A Review of PEM Fuel Cell Durability: Materials Degradation, Local Heterogeneities of Aging and Possible Mitigation Strategies. *Wiley Interdiscip. Rev. Energy Environ.* **2014**, *3* (6), 540–560. https://doi.org/10.1002/wene.113.
(190) Qu, L.; Wang, Z.; Guo, X.; Song, W.; Xie, F.; He, L.; Shao, Z.; Yi, B. Effect of Electrode Pt-Loading and Cathode Flow-Field Plate Type on the Degradation of PEMFC. *J. Energy Chem.* **2019**, *35*, 95–103. https://doi.org/10.1016/j.jechem.2018.09.004.
(191) Zenyuk, I. V.; Lamibrac, A.; Eller, J.; Parkinson, D. Y.; Marone, F.; Büchi, F. N.; Weber, A. Z. Investigating Evaporation in Gas Diffusion Layers for Fuel Cells with X-Ray Computed Tomography. *J. Phys. Chem. C* **2016**, *120* (50), 28701–28711.

https://doi.org/10.1021/acs.jpcc.6b10658.
(192) Gazdzicki, P.; Mitzel, J.; Sanchez, D. G.; Aßmann, P.; Sousa, J.; Morawietz, T.; Hiesgen, R.; Häußler, F.; Hunger, J.; Schlumberger, G.; Friedrich, K. A. Operando and Ex-Situ Investigation of PEMFC Degradation. *ECS Trans.* **2019**, *92* (8), 261–276. https://doi.org/10.1149/09208.0261ecst.
(193) Borup, R.; Meyers, J.; Pivovar, B.; Kim, Y. S.; Mukundan, R.; Garland, N.; Myers, D.; Wilson, M.; Garzon, F.; Wood, D.; Zelenay, P.; More, K.; Stroh, K.; Zawodzinski, T.; Boncella, J.; McGrath, J. E.; Inaba, M.; Miyatake, K.; Hori, M.; Ota, K.; Ogumi, Z.; Miyata, S.; Nishikata, A.; Siroma, Z.; Uchimoto, Y.; Yasuda, K.; Kimijima, K. I.; Iwashita, N. Scientific Aspects of Polymer Electrolyte Fuel Cell Durability and Degradation. *Chem. Rev.* **2007**, *107* (10), 3904–3951. https://doi.org/10.1021/cr050182l.
(194) De Bruijn, F. A.; Dam, V. A. T.; Janssen, G. J. M. Review: Durability and Degradation Issues of PEM Fuel Cell Components. *Fuel Cells* **2008**, *8* (1), 3–22. https://doi.org/10.1002/fuce.200700053.
(195) Wang, Z. B.; Zuo, P. J.; Wang, X. P.; Lou, J.; Yang, B. Q.; Yin, G. P. Studies of Performance Decay of Pt/C Catalysts with Working Time of Proton Exchange Membrane Fuel Cell. *J. Power Sources* **2008**, *184* (1), 245–250. https://doi.org/10.1016/j.jpowsour.2008.06.037.
(196) Ren, P.; Pei, P.; Li, Y.; Wu, Z.; Chen, D.; Huang, S. Degradation Mechanisms of Proton Exchange Membrane Fuel Cell under Typical Automotive Operating Conditions. *Prog. Energy Combust. Sci.* **2020**, *80*, 100859. https://doi.org/10.1016/j.pecs.2020.100859.
(197) Meier, J. C.; Galeano, C.; Katsounaros, I.; Witte, J.; Bongard, H. J.; Topalov, A. A.; Baldizzone, C.; Mezzavilla, S.; Schüth, F.; Mayrhofer, K. J. J. Design Criteria for Stable Pt/C Fuel Cell Catalysts. *Beilstein J. Nanotechnol.* **2014**, *5* (1), 44–67. https://doi.org/10.3762/bjnano.5.5.
(198) Darling, R. M.; Meyers, J. P. Kinetic Model of Platinum Dissolution in PEMFCs. *J. Electrochem. Soc.* **2003**, *150* (11), A1523. https://doi.org/10.1149/1.1613669.
(199) Zhang, S.; Yuan, X. Z.; Hin, J. N. C.; Wang, H.; Friedrich, K. A.; Schulze, M. A Review of Platinum-Based Catalyst Layer Degradation in Proton Exchange Membrane Fuel Cells. *J. Power Sources* **2009**, *194* (2), 588–600. https://doi.org/10.1016/j.jpowsour.2009.06.073.
(200) Zenyuk, I. V.; Das, P. K.; Weber, A. Z. Understanding Impacts of Catalyst-Layer Thickness on Fuel-Cell Performance via Mathematical Modeling. *J. Electrochem. Soc.* **2016**, *163* (7), F691–F703. https://doi.org/10.1149/2.1161607jes.
(201) Jahnke, T.; Futter, G. A.; Baricci, A.; Rabissi, C.; Casalegno, A. Physical Modeling of Catalyst Degradation in Low Temperature Fuel Cells: Platinum Oxidation, Dissolution, Particle Growth and Platinum Band Formation. *J. Electrochem. Soc.* **2020**, *167* (1), 013523. https://doi.org/10.1149/2.0232001JES.
(202) Fang, Z.; Star, A. G.; Fuller, T. F. Effect of Carbon Corrosion on Wettability of PEM Fuel Cell Electrodes. *J. Electrochem. Soc.* **2019**, *166* (12), F709–F715. https://doi.org/10.1149/2.0231912jes.
(203) Kneer, A.; Wagner, N. A Semi-Empirical Catalyst Degradation Model Based on Voltage Cycling under Automotive Operating Conditions in PEM Fuel Cells. *J. Electrochem. Soc.* **2019**, *166* (2), F120–F127. https://doi.org/10.1149/2.0641902jes.
(204) Zihrul, P.; Hartung, I.; Kirsch, S.; Huebner, G.; Hasché, F.; Gasteiger, H. A. Voltage Cycling Induced Losses in Electrochemically Active Surface Area and in H2/Air-Performance of PEM Fuel Cells. *J. Electrochem. Soc.* **2016**, *163* (6), F492–F498. https://doi.org/10.1149/2.0561606jes.
(205) Kneer, A.; Wagner, N.; Sadeler, C.; Scherzer, A. C.; Gerteisen, D. Effect of Dwell Time and Scan Rate during Voltage Cycling on Catalyst Degradation in PEM Fuel Cells. *J. Electrochem. Soc.* **2018**, *165* (10), F805–F812. https://doi.org/10.1149/2.0651810jes.
(206) Kongkanand, A.; Ziegelbauer, J. M. Surface Platinum Electrooxidation in the Presence of Oxygen. *J. Phys. Chem. C* **2012**, *116* (5), 3684–3693. https://doi.org/10.1021/jp211490a.
(207) Ferreira, P. J.; la O', G. J.; Shao-Horn, Y.; Morgan, D.; Makharia, R.; Kocha, S.; Gasteiger, H. A. Instability of Pt/C Electrocatalysts in Proton Exchange Membrane Fuel Cells. *J. Electrochem. Soc.* **2006**, *152* (11), A2256–A2271. https://doi.org/10.1149/1.2050347.
(208) Guilminot, E.; Corcella, A.; Charlot, F.; Maillard, F.; Chatenet, M. Detection of Pt[Sup Z+] Ions and Pt Nanoparticles Inside the Membrane of a Used PEMFC. *J. Electrochem. Soc.* **2007**, *154* (1),

B96. https://doi.org/10.1149/1.2388863.
(209) Myers, D. J.; Wang, X.; Smith, M. C.; More, K. L. Potentiostatic and Potential Cycling Dissolution of Polycrystalline Platinum and Platinum Nano-Particle Fuel Cell Catalysts. *J. Electrochem. Soc.* **2018**, *165* (6), F3178–F3190. https://doi.org/10.1149/2.0211806jes.
(210) Imai, H.; Izumi, K.; Matsumoto, M.; Kubo, Y.; Kato, K.; Imai, Y. In Situ and Real-Time Monitoring of Oxide Growth in a Few Monolayers at Surfaces of Platinum Nanoparticles in Aqueous Media. *J. Am. Chem. Soc.* **2009**, *131* (17), 6293–6300. https://doi.org/10.1021/ja810036h.
(211) Huang, Y.; Zhang, J.; Kongkanand, A.; Wagner, F. T.; Li, J. C. M.; Jorné, J. Transient Platinum Oxide Formation and Oxygen Reduction on Carbon-Supported Platinum and Platinum-Cobalt Alloy Electrocatalysts. *J. Electrochem. Soc.* **2014**, *161* (1), F10–F15. https://doi.org/10.1149/2.018401jes.
(212) Zhang, H.; Haas, H.; Hu, J.; Kundu, S.; Davis, M.; Chuy, C. The Impact of Potential Cycling on PEMFC Durability. *J. Electrochem. Soc.* **2013**, *160* (8), F840–F847. https://doi.org/10.1149/2.083308jes.
(213) Zhang, X.; Higier, A.; Zhang, X.; Liu, H. Experimental Studies of Effect of Land Width in PEM Fuel Cells with Serpentine Flow Field and Carbon Cloth. *Energies* **2019**, *12* (3). https://doi.org/10.3390/en12030471.
(214) Weber, A. Z.; Newman, J. Coupled Thermal and Water Management in Polymer Electrolyte Fuel Cells. *J. Electrochem. Soc.* **2006**, *153* (12), A2205. https://doi.org/10.1149/1.2352039.
(215) Wang, Y.; Chen, K. S.; Mishler, J.; Cho, S. C.; Adroher, X. C. A Review of Polymer Electrolyte Membrane Fuel Cells: Technology, Applications, and Needs on Fundamental Research. *Appl. Energy* **2011**, *88* (4), 981–1007. https://doi.org/10.1016/j.apenergy.2010.09.030.
(216) Mayrhofer, K. J. J.; Meier, J. C.; Ashton, S. J.; Wiberg, G. K. H.; Kraus, F.; Hanzlik, M.; Arenz, M. Fuel Cell Catalyst Degradation on the Nanoscale. *Electrochem. commun.* **2008**, *10* (8), 1144–1147. https://doi.org/10.1016/j.elecom.2008.05.032.
(217) Yoda, T.; Uchida, H.; Watanabe, M. Effects of Operating Potential and Temperature on Degradation of Electrocatalyst Layer for PEFCs. *Electrochim. Acta* **2007**, *52* (19), 5997–6005. https://doi.org/10.1016/j.electacta.2007.03.049.
(218) Shao, Y.; Kou, R.; Wang, J.; Viswanathan, V. V.; Kwak, J. H.; Liu, J.; Wang, Y.; Lin, Y. The Influence of the Electrochemical Stressing (Potential Step and Potential-Static Holding) on the Degradation of Polymer Electrolyte Membrane Fuel Cell Electrocatalysts. *J. Power Sources* **2008**, *185* (1), 280–286. https://doi.org/10.1016/j.jpowsour.2008.07.008.
(219) A.S. Arico', A. Stassi, E. Modica, R. Ornelas, I. Gatto, E. Passalacqua, V. A. Evaluation of High Temperature Degradation of Pt/C Catalysts in PEM Fuel Cells. *ECS Trans.* **2006**, *3* (1), 765–774. https://doi.org/10.1149/1.2356196.
(220) Xie, J.; Wood, D. L.; Wayne, D. M.; Zawodzinski, T. A.; Atanassov, P.; Borup, R. L. Durability of PEFCs at High Humidity Conditions. *J. Electrochem. Soc.* **2005**, *152* (1), 104–113. https://doi.org/10.1149/1.1830355.
(221) Siroma, Z.; Ishii, K.; Yasuda, K.; Inaba, M.; Tasaka, A. Stability of Platinum Particles on a Carbon Substrate Investigated by Atomic Force Microscopy and Scanning Electron Microscopy. *J. Power Sources* **2007**, *171* (2), 524–529. https://doi.org/10.1016/j.jpowsour.2007.06.016.
(222) Matsuoka, K.; Sakamoto, S.; Nakato, K.; Hamada, A.; Itoh, Y. Degradation of Polymer Electrolyte Fuel Cells under the Existence of Anion Species. *J. Power Sources* **2008**, *179* (2), 560–565. https://doi.org/10.1016/j.jpowsour.2008.01.027.
(223) Yu, P.; Pemberton, M.; Plasse, P. PtCo/C Cathode Catalyst for Improved Durability in PEMFCs. *J. Power Sources* **2005**, *144* (1), 11–20. https://doi.org/10.1016/j.jpowsour.2004.11.067.
(224) White, R. T.; Eberhardt, S. H.; Singh, Y.; Haddow, T.; Dutta, M.; Orfino, F. P.; Kjeang, E. Four-Dimensional Joint Visualization of Electrode Degradation and Liquid Water Distribution inside Operating Polymer Electrolyte Fuel Cells. *Sci. Rep.* **2019**, *9* (1), 1–12. https://doi.org/10.1038/s41598-018-38464-9.
(225) Cheng, L.; Khedekar, K.; Rezaei Talarposhti, M.; Perego, A.; Metzger, M.; Kuppan, S.; Stewart, S.; Atanassov, P.; Tamura, N.; Craig, N.; Zenyuk, I. V.; Johnston, C. M. Mapping of Heterogeneous

Catalyst Degradation in Polymer Electrolyte Fuel Cells. *Adv. Energy Mater.* **2020**, *2000623*, 1–7. https://doi.org/10.1002/aenm.202000623.
(226) R. Barabash, G. I. *Strain and Dislocation Gradients From Diffraction: Spatially-Resolved Local Structures and Defects*; Elsevier, 2014.
(227) Vogt, S.; Gleber, S.; Narayanan, S.; Newville, M. Scientific Data Exchange : A Schema for HDF5-Based Storage of Raw and Analyzed Data. *J. Synchrotron Radiat.* **2014**, *21*, 1224–1230.
(228) Palenstijn, W. J.; Sijbers, J. Integration of TomoPy and the ASTRA Toolbox for Advanced Processing and Reconstruction of Tomographic Synchrotron Data. *Comput. Programs* **2016**, *23*, 842–849. https://doi.org/10.1107/S1600577516005658.
(229) Carlo, F. De; Xiao, X.; Jacobsen, C. TomoPy : A Framework for the Analysis of Synchrotron Tomographic Data Research Papers. *J. Synchrotron Radiat.* **2014**, *21*, 1188–1193. https://doi.org/10.1107/S1600577514013939.
(230) Serov, A.; Shum, A. D.; Xiao, X.; Andrade, V. De; Artyushkova, K. Nano-Structured Platinum Group Metal-Free Catalysts and Their Integration in Fuel Cell Electrode Architectures. *Appl. Catal. B Environ.* **2018**, *237*, 1139–1147. https://doi.org/10.1016/j.apcatb.2017.08.067.
(231) Shum, A. D.; Parkinson, D. Y.; Xiao, X.; Weber, A. Z.; Burheim, O. S.; Zenyuk, I. V. Investigating Phase-Change-Induced Flow in Gas Diffusion Layers in Fuel Cells with X-Ray Computed Tomography. *Electrochim. Acta* **2017**, *256*, 279–290. https://doi.org/10.1016/j.electacta.2017.10.012.
(232) Schneider, C. A.; Rasband, W. S.; Eliceiri, K. W.; Instrumentation, C. NIH Image to ImageJ : 25 Years of Image Analysis. *Nat. Methods* **2012**, *9* (7), 671–675.
(233) Kabir, S.; Myers, D. J.; Kariuki, N.; Park, J.; Wang, G.; Baker, A.; Macauley, N.; Mukundan, R.; More, K. L.; Neyerlin, K. C. Elucidating the Dynamic Nature of Fuel Cell Electrodes as a Function of Conditioning: An Ex Situ Material Characterization and in Situ Electrochemical Diagnostic Study. *ACS Appl. Mater. Interfaces* **2019**, *11* (December), 45016–45030. https://doi.org/10.1021/acsami.9b11365.
(234) Dubau, L.; Castanheira, L.; Berthomé, G.; Maillard, F. An Identical-Location Transmission Electron Microscopy Study on the Degradation of Pt/C Nanoparticles under Oxidizing, Reducing and Neutral Atmosphere. *Electrochim. Acta* **2013**, *110*, 273–281. https://doi.org/10.1016/j.electacta.2013.03.184.
(235) Sugawara, Y.; Okayasu, T.; Yadav, A. P.; Nishikata, A.; Tsuru, T. Dissolution Mechanism of Platinum in Sulfuric Acid Solution. *J. Electrochem. Soc.* **2012**, *159* (11), F779–F786. https://doi.org/10.1149/2.017212jes.
(236) Lopes, P. P.; Strmcnik, D.; Tripkovic, D.; Connell, J. G.; Stamenkovic, V.; Markovic, N. M. Relationships between Atomic Level Surface Structure and Stability/Activity of Platinum Surface Atoms in Aqueous Environments. *ACS Catal.* **2016**, *6* (4), 2536–2544. https://doi.org/10.1021/acscatal.5b02920.
(237) Neyerlin, K. C.; Srivastava, R.; Yu, C.; Strasser, P. Electrochemical Activity and Stability of Dealloyed Pt-Cu and Pt-Cu-Co Electrocatalysts for the Oxygen Reduction Reaction (ORR). *J. Power Sources* **2009**, *186* (2), 261–267. https://doi.org/10.1016/j.jpowsour.2008.10.062.
(238) Pizzutilo, E.; Geiger, S.; Grote, J.-P.; Mingers, A.; Mayrhofer, K. J. J.; Arenz, M.; Cherevko, S. On the Need of Improved Accelerated Degradation Protocols (ADPs): Examination of Platinum Dissolution and Carbon Corrosion in Half-Cell Tests. *J. Electrochem. Soc.* **2016**, *163* (14), F1510–F1514. https://doi.org/10.1149/2.0731614jes.
(239) Curnick, O. J.; Pollet, B. G.; Mendes, P. M. Nafion®-Stabilised Pt/C Electrocatalysts with Efficient Catalyst Layer Ionomer Distribution for Proton Exchange Membrane Fuel Cells. *RSC Adv.* **2012**, *2* (22), 8368–8374. https://doi.org/10.1039/c2ra21071a.
(240) Sethuraman, V. A.; Weidner, J. W.; Haug, A. T.; Pemberton, M.; Protsailo, L. V. Importance of Catalyst Stability Vis-à-Vis Hydrogen Peroxide Formation Rates in PEM Fuel Cell Electrodes. *Electrochim. Acta* **2009**, *54* (23), 5571–5582. https://doi.org/10.1016/j.electacta.2009.04.062.
(241) Lai, Y. H.; Fly, G. W. In-Situ Diagnostics and Degradation Mapping of a Mixed-Mode Accelerated

Stress Test for Proton Exchange Membranes. *J. Power Sources* **2015**, *274*, 1162–1172. https://doi.org/10.1016/j.jpowsour.2014.10.116.

(242) Applied Physical Chemistry LaboratoryDepartment of Applied Chemistry, W. U. https://www.waseda.jp/top/en?utm_source=%2Ftop%2Findex-j.html.

(243) Online, V. A.; Uchida, M.; Park, Y.; Kakinuma, K.; Yano, H.; Tryk, D. A.; Kamino, T.; Uchida, H.; Watanabe, M. Effect of the State of Distribution of Supported Pt Nanoparticles on Effective Pt Utilization in Polymer Electrolyte Fuel Cells. *Phys. Chem. Chem. Phys.* **2013**, *15*, 11236–11247. https://doi.org/10.1039/c3cp51801a.